Summer 8-15-2019

Enhanced Magnetic Ordering in Sm Metal and Search for Superconductivity in Cs and Rb under Extreme Pressure

Yuhang Deng
Washington University in St. Louis

WASHINGTON UNIVERSITY IN ST. LOUIS

Department of Physics

Dissertation Examination Committee:
James S. Schilling, Chair
Erik Henriksen
Anne Hofmeister
Kenneth Kelton
Bryce Sadtler
Alexander Seidel

Enhanced Magnetic Ordering in Sm Metal and Search for Superconductivity in Cs and Rb under Extreme Pressure

by
Yuhang Deng

A dissertation presented to
The Graduate School
of Washington University in
partial fulfillment of the
requirements for the degree
of Doctor of Philosophy

August 2019
St. Louis, Missouri

Table of Contents

List of Figures

List of Tables

Acknowledgments

Financial support for the work contained within this dissertation was provided by the National Science Foundation (NSF) through Grant No. DMR-1104742 and No. DMR-1505345 as well as by the Carnegie/DOE Alliance Center (CDAC) through NNSA/DOE Grant No. DE-FC52-08NA28554.

The research results presented here would be impossible without many people's support and encouragement. In particular, I would like to sincerely thank:

Prof. James Schilling, my advisor, for his supervision, encouragement, and showing me how to think critically in doing research. He is a physicist who pays attention to every small detail in experiments, giving me an exemplary life as a high-pressure researcher.

Professors Erik Henriksen, Anne Hofmeister, Kenneth Kelton, Bryce Sadtler, and Alexander Seidel, for their kindly accepting to be my dissertation committee members.

Dr. Anne Hofmeister for lending me her drilling machine, drilling bits and her friendly guidance on how to use these tools. Without her help, I could not have completed cesium and rubidium experiments.

Dr. Anup Gangopadhyay for his support in arc-melting Y(Sm) alloys and suggestions on annealing the alloys.

Dr. Rex Couture for his support in analyzing the Sm content in Y(Sm) alloys by X-ray fluorescence spectroscopy.

Dr. Jing Song for teaching me how to conduct a high-pressure resistivity measurement with a DAC and for inspiring discussions with him.

Dr. Pallavi Malavi for the collaboration in measuring β-Li_2IrO_3 and β-Ce and her help in the lab when Prof. Schilling and Dr. Song were not in St. Louis.

The staff in the physics machine shop and the student shop, especially Todd and Tony, for their instruction and hard work in preparing many important parts of equipment.

My friends in the physics department. I had a great time in St. Louis because of their companionship. They encouraged me, shared happiness and stress throughout my whole graduate time in the physics department.

My wife Chuan Wang. I am indebted to her since she does a lot of housework and I have little time to accompany her. In order to support my life and research, she left her family for more than one year and has to tolerate a lonely life here in our little apartment. Without her support and care, I definitely could not have survived my graduate studies.

My daughter Olivia. She was born when I was in my fifth year of the PhD program. She is so cute and makes me realize that I must work hard to give her a bright future.

My parents Guoping Deng and Meifang Zhao. I was brought up and well educated by them, with great patience and unwavering love. They are among hundreds of millions of ordinary Chinese parents, industrious, simple, and willing to offer their all to their children. This dissertation would be my best gift to them.

Yuhang Deng

Washington University in St. Louis

August 2019

ABSTRACT OF THE DISSERTATION

Enhanced Magnetic Ordering in Sm Metal and

Search for Superconductivity in Cs and Rb

under Extreme Pressure

by

Yuhang Deng

Doctor of Philosophy in Physics

Washington University in St. Louis, 2019

Dr. James S. Schilling, Chair

At ambient pressure Sm metal orders antiferromagnetically at 106 K and 14 K. The pressure-dependence of the magnetic ordering temperature T_o of Sm metal was determined through four-point electrical resistivity measurements in a diamond anvil cell to pressures as high as 150 GPa. A strong increase in T_o with pressure is observed above 85 GPa. In this pressure range Sm ions alloyed in dilute concentration with superconducting Y exhibit giant Kondo pair breaking. Taken together, these results suggest that for pressures above 85 GPa Sm is in a highly correlated electron state, like a Kondo lattice, with an unusually high value of T_o. A detailed comparison is made with similar results obtained earlier on Nd, Tb and Dy and their dilute magnetic alloys with superconducting Y. All four lanthanides enter an "unconventional" magnetic state under very high pressure.

Resistivity measurements up to 45 GPa show that Cs, a member of heavy alkali metals, experiences a sharp resistance drop at $T_c \approx 1.4$ K for pressures above 12 GPa. The value of T_c

decreases upon the application of either a magnetic field or pressure. This result confirms the pressure-induced superconductivity for Cs nearly half a century ago reported by Wittig and significantly extends the pressure range studied. Parallel resistivity measurements are carried out on the lighter alkali metal Rb to 78 GPa pressure. Above 55 GPa Rb enters a superconducting state near 2 K where, as for Cs, T_c decreases in a magnetic field or pressure, T_c falling below 1.3 K above 85 GPa. In both Cs and Rb the superconductivity appears following a phase transformation from *tI*4 to *oC*16 with increasing pressure accompanied by a marked upturn in the room-temperature resistivity. The superconductivity, phase transition, and resistivity upturn are believed related to pressure-induced *s*-*d* electron transfer.

Chapter 1

Introduction

Pressure is an extremely useful thermodynamic variable to explore the physical properties of condensed matter because of its ability to directly change the distance between atoms. In condensed matter the atoms, or ion cores and valence electrons, are bound together by the electromagnetic force that is a function of the distance between the charged particles described by Coulomb's law. As a result it is straightforward to expect pressure to influence the properties of matter in a fundamental way since pressure tunes the forces between matter's atomic building blocks. On the other hand, the importance of pressure can be realized from the viewpoint of energy. In thermodynamics pressure (P) at constant temperature can be expressed as

$$P = -\left(\frac{\partial E}{\partial V}\right)_{S,N}, \tag{1.1}$$

where E is the internal energy, V is the volume, S is the entropy, and N is the number of particles in a system. This equation demonstrates that pressure affects the internal energy by changing the volume, leading to the change in the energy levels of the system. A multi-Mbar pressure could increase the energy per atom by several electron volts (eV). This huge energy, equivalent to 10^4 K, can significantly alter the ground state of matter: recall that the energy of a typical chemical bond is of the order of eV whereas most magnetic ordering temperatures and superconducting transition temperatures are only 10^0 to 10^2 K. Modern static high-pressure science often utilizes diamond anvil cell technology which allows pressures as high as several Mbar to be reached. Since its invention in the late 1950s, together with the development of a multitude of suitable

techniques, such as X-ray diffraction, electrical transport, magnetic susceptibility, and optical spectroscopy, diamond anvil cells have facilitated many profound discoveries in the field of high-pressure science.

Magnetic ordering in lanthanide metals at ambient pressure has been well explained by invoking the RKKY (Ruderman-Kittel-Kasuya-Yosida) exchange interaction. In lanthanide metals the magnetic moments of lanthanide trivalent ions are due to the unfilled 4*f* orbitals and are strongly localized. This implies that an indirect interaction must be responsible for ferromagnetism or antiferromagnetism. The RKKY interaction is an interaction between localized magnetic moments mediated by the surrounding conduction electrons (6*s* and 5*d* electrons). Based on the Weiss molecular field model, the ordering temperature of a lanthanide metal is proportional to $J_{ex}^2 N(E_F)(g_J - 1)^2 J(J+1)$ [1], where J_{ex} is the exchange interaction between local moment and the conduction electrons, $N(E_F)$ is the density of states at the Fermi level and $(g_J - 1)^2 J(J+1)$ is the de Gennes factor.

However, this simple scenario is insufficient when applying a pressure high enough to destabilize the magnetic state of lanthanide metals. Pressure can push lanthanides into an unstable magnetic state where the Kondo screening effect competes strongly with the RKKY interaction. The Kondo screening effect comes from the negative exchange interaction between the magnetic moments and surrounding conduction electrons that aligns the magnetic moment and nearby electron spins antiparallel. It will inevitably renormalize the positive RKKY exchange interaction. In this situation, the ordering temperature does not obey the de Gennes scaling any longer and often shows an unusual upturn with pressure. A superconductor doped

with lanthanide ions in an unstable magnetic state will also show a giant Kondo pair breaking effect. Such competition has been discovered earlier in Nd [2], Tb [3], and Dy [4].

Superconductivity is always a hot topic in condensed matter physics, especially for superconductors with high transition temperatures (T_c). Conventional superconductivity can be explained by the BCS (Bardeen, Cooper, Schrieffer) theory [5] that involves the concept of Cooper pairs formed at low temperature due to the electron-phonon coupling. BCS theory gives an equation to calculate T_c in the limit of a weak electron-phonon coupling: $T_c = 1.14\left(\frac{\hbar\omega_D}{k_B}\right)\exp\left[-\frac{1}{N(E_F)V_{eff}}\right]$ where ω_D is the Debye frequency and V_{eff} the (positive) effective attractive potential between the electrons in the Cooper pair. Pressure can change T_c by stiffening the lattice to alter ω_D and V_{eff}, and by broadening energy bandwidth to affect $N(E_F)$. For those unconventional superconductors which cannot be described by the BCS theory, such as cuprates and iron pnictides/chalcogenides, applying pressure causes T_c to change as well, but the interpretation is much more complicated.

At ambient pressure alkali metals are considered to be simple metals whose properties can be explained by the nearly-free-electron model. Here the electron-phonon coupling is weak which means their T_c would be quite low. In fact, at ambient pressure only Li has been found to be superconducting, but at the very low temperature of 0.4 mK [6]. However, in alkali metals high pressure can cause electrons to transfer from the *s* band to the *p* or *d* band and induce superconductivity with $T_c \approx 14$ K in Li at 30 GPa [7] and $T_c \approx 1.4$ K in Cs at 14 GPa [8]. Alkali metals are among the most compressible elements. Pressure can readily shorten the atomic distance, making the Wigner-Seitz radius r_a comparable to the ion core radius r_c so that there is

some overlap between the orbitals of the core electrons. As a result, under very high pressure the alkali metals cannot be viewed as simple metals and a superconducting state may emerge.

This dissertation mainly concerns itself with the important role of pressure in magnetism in the lanthanides and superconductivity in the alkalis. It is organized as follows. Chapter 2 provides general theoretical background information on magnetism, superconductivity, pressure effect on magnetism and superconductivity. Chapter 3 presents the high-pressure techniques including the helium gas system and diamond anvil cell. Chapter 4 describes the results of measurements on Sm, Y(Sm), Cs, and Rb. Chapter 5 contains a brief summary of the results. The dissertation ends with the appendices including experiments on β-Ce, $PbTaSe_2$, $Bi_2Te_3/Fe_{1+y}Te$ heterostructure, and β-Li_2IrO_3.

Chapter 2

Theoretical Background

2.1 Ferromagnetism and Antiferromagnetism

The fundamental object in magnetism is the magnetic moment. In atoms the magnetic moments of the nuclei are tiny and can be neglected compared with the magnetic moments of electrons. Materials which consist of atoms with unpaired core electrons are either paramagnetic or ferro/antiferromagnetic, depending on whether the magnetic moments of atoms tend to align spontaneously in the absence of a magnetic field. To distinguish these different forms of magnetism, the temperature dependence of the magnetic susceptibility χ is usually measured. The magnetic susceptibility characterizes the magnetic response of a material to an external magnetic field. The Curie-Weiss dependence can fit the magnetic susceptibility of materials versus temperature when the temperature is above the magnetic ordering temperature:

$$\chi \propto \frac{1}{T-\theta}, \tag{2.1}$$

$\theta = 0$: paramagnetic

$\theta > 0$: ferromagnetic and in the mean-field approximation $\theta = T_C$ the Curie temperature

$\theta < 0$: antiferromagnetic and in the mean-field approximation $\theta = T_N$ the Néel temperature,

where θ is the Curie-Weiss temperature. When the temperature is below the ordering temperature, $\chi(T)$ is not described by the Curie-Weiss law. The temperature-dependent susceptibility for the three kinds of magnetic materials is shown in Figure 2.1.

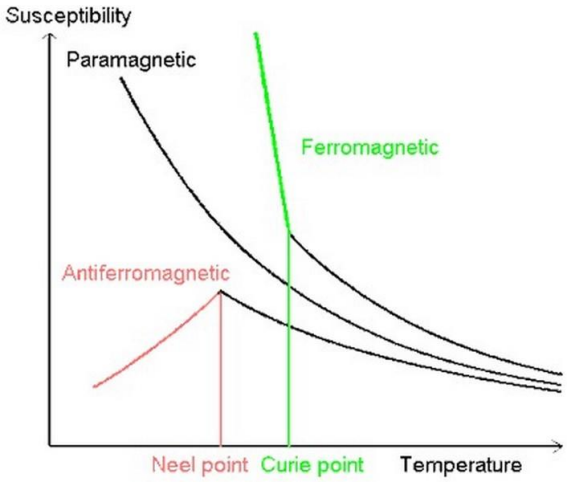

Figure 2.1: Temperature-dependent magnetic susceptibility for different forms of magnetism. When magnetic ordering occurs, the $\chi(T)$ curves deviate significantly from the Curie-Weiss law below the ordering temperature.

2.1.1 Weiss Molecular Field Model

Long-range ordering of paramagnetic ions in solids results from magnetic interactions between ions, including the magnetic dipolar interaction and different kinds of exchange interactions. The magnitude of the magnetic dipolar interaction is too weak (only about 1 K) to account for the magnetic ordering of most materials. Exchange interactions are basically electrostatic interactions. Usually the interactions are not direct. In other words, some intermediaries are needed to create magnetic ordering in solids: in ionic solids the interactions between non-neighboring magnetic ions are mediated by nearby non-magnetic ions; in metals conduction ions act as the medium between magnetic ions.

Now let's examine in some detail how the exchange interaction J leads to magnetic ordering. For a ferromagnet in an applied field $\vec{B}$, the Hamiltonian of the system is

$$H = -\sum_{ij} J_{ij} \vec{S}_i \cdot \vec{S}_j + g_J \mu_B \sum_j \vec{S}_j \cdot \vec{B}, \tag{2.2}$$

where J_{ij} is the interaction between ions at site i and j, and g_J is the Landé g-factor. Here we assume there is no orbital angular momentum in the ions in the system, so the total angular moment $\boldsymbol{J}$ obeys $\boldsymbol{J} = \boldsymbol{S}$, thus simplifying the problem. Define an effective molecular field at the site i

$$\vec{B}_{mf} = -\frac{2}{g_J \mu_B} \sum_j J_{ij} \vec{S}_j . \tag{2.3}$$

Then Eq. (2.2) can be reduced to

$$H = g_J \mu_B \sum_i \vec{S}_i \cdot (\vec{B} + \vec{B}_{mf}) . \tag{2.4}$$

The molecular field represents the contribution from the magnetic ordering which can be written as

$$\vec{B}_{mf} = \lambda \vec{M} , \tag{2.5}$$

where λ is a constant which parametrizes the strength of the molecular field as a function of the magnetization. For a ferromagnet, $\lambda > 0$.

Now the system can be treated as if it were in a magnetic field $\vec{B} + \vec{B}_{mf}$. At low temperature the magnetic moments are aligned due to the internal $\vec{B}_{mf}$, even without an external applied field $\vec{B}$. At high temperature thermal fluctuations begin to progressively destroy the magnetic ordering until at a critical temperature the order will be destroyed completely. This is the so-called Weiss model of ferromagnetism.

To find a solution to the Hamiltonian, it is necessary to solve the following equations simultaneously

$$M / M_S = B_J(y) , \tag{2.6}$$

$$y = \frac{g_J \mu_B J(B + \lambda M)}{k_B T}, \tag{2.7}$$

where M_S is the saturation magnetization, and $B_J(y)$ is the Brillouin function. Eqs. (2.6) and (2.7) can be solved graphically. If there is no external applied field (B = 0), a critical temperature T_C (Curie temperature) can be defined as the temperature below which two stable solutions to the equations appear. For a small y, $B_J(y) = \frac{(J+1)y}{3J} + O(y^3)$, then

$$T_C = \frac{g_J \mu_B (J+1) \lambda M_S}{3k_B} = \frac{n \lambda \mu_{eff}^2}{3k_B}, \tag{2.8}$$

where *n* is the total number of magnetic moments in the system and $\mu_{eff} = g_J \mu_B \sqrt{J(J+1)}$ is the effective moment. Note that $M_S = n g_J \mu_B J$.

If a small field *B* is applied at $T > T_C$, the y << 1 approximation for the Brillouin function can be used. Thus,

$$\frac{M}{M_S} \approx \frac{g_J \mu_B (J+1)}{3k_B} \left(\frac{B + \lambda M}{T} \right) = \frac{T_C}{\lambda M_S} \left(\frac{B + \lambda M}{T} \right). \tag{2.9}$$

So the magnetic susceptibility $\chi = \lim_{B \to 0} \frac{\mu_0 M}{B}$ can be expressed as

$$\chi = \frac{\mu_0 T_C}{\lambda} \frac{1}{T - T_C} \sim \frac{1}{T - T_C}. \tag{2.10}$$

This is the Curie-Weiss law mentioned in Eq. (2.1).

Assuming the exchange interaction is effective only over z nearest neighbors of a magnetic ion and it is isotropic with a value J_{ex}, then the constant λ can be written as

$$\lambda = \frac{2 z J_{ex}}{n g_J^2 \mu_B^2}. \tag{2.11}$$

Combined with Eq. (2.8), the Curie temperature can be expressed as

$$T_C = \frac{2zJ_{ex}J(J+1)}{3k_B}. \tag{2.12}$$

In the case of antiferromagnets, they can be viewed as two sets of sublattices in which magnetic ions order ferromagnetically. However, the total magnetizations of these two sublattices are anti-parallel to each other. Following a very similar treatment as for ferromagnets, two sets of internal molecular field are written as

$$\begin{aligned} B_+ &= -|\lambda| M_- \\ B_- &= -|\lambda| M_+ \end{aligned}, \tag{2.13}$$

where B_+ is the molecular field exerted by the "down" sublattice with M_- on the "up" sublattice and vice versa, λ the molecular field constant which is now negative for an antiferromagnet (so as the exchange interaction J_{ex}), and $|M_+| = |M_-| \doteq M$.

Then, using the same procedure to derive Eqs. (2.6) and (2.7), one obtains

$$M = M_S B_J\left(\frac{g_J \mu_B J(B + |\lambda| M)}{k_B T}\right). \tag{2.14}$$

In zero magnetic field $B = 0$, a critical temperature, known as the Néel temperature, is calculated to be

$$T_N = \frac{g_J \mu_B (J+1)|\lambda| M_S}{3k_B} = \frac{n|\lambda|\mu_{eff}^2}{3k_B}. \tag{2.15}$$

And under a small external magnetic field, the magnetic susceptibility can be expressed as

$$\chi = \lim_{B\to 0}\frac{\mu_0 M}{B} = \frac{\mu_0 T_C}{\lambda}\frac{1}{T+T_N} \sim \frac{1}{T+T_N}. \tag{2.16}$$

This is the Curie-Weiss law for antiferromagnets.

Note that so far $L = 0$ is assumed. This assumption is valid for most 3*d* ions. But for 4*f* ions (lanthanide ions), the component of $\vec{S}$ that is a good quantum number is $(g_J - 1)\vec{J}$ and the ordering temperatures of lanthanides should be changed to

$$T_o = \frac{2z|J_{ex}|(g_J - 1)^2 J(J+1)}{3k_B} \propto (g_J - 1)^2 J(J+1), \tag{2.17}$$

where $(g_J - 1)^2 J(J+1)$ is the well-known de Gennes factor.

2.1.2 Magnetism in Metals

In metals not only the localized magnetic ions but also the itinerant conduction electrons contribute to the overall magnetic properties of metals. Pauli paramagnetism is one of the forms of magnetism appearing in metals. It comes from the energy difference between spin-up and spin-down conduction electrons in the presence of a magnetic field. The external magnetic field lowers the energy of the electrons with spins parallel to the field and increases the energy of the electrons with spins antiparallel. As a result, the conduction electrons contribute a net magnetization with a direction the same as the field. Pauli paramagnetism is quite weak, compared to the Curie-Weiss paramagnetism found in insulators, since only a small portion of electrons near the Fermi surface participates in the response to the field.

Pauli paramagnetism is associated with the spins of electrons. Another magnetism in metals, Landau diamagnetism, involves the orbital angular momentum of conduction electrons in a field. The state of electron gas in a magnetic field will be quantized into a series of Landau tubes which lie parallel to the direction of the field. Electrons in the same Landau tube have the same eigen-energy related to the wave vectors perpendicular to the field, in the form of the eigen-energy of one-dimensional quantum harmonic oscillator. The magnetization of the system can be

obtained from calculating the derivative of the free energy with respect to the field. The calculated magnetization has an opposite sign to the field, which means it is a diamagnetic effect.

According to the discussion mentioned above, metals are either paramagnetic or diamagnetic, mainly depending on the comparison between the magnitudes of Pauli paramagnetism and Landau diamagnetism since the diamagnetism of the bound electrons in the ions is usually smaller than the effects associated with the conduction electrons. However, in many metals such as lanthanide metals, strong Curie-Weiss paramagnetism as well as ferromagnetism or antiferromagnetism emerge. Lanthanides are well known for their strongly paramagnetic 4*f* ions. Figure 2.2 shows the normalized radial charge density of Gd^{3+} versus distance *R* from the nucleus. As can been seen, only 5*d* and 6*s* orbitals have significant overlap with the same orbitals of the nearest Gd^{3+} ion. They form the conduction bands and contribute to binding in Gd metal. The other orbitals, including the 4*f* orbital, are quite localized: they do not overlap with the corresponding orbitals in other ions. The 4*f* orbital in Gd and other lanthanides has unpaired electrons which is responsible for the local magnetic moments in lanthanides. However, due to the large distance between the nearest 4*f* orbitals, no direct exchange interactions between them are expected.

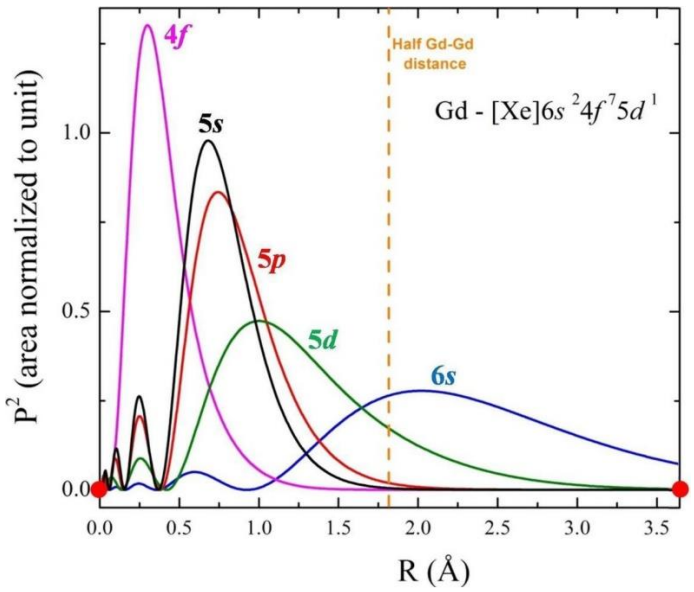

Figure 2.2: Normalized radial charge density of Gd^{3+} versus distance *R* from the nucleus. The two red dots mark the positions of two nearest neighbor Gd^{3+} ions. The orange dashed line marks the half-distance of the two ions. The figure is taken from ref [9].

In 1954, an indirect exchange interaction named after Ruderman, Kittel, Kasuya, and Yosida was proposed to explain the magnetic ordering in metals. This RKKY interaction emphasizes the function of conduction electrons in mediating the interactions between localized magnetic moments embedded in the sea of electron gas. The interaction between a magnetic moment and the surrounding electrons can be expressed by a Heisenberg exchange Hamiltonian $H_{ex} = -J_{ex}\vec{S}_m \cdot \vec{S}_c$ where J_{ex} is the coupling constant between the magnetic ion and the conduction electrons, $\vec{S}_m$ is the spin angular momentum of the magnetic ion in position $\vec{R}_i$, and $\vec{S}_c$ is the spin angular momentum of the conduction electrons. The interaction results in an oscillatory spin density in real space that interacts with the neighboring magnetic ions in position $\vec{R}_j$. The spin density has the form

$$\phi(x) = \frac{\sin x - x\cos x}{x^4}, x = 2\vec{k}_F\left|\vec{R}_i - \vec{R}_j\right|, \tag{2.18}$$

where $\vec{k}_F$ is the Fermi wave vector. For $\phi(x) > 0$ the indirect exchange coupling is ferromagnetic and for $\phi(x) < 0$, the coupling is antiferromagnetic.

The magnetic ordering temperature T_o is calculated as [1]

$$T_o = \frac{2\pi z}{k_B}\left[(g_J - 1)^2 J(J+1)\right] J_{ex}^2 N(E_F) \sum_{\vec{R}_i \neq \vec{R}_j} \phi\left(2\vec{k}_F \left|\vec{R}_i - \vec{R}_j\right|\right), \tag{2.19}$$

where z is the number of conduction electrons per atomic volume and $N(E_F)$ is the density of states at the Fermi level and $(g_J - 1)^2 J(J+1)$ is the de Gennes factor from Eq. (2.17). Again, only the electrons near the Fermi level contribute to the magnetic ordering. From Eq. (2.19) the ordering temperature for lanthanides is proportional to the de Gennes factor and $J_{ex}^2 N(E_F)$. Table 2.1 gives the magnetic ordering temperatures and the de Gennes factors for all lanthanide metals at ambient pressure, from which the validity of Eq. (2.19) can be seen.

Table 2.1: Magnetic ordering temperatures and de Gennes factors of lanthanide metals. Values are measured at ambient pressure. FM means ferromagnetism and AFM means antiferromagnetism.

Lanthanide ions in metals	Electronic configuration in metals	de Gennes factor of the ions in metals	Magnetic ordering temperature T_o(K)
La^{3+}	[Xe]$4f^0 5d^1 6s^2$	-	-
Ce^{3+}	[Xe]$4f^1 5d^1 6s^2$	0.18	12.5 (AFM)
Pr^{3+}	[Xe]$4f^2 5d^1 6s^2$	0.80	0.05 (AFM)
Nd^{3+}	[Xe]$4f^3 5d^1 6s^2$	1.84	20 (AFM), 8 (AFM)
Pm^{3+}	[Xe]$4f^4 5d^1 6s^2$	3.20	-
Sm^{3+}	[Xe]$4f^5 5d^1 6s^2$	4.46	106 (AFM), 14 (AFM)
Eu^{2+}	[Xe]$4f^7 6s^2$	-	90.4 (AFM)

Gd^{3+}	$[Xe]4f^{7}5d^{1}6s^{2}$	15.75	293 (FM)
Tb^{3+}	$[Xe]4f^{8}5d^{1}6s^{2}$	10.50	230 (AFM), 220 (FM)
Dy^{3+}	$[Xe]4f^{9}5d^{1}6s^{2}$	7.08	179 (AFM), 89 (FM)
Ho^{3+}	$[Xe]4f^{10}5d^{1}6s^{2}$	4.50	132 (AFM), 20 (FM)
Er^{3+}	$[Xe]4f^{11}5d^{1}6s^{2}$	2.55	85 (AFM), 20 (FM)
Tm^{3+}	$[Xe]4f^{12}5d^{1}6s^{2}$	1.17	58 (AFM), 32 (FM)
Yb^{2+}	$[Xe]4f^{14}6s^{2}$	-	-
Lu^{3+}	$[Xe]4f^{14}5d^{1}6s^{2}$	-	-

The de Gennes factors and magnetic ordering temperatures in Table 2.1 are mainly taken from [10]. Eu and Yb are divalent in the elemental metals. Note the obvious deviation from the de Gennes scaling in Ce, Eu, and Yb, because the exchange interactions in them are of the Coqblin-Schrieffer type [11] coming from the hybridization of the 4*f* levels with conduction electrons, leading to an antiferromagnetic exchange. The Heisenberg exchange interactions between 4*f* ions and conduction electrons in other lanthanides are ferromagnetic, coming from the Coulomb interaction in conjunction with the antisymmetry of the wave function [12].

2.1.3Magnetic Ordering under Pressure

Magnetism in a lattice consisting of magnetic ions has been discussed, but a question may arise regarding what will happen when a small concentration of magnetic ions is doped into a non-magnetic host to form a dilute magnetic alloy. A significant feature found in the temperature-dependent resistivity of selected dilute magnetic alloys is a resistivity minimum at low temperatures. In 1963 J. Kondo published a theory to explain the minimum that considers an antiferromagnetic (negative) exchange interaction between the magnetic impurities and the surrounding conduction electrons [13]. In a dilute magnetic alloy where the separation between

the magnetic impurities is so great that the RKKY coupling between them is neglectable (keep in mind that Eq. (2.18) decays rapidly with the separation), at high temperatures the magnetic impurities behave like free paramagnetic moments. But when the temperature is lower than a critical value called the Kondo temperature T_K, the negative exchange interaction between the impurities and the conduction electrons prompts the spins of the conduction electrons to form a cloud of opposite spin-polarization around each impurity spin. This magnetic screening process is known as the Kondo effect. The strong interaction enhances the electron-impurity scattering, resulting in the minimum in the temperature-dependent resistivity $R(T)$ of dilute magnetic alloys.

The $R(T)$ of a simple metal at low temperatures, including the Kondo effect, can be formulated as

$$\rho(T) = \rho_0 + aT^2 + bT^5 + cJ_{ex} \ln T \,, \tag{2.20}$$

where ρ_0 is the residual resistivity that includes both defect and spin-disorder scattering (to be discussed below), the T^2 term comes from electron-electron scattering (Fermi liquid behavior), the T^5 term comes from electron-phonon scattering, and $J_{ex} \ln T$ is the Kondo term with a negative J_{ex}, the antiferromagnetic exchange interaction between magnetic impurities and the conduction electrons. As the temperature is lowered further, the Kondo contribution to the resistivity grows dramatically, eventually reaching the temperature-independent unitary limit at the lowest temperatures.

In concentrated magnetic systems with a negative J_{ex}. there is a competition between the oscillatory RKKY interaction and the Kondo effect. Such systems are given the name "Kondo lattice". Doniach [14] proposed a simple Kondo lattice model to illustrate this competition and to explain the properties of heavy fermion systems. In this Kondo lattice model, the magnetic ordering temperature of a system where every magnetic moment in the lattice interacts with the

surrounding conduction electrons is determined by the magnitude of the negative exchange interaction J_{ex} between the magnetic moments and the conduction electrons. Here we apply the Kondo lattice model to study how the magnetic ordering temperatures T_o in lanthanide metals evolve with pressure. J_{ex} is the combination of the positive interaction J_+ which leads to RKKY interaction, and the negative interaction J_- which leads to the Kondo effect. At ambient pressure, J_{ex} in most lanthanide metals is positive, which means J_+ dominates J_-, and T_o follows the de Gennes scaling. However, pressure can push the magnetic ions to an unstable state in which J_- becomes predominant. As a result, the strong Kondo screening significantly renormalizes the interaction between magnetic moments, making T_o deviate significantly from the de Gennes scaling.

Figure 2.3 presents the Doniach phase diagram which describes the competition between J_+ and J_-. As can been seen, after J_{ex} becomes negative driven by high pressure, T_o increases initially with $|J_{ex}|$ to a maximum, followed by a sharp dive to the quantum critical point (QCP) near which many exotic phenomena such as non-Fermi liquid appear. J_-, resulting from the exponentially increasing T_K ($T_K \propto \exp\left[\frac{-1}{|J_{ex}|N(E_F)}\right]$). The magnetic ordering is quenched since it only increases as J_{ex}^2 ($T_{RKKY} \propto J_{ex}^2 N(E_F)$), in lanthanide metals under high pressure.

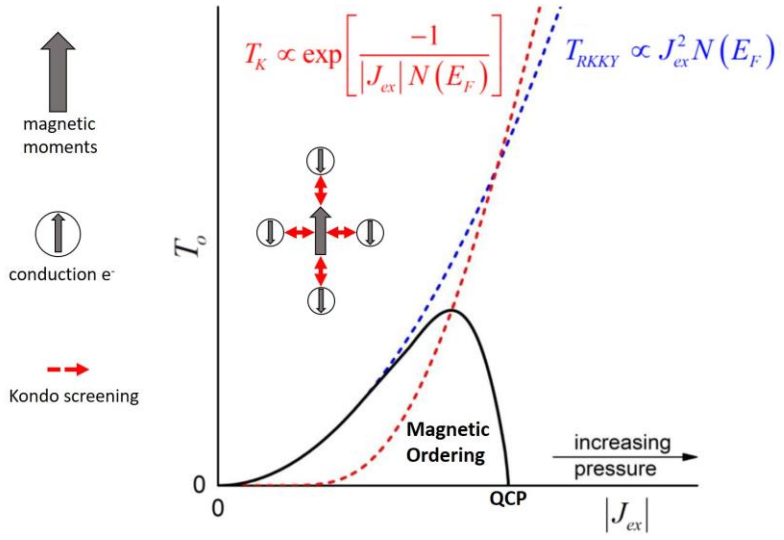

Figure 2.3: Competition between the RKKY interaction and the Kondo effect. This competition results in the phase diagram of the Kondo lattice given by S. Doniach [14]. The black curve represents the T_o versus $|J_{ex}|$. QCP denotes quantum critical point.

2.2 Superconductivity

Superconductivity was first discovered by Heike Kamerlingh Onnes and student Gilles Holst in 1911. In his lab at Leiden University, by measuring the resistance of mercury at cryogenic temperatures using the recently produced liquid helium as a refrigerant, they observed exactly zero resistance of mercury at 4.2 K. Superconductivity is characterized by two features: zero resistivity and the Meissner effect. In the Meissner effect the magnetic field flux is ejected from the interior of a superconductor when it enters the superconducting state as it is cooled below a critical temperature T_c. The Meissner effect demonstrates that superconductivity cannot be viewed as the idealization of a perfect conductor since the state of magnetic flux in a perfect conductor would not be changed according to the Maxwell's equations. Superconductors have found use in many applications, for example in NMR spectrometers and Tokamak plasma devices, maglev trains, and SQUID magnetometers (Josephson effect). Since the potential for practical applications increases substantially if T_c can be pushed above ambient temperatures,

scientists go to great lengths to search for superconductors with T_c values as high as possible. In 2018 M. Somayazulu *et al*. [15] reported that LaH_{10} displayed a significant drop in resistivity on cooling beginning around 260 K and pressures of 190 GPa. Later, A. P. Drozdov *et al*. [16] reported a similar observation in LaH_{10} and proved this is a superconducting transition through the observation of zero-resistance, isotope effect, and the decrease of T_c under an external magnetic field. In 2017, Dias and Silvera [17] reported that they had finally synthesized metallic hydrogen by applying pressures as high as 500 GPa. In 1968 metallic hydrogen was predicted by Ashcroft [18] to be a high temperature superconductor though Ashcroft thought 100 GPa would be sufficient to metallize hydrogen. Table 2.2 summarizes the properties of several different kinds of superconductors.

Table 2.2: Superconductors classified based on several different criteria.

Magnetic properties:	Type I, only one critical field separating normal and superconducting state. Al, Pb, Hg, $TaSi_2$ [19].	Type II, two critical fields in between is the vortex state. $Pb_{.98}In_{.02}$, Nb, V, boron doped diamond.
Critical temperature:	Low-T_c (T_c < 30 K). All elemental superconductors.	High-T_c (T_c > 30 K). MgB_2, YBCO family, Fe-based superconductors, LaH_{10} [15, 16]
Conventional (BCS theory) or unconventional:	Conventional. Most elemental superconductors.	Unconventional. Heavy fermion materials ($CeCu_2Si_2$, UPt_3), organic material $(TMTSF)_2PF_6$, cuprates, Fe-base superconductors, graphene bilayer misaligned by 1.1^o [20].

2.2.1BCS Theory

Many theories, both phenomenological and microscopic, have been developed to understand superconductivity. Among them are those from London (1935), Ginzburg-Landau (1950), and Bardeen, Cooper and Schrieffer (BCS) (1957). Although the BCS theory is unable to give a

satisfactory explanation for such unconventional superconductors as found in heavy Fermion, Cu-based, or Fe-based systems, it is still the most complete microscopic theory, one that is able to account for the superconducting state in the vast majority of materials, including the new hydride superconductors with values of T_c that approach ambient temperature.

In 1950 E. Maxwell [21] and C. Reynolds [22] found that the superconducting critical temperatures for Hg isotopes decreased with increasing nuclear mass of Hg isotopes (the so-called isotope effect), pointing to the importance of the crystal lattice in superconductivity. This in turn led to the development of the BCS theory [5] by three scientists (Bardeen, Cooper, Schrieffer) at the University of Illinois in Urbana-Champaign. An essential ingredient of BCS theory is the formation of Cooper pairs, pairs of electrons bound together at low temperatures. At first sight it appears weird that electrons can bind together in spite of the Coulomb repulsion between two negatively charged electrons. Taking the electron-phonon coupling into account, it can be shown that Cooper pairs can indeed be constructed though the binding energy is often only about 10^{-3} eV.

Suppose an electron e_1^- with wave vector $\vec{k}_1$ is moving through the crystal lattice. It attracts positive ions around it, deforms the lattice, and excites a phonon with wave vector q. The results of its moving are that (1) the final state of e_1^- becomes $\vec{k'}_1 = \vec{k}_1 - \vec{q}$ and (2) a region with slightly positive charge is created. This local positive charge region can remain for awhile because of the slow relaxation of the heavy ions compared to the light electrons. Therefore, a nearby electron e_2^- with $\vec{k}_2$ can be attracted to this slightly positive charged region and absorbs the excited phonon, transferring into a state with $\vec{k'}_2 = \vec{k}_2 + \vec{q}$. The pair consisting of the two electrons bound by the phonon is a Cooper pair. Figure 2.4 illustrates the formation of a Cooper pair.

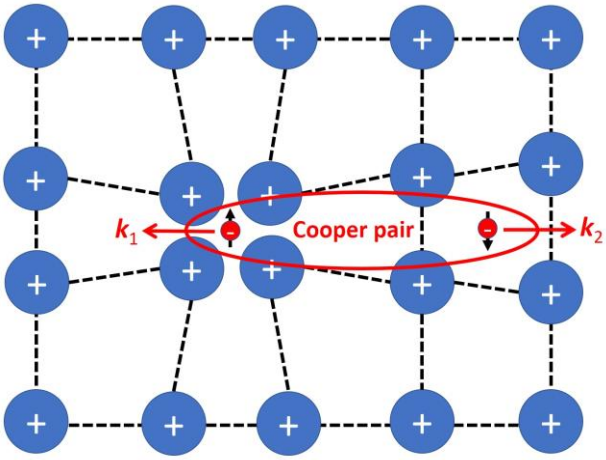

Figure 2.4: Schematic illustration of the formation of a Cooper pair. An electron with momentum $\vec{k}_1$ distorts the cations near it, creating a positive charge region that attracts a nearby electron with momentum $\vec{k}_2$. These two electrons form a Cooper pair, marked by a red circle.

Only electrons in a shell around the Fermi surface with width ~ $\hbar\omega_D$, where ω_D is the Debye frequency, can exchange phonons. Other energy transfers between states of electrons are forbidden due to the Pauli exclusion principle. This requires

$$\left|E\left(\vec{k}_1\right)-E\left(\vec{k'}_1\right)\right|<\hbar\omega_D, \tag{2.21}$$

where $E\left(\vec{k}_1\right)$ and $E\left(\vec{k'}_1\right)$ is the energy of e_1^- before and after emitting a phonon. Together with the conservation of momentum

$$\vec{k}_1+\vec{k}_2=\vec{k'}_1+\vec{k'}_2=\vec{q}_{tot}, \tag{2.22}$$

where $\vec{q}_{tot}$ is the total momentum of two electrons, the regions in which Cooper pairing could occur are shaded in in Figure 2.5 since only these regions satisfy (2.21) and (2.22) simultaneously. Since the interaction energy between e_1^- and e_2^- is related to attraction, the total energy of the system can be reduced by Cooper pairing, which means the system tends to increase the number of electrons paired as much as possible. To maximize the size of the shaded

region, the magnitude of $\vec{q}_{tot}$ should be minimized to zero. As a result, the electron states that make the largest contribution to Cooper pairing are the electrons with opposite momenta. Those Cooper pairs are bosons with either a total spin 0 (one electron spin up and one electron spin down, called *s*-wave Cooper pair) or 1 (*p*-wave Cooper pair, occurring in some unconventional superconductors). They undergo a Bose-Einstein condensation when the temperature falls below the binding energy of the Cooper pairs.

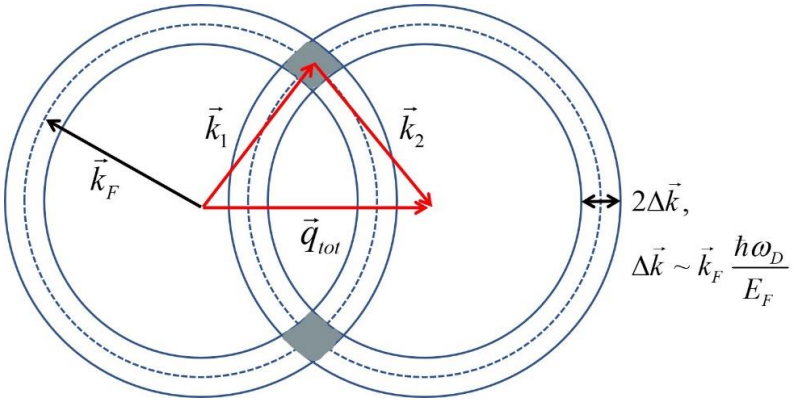

Figure 2.5: Electrons participating in the formation of Cooper pairs in the *k*-space. They are in the states shaded in grey that are within a thin shell around the Fermi surface with a width about $2\Delta k$. k_F is the Fermi vector and E_F is the Fermi energy.

In the limit of weak electron-phonon coupling, the critical temperature T_c given by BCS theory is

$$T_c = 1.14\left(\frac{\hbar\omega_D}{k_B}\right)\exp\left[-\frac{1}{N(E_F)V_{eff}}\right], \tag{2.23}$$

where $\hbar$ is the reduced Planck constant, k_B is the Boltzmann constant, $N(E_F)$ is the density of states at the Fermi level, and V_{eff} is the effective attractive potential between electrons (positive in sign for an attractive interaction, but negative in sign for a repulsive interaction).

Note that $\omega_D \sim M^{-1/2}$ where M is the mass of ions in the lattice. Eq. (2.23) thus gives the isotope effect directly. The total energy of a superconducting state reaches its minimum at 0 K. When

entering the BCS ground state the sharp step of the electron distribution at E_F showing in free-electron gas is rounded over an energy region $\sim 2\Delta_0$, where

$$\Delta_0 = 2\hbar\omega_D \exp\left[-\frac{1}{N(E_F)V_{eff}}\right]. \tag{2.24}$$

Combining Eqs. (2.23) and (2.24), a BCS predication is made

$$\frac{2\Delta_0}{k_B T_c} = 3.52\,. \tag{2.25}$$

Both T_c and the energy gap can be measured. Eq. (2.25) has been confirmed for many superconductors including Al (3.4) and In (3.6) [23]. The energy required to break up the Cooper pairs, and thus the superconducting state at a finite temperature below T_c, is

$$2\Delta(T) = 2\Delta_0\left[1.76\left(1-\frac{T}{T_c}\right)^{\frac{1}{2}}\right]. \tag{2.26}$$

For a normal metal, the specific heat comes from both electron and lattice terms. At low temperature the lattice term is small, and the specific heat is dominated by the electron term. When a metal becomes superconducting at T_c, the electronic specific heat changes discontinuously

$$\frac{c_s - c_n}{c_n}\Big|_{T_c} = 1.43\,, \tag{2.27}$$

where c_s and c_n are the electronic specific heat in the superconducting and normal state, respectively. Again, Eq. (2.27) agrees well with the ratio found for many superconductors such as Al (1.4) and In (1.7) [23]. BCS theory also presents a good description of the temperature dependence of the critical field H_c at which superconductivity is destroyed

$$H_c(T) \approx H_0\left[1-\left(\frac{T}{T_c}\right)^2\right], \tag{2.28}$$

where H_0 is the critical field at 0 K.

BCS theory is very successful when the electron-phonon interaction is weak. For some metals such as Pb and Hg, Eqs. (2.25) and (2.27) are unable to give good agreement with the experimental data. This is because the electron-phonon interaction in these metals is too strong. In 1960 Eliashberg proposed an integral equation (Eliashberg function) to describe the strength of electron-phonon coupling [24]

$$\lambda = 2\int_0^\infty \frac{\alpha^2(\omega)F(\omega)}{\omega}d\omega, \tag{2.29}$$

where $\alpha^2(\omega)$ is the matrix element describing the effective interaction between the electron and the lattice, and $F(\omega)$ is the phonon density of states. The weak, intermediate, and strong electron-phonon couplings correspond to $\lambda << 1$, $\lambda \approx 1$, and $\lambda > 1$, respectively. Then T_c for arbitrary coupling strength is given by

$$T_c = \frac{0.25\hbar\left\langle\omega^2\right\rangle^{1/2}}{k_B\left(e^{2/\lambda_{eff}}-1\right)^{1/2}}, \tag{2.30}$$

where λ_{eff} is the effective coupling constant given by

$$\lambda_{eff} = \frac{\lambda-\mu^*}{1+2\mu^*+\lambda\mu^* t(\lambda)}, \tag{2.31}$$

where μ^* is the Coulomb pseudopotential which takes into account the screened Coulomb repulsion between the electrons and $t(\lambda)$ is a universal function [25]. For a strong coupling ($\lambda > 1$), T_c is given by the McMillan equation [26]

$$T_c = \frac{\hbar\omega_D}{1.45k_B}\exp\left[-\frac{1.04(1+\lambda)}{\lambda-\mu^*(1+0.62\lambda)}\right], \tag{2.32}$$

where the Debye frequency has been used for the characteristic phonon frequency. In the limit of weak coupling, all these equations reduce to those given by BCS theory.

2.2.2 Superconductivity under Pressure

BCS theory emphasizes the importance of electron-phonon coupling in conventional superconductivity. It is not surprising at all that pressure can influence superconductivity significantly since pressure can bring ions in materials closer together, changing the phonon spectrum and the electronic density of states at the Fermi level. As can been seen in Eq. (2.23), under pressure ω_D can be enhanced because ω_D is positively related to the lattice spring constant k which would be increased under pressure. However, pressure also affects the $N(E_F)V_{eff}$ term in the dominating exponential factor. To see clearly how pressure influence T_c, neglecting the small effective Coulomb repulsion, Eq. (2.23) is rewritten as

$$T_c = 1.14\left(\frac{\hbar}{k_B}\right)\sqrt{\frac{k}{M}}\exp\left[-\frac{k}{\eta}\right], \tag{2.33}$$

where k is the lattice spring constant, M is the mass of ions, and the Hopfield parameter is given by $\eta = N(E_F)\langle I^2\rangle$, where $\langle I^2\rangle$ the average square electronic matrix element. As mentioned above, pressure usually increases k due to lattice stiffening under pressure but η usually increases with pressure as well. Whether pressure increases T_c or not depends on the competition between the $k(P)$ and $\eta(P)$. In simple (s- and p-electron) metals like Al, Cd, Zn, In, Sn, and Pb, k increases more rapidly than η under pressure so the exponential term in Eq. (2.33) dominates and T_c decreases [27] as seen in Figure 2.6 (left). In transition (d-electron) metals, T_c under

pressure becomes uncertain: can either increase or decrease depending on the relative change of k to η. For some transition metals such as Tl and Re, there even exists a non-monotonic dependence of T_c on P. For example, T_c (P) of Re shows a minimum around 0.6 GPa [28] as seen in Figure 2.6 (right). Together with the fact that alloying Os into Re significantly changes the behavior of T_c (P), it was thought that the anomalous T_c (P) of Re is associated with the pressure-driven change in Fermi surface topology of Re. Keep in mind that the discussion above is based on a weak-coupling BCS theory, but for most elemental metal superconductors, the electron-phonon coupling is intermediate or strong [29]. For unconventional superconductors, the situation becomes even more complex. More information can be found in references [30] and [31] which present extensive reviews of the effect of pressure on superconducting materials.

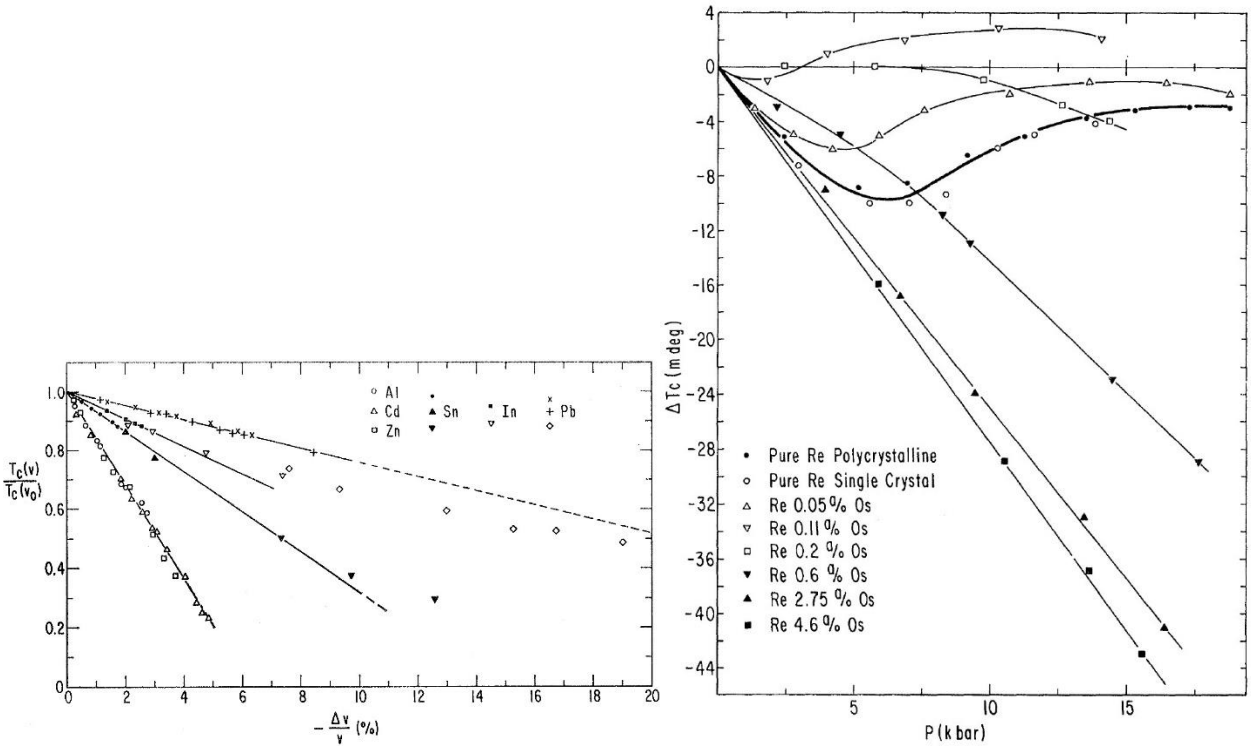

Figure 2.6: The relation between T_c and pressure for some elements. For simple metals including Al, Cd, Zn, In, Sn, and Pb, T_c(P) is shown in left. For Re with different contents of Os doping, T_c(P) is shown in right. The figure is taken from [27, 28].

Pressure can even induce superconductivity in elements that do not superconduct at ambient pressure. Figure 2.7 shows the periodic table of superconductivity, including 31 elements that superconduct at ambient pressure and an additional 23 elements that are only known to superconduct at high pressure. At ambient pressure only the lanthanide La is superconducting, whereas Ce, Eu, Yb, and Lu superconduct under high pressure. Of the alkali metals only Li and Cs are found to be superconducting at ambient or high pressure, respectively. Superconductivity in the alkali metals is of special interest since their Debye temperatures Θ_D are quite low (for Cs, Θ_D is only about 40 K, probably the lowest of all non-organic metals) and their densities of states $N(E_F)$ are not high due to their *s*-band nature, so their T_c would not be high according to Eq. (2.23). Indeed, not until 2007 was superconductivity in Li below 0.4 mK at ambient pressure reported [6]. However, high pressure boosts the T_c of Li to 14 K at 30 GPa, exceeding the T_c of Nb (~ 9.5 K), the elemental metal with the highest T_c at ambient pressure. In Cs the application of 12 GPa pressure is required for superconductivity to appear near 1.3 K. Further discussion about superconductivity in the alkali metals will be presented in Section 4.2.

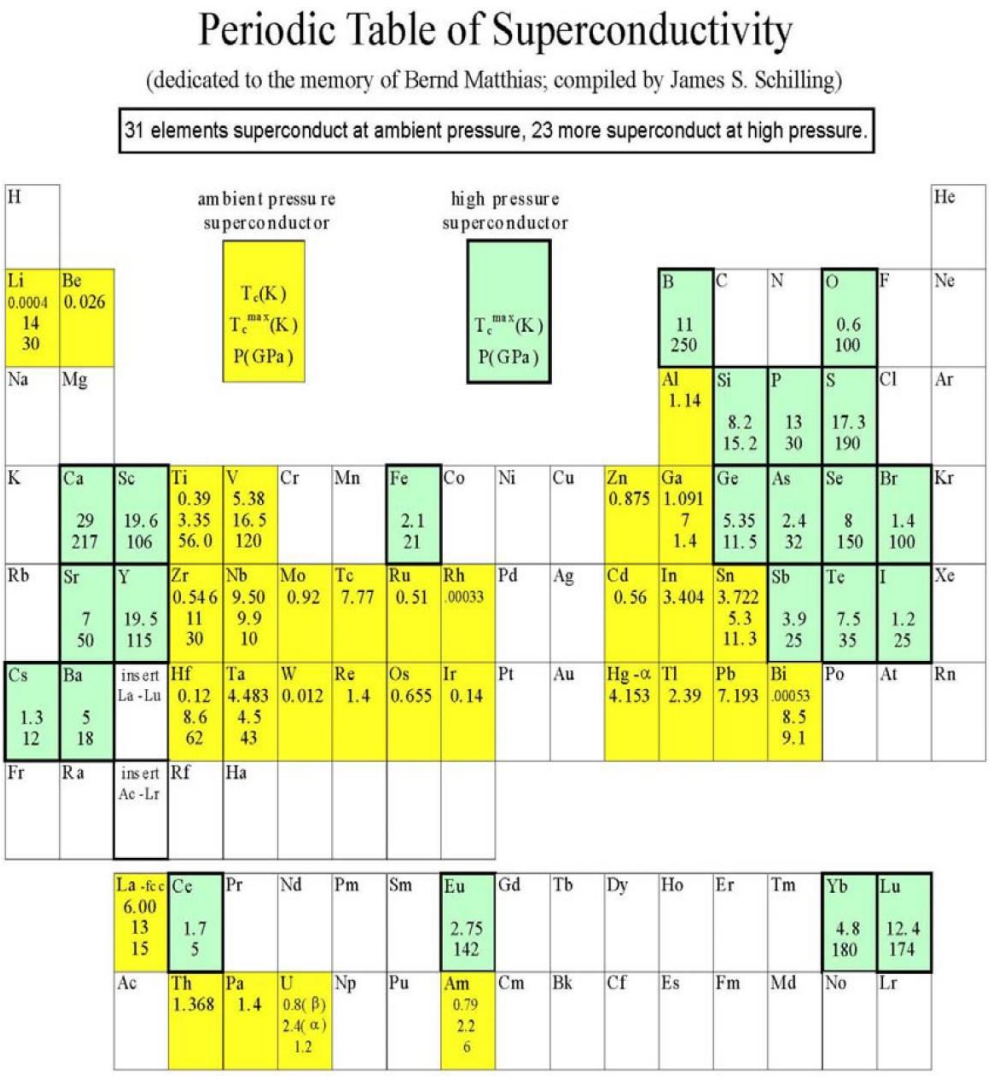

Figure 2.7: Periodic table of superconductivity. 31 elements superconduct at ambient pressure, marked in yellow; additional 23 elements superconduct at high pressure, marked in light green. The pressures of the highest T_c are given by P and T_c^{max}. The figure is taken from [32].

2.2.3Magnetic Impurities in Superconductors

Magnetism and superconductivity in metals are closely correlated since both states involve the alignment of the spins of conduction electrons either through the RKKY interaction or Cooper pairing. Except for the nonmagnetic lanthanides La, Yb, and Lu, the local-moment magnetism in the other lanthanide inhibits the appearance of superconductivity at ambient pressure. But by

applying high pressure, the RKKY interactions between ions in some lanthanides may be suppressed, allowing superconductivity to appear. Good examples include Ce and Eu, which undergo superconducting transitions when the pressure is higher than 5 GPa [33] and 80 GPa [34], respectively.

In view of the relationship between magnetism and superconductivity in lanthanides, researchers have developed a strategy to probe the magnetic state of lanthanides by alloying these in dilute concentration into a superconducting host. In 1958 Matthias *et al*. [35] measured the superconducting transition temperatures of 1 at.% rare earth solid solutions in lanthanum, the only lanthanide that superconducts at ambient pressure. As seen in Figure 2.8, the suppression of superconductivity seems to be correlated only with the spin of the solute atom. Also the suppression of superconductivity in La(Gd) obeys a linear function of the concentration of dissolved Gd for Gd concentrations below 1 at.%. The alloys La(2.5 - 10 at.% Gd) become ferromagnetic with Curie temperatures between 1 and 6 K [35] (see Figure 2.9).

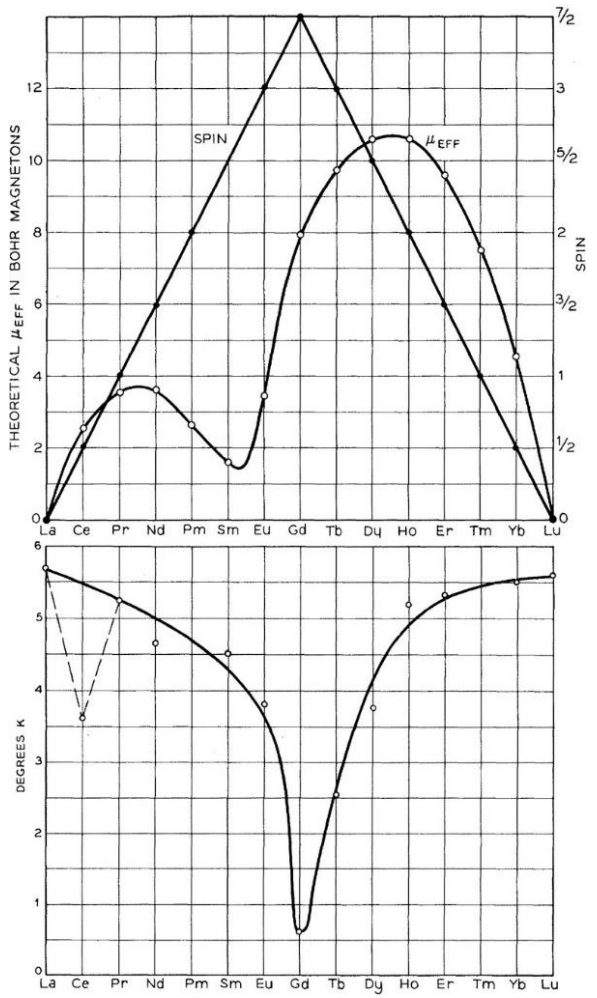

Figure 2.8: Spins and effective magnetic moments of lanthanides (upper) and superconducting transition temperatures of 1 at.% lanthanide solid solutions in La (lower). The figure is taken from [35].

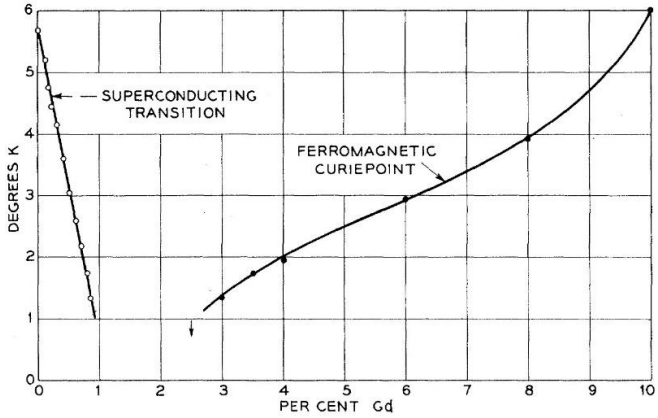

Figure 2.9: Ferromagnetic and superconducting transition temperatures of La(Gd) solid solutions. The figure is taken from [35].

In 1969 Maple *et al*. [36] reported a "sinkhole" like suppression in the pressure dependence of T_c for the dilute alloys La(Ce), as shown in Figure 2.10. The suppression effect reaches a maximum near 1.5 GPa, then continuously decreases until a saturation is reached above 10 GPa. A linear relation between the suppression and the concentrations of Ce is observed at low pressures and low concentrations. This phenomenon was attributed by Maple *et al*. [36] to the magnetic-nonmagnetic transition in Ce impurity under pressure.

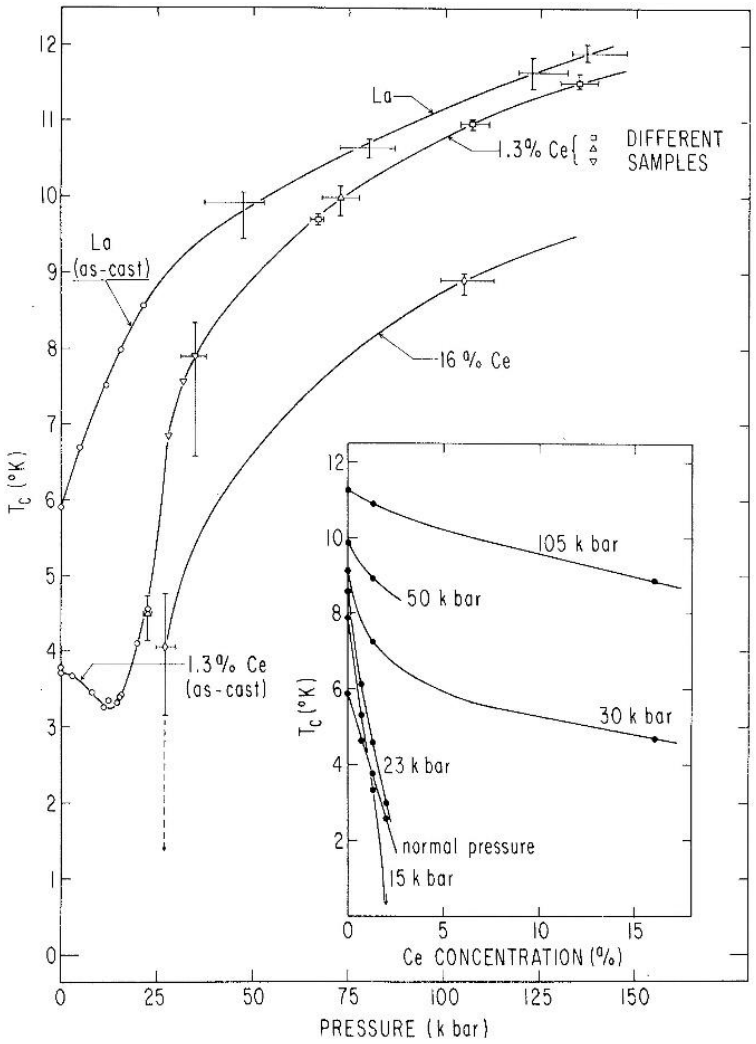

Figure 2.10: Pressure dependence of the superconducting transition temperature (T_c) of pure La and two La(Ce) alloys (1.3 and 16 at.% Ce) to 15 GPa. The vertical bars represent the transition widths rather than uncertainty of the temperature measurement and the horizontal bars the pressure inhomogeneity in the cell. Isobars of T_c versus Ce concentration for as-cast alloys are shown in the inset. The figure is taken from [36].

Abrikosov and Gorkov [37] gave a formula describing the initial decrease of T_c for superconductors doped with very low concentrations of magnetic impurities

$$k_B(T_{c0}-T_c)=\frac{c}{N(E_F)}\frac{\pi^2}{8}S(S+1)\gamma^2=\frac{\pi^2 c}{8}S(S+1)N(E_F)J^2 \tag{2.34}$$

where T_{c0} is the superconducting transition temperature of the host superconductor without doping, T_c the transition temperature with magnetic impurities, c the impurity concentration, $N(E_F)$ the density of states at Fermi level of the pure superconductor, S the magnitude of the impurity spin, and $\gamma = N(E_F)J$ the coupling constant between impurities and conduction electrons. For ferromagnetic coupling γ is positive while for antiferromagnetic coupling γ is negative. This Abrikosov-Gorkov formula (2.34), derived within the Born approximation for the scattering of electrons from magnetic impurities, accounts for the linear suppression with the concentration of impurities and the relation between impurity spins and the suppression. Corrections should be made when the Kondo temperature approaches T_{c0}, since then the Kondo resonance scattering most strongly influences T_c as the spin-flip amplitude responsible for the pair-breaking effect reaches its maximum. Further information about how magnetic impurities affect the transition temperatures of superconductors can be found in a review paper published by E. Müller-Hartmann and J. Zittartz [38].

How the Kondo effect influences the temperature-dependent electrical resistivity of metals has been discussed in Subsection 2.1.3. The Kondo effect appears if the coupling between magnetic impurities and conduction electrons J is negative, favoring the antiparallel alignment of conduction electron spins around impurity spins, leading to the breaking up of Cooper pairs (see Figure 2.11). As a result, a suppression of T_c of the host material due to the negative J, known as

the Kondo pair-breaking effect, is expected and indeed appears in La(Ln) [35, 36], as discussed earlier, and in Y(Nd, Sm, Tb, Dy) as will be presented in Subsection (4.1.3).

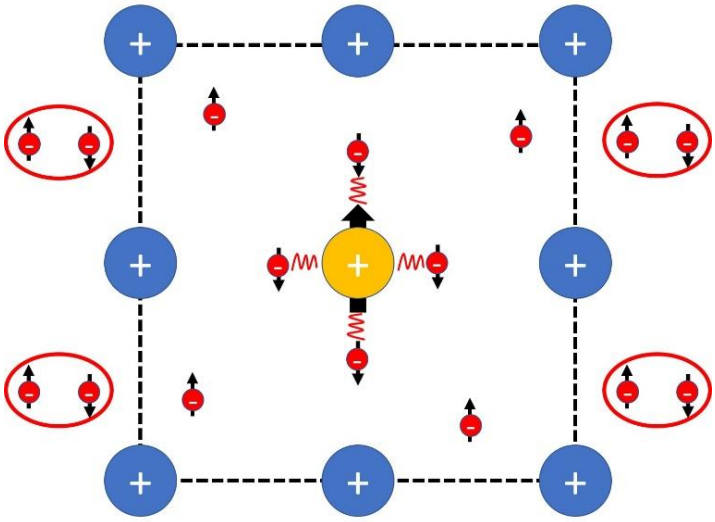

Figure 2.11: Kondo pair-breaking effect. The yellow circle represents a magnetic impurity doped in the host lattice marked by the blue circles. The small red circles represent the conduction electrons with either spin up or spin down. Near the impurities (the region enclosed by the dashed square), the negative *J* leads to an antiparallel alignment of the conduction electron spins around the impurity, destroying the Cooper pairs.

Chapter 3

High-Pressure Techniques

3.1 Helium Gas System

Unlike any other substance, helium remains liquid down to absolute zero at ambient pressure because the zero-point energy of helium is too high to allow freezing. To freeze liquid helium at a temperature above 1 K, a pressure of at least 25 bar is required. At a given pressure helium has the lowest freezing point among any fluid and provides nearly hydrostatic pressure even in the solid state. These facts make helium an ideal pressure transmitting medium to study materials under hydrostatic pressure.

Besides the points mentioned above, a He-gas high-pressure system has a number of advantages: (1) pressure can be changed hydrostatically at any temperature above the melting point of helium; (2) pressure can be measured continuously by a pressure gauge maintained at room-temperature; (3) the compressor can pressurize a large volume of gas/liquid so as to allow measurements on mm- or cm-sized samples. This compares with the micron-sized samples required for measurements in a diamond anvil cell (DAC), yielding, for example, only a very weak signal in the magnetic susceptibility. In a He-gas system, however, pressures only up to approximately 1.4 GPa can be generated, compared to the Mbar pressures in a DAC.

3.1.1 Helium Gas Hydrostatic Pressure System

A helium gas hydrostatic pressure system (see Figure 3.1) is built to generate nearly hydrostatic pressure up to 1.4 GPa (to extend the useful lifetime of the seals, the pressure is normally kept

below 1 GPa). Ultra-pure helium gas from a compressed gas bottle at 1,200 psi (80 bar) or more is fed into a two-stage membrane compressor (Newport Scientific) that can compress He gas to 1.7 kilobar (0.17 GPa). Then an oil-driven intensifier (Harwood Engineering) is used to increase pressure further to 1.4 GPa. The high-pressure gas is transmitted via a flexible copper beryllium (CuBe) capillary (inner diameter 0.3 mm and outer diameter 3.0 mm) to a CuBe pressure cell (Unipress, Warsaw) with a cross section shown in Figure 3.2. Since during the cooling period the volume/pressure of He gas decreases appreciably, an alumina spacer is often put in the cell together with the sample to reduce the volume of the cold He gas inside the pressure cell, thus reducing the decrease in pressure on cooling. An additional measure to minimize the reduction in pressure on cooling is to increase the volume of He gas at a constant ambient temperature by adding a 3.6 cm^3 "dead volume" in parallel with the pressure cell (see Fig 3.1).

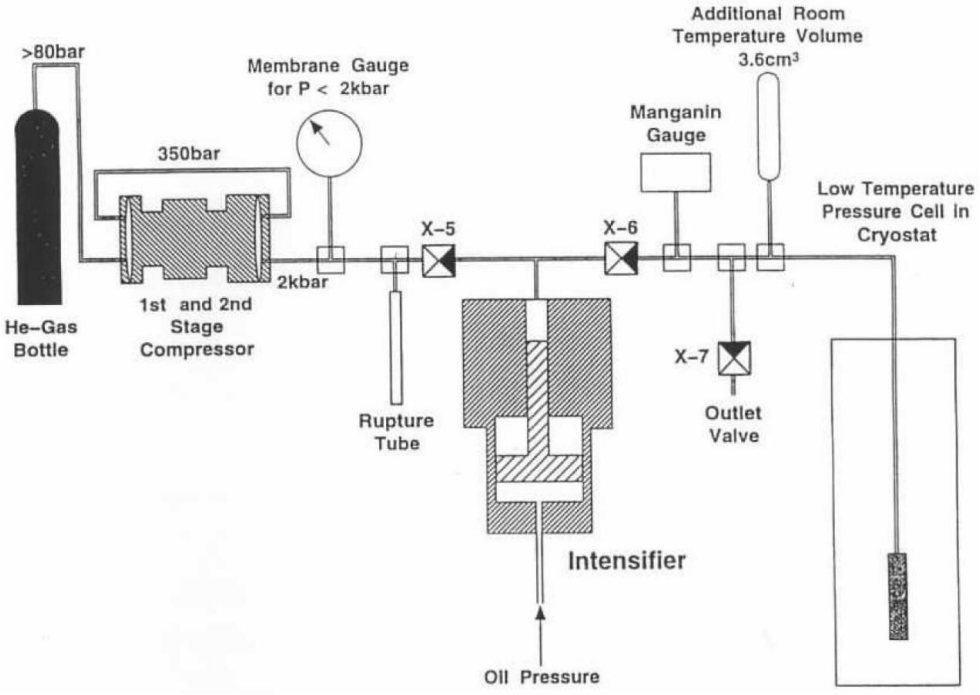

Figure 3.1: Schematic of He-gas hydrostatic pressure system. The valve X-5 should be closed when using the intensifier to prevent damaging the two-stage compressor. The additional room-temperature volume ("dead volume") is used to reduce the decrease in pressure when the pressure cell cools down. The figure is taken from [39].

CuBe gaskets coated with indium (Unipress) are placed between the pressure cell body and the electrical feed-through and capillary plug to seal the cell under high pressure. Recoating the gaskets with fresh indium shortly before the experiment has been found to improve sealing.

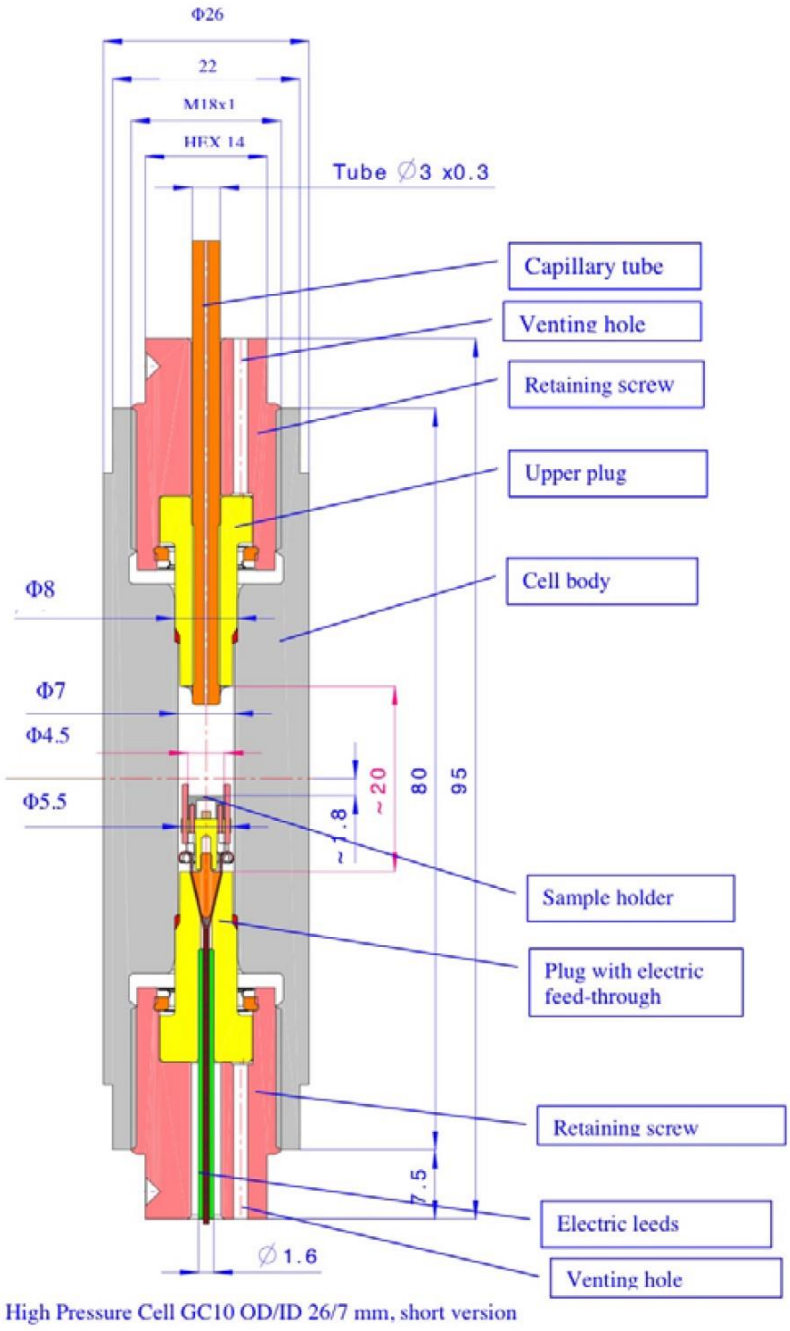

Figure 3.2: Diagram of the new gold-plated pressure cell acquired in 2009. The figure is taken from [40].

It's very important to test if the sealing of the system is good before starting a measurement. Serious leakage can result in failure of a coil system for ac susceptibility measurements or failure of contact points between electrical wires and samples in a resistivity experiment. Usually the leakage problem would become worse at higher pressure and lower temperature. The usual leaking locations are: the point where the capillary is connected to the He-gas compressor system as well as the gaskets and the electrical feedthrough in the pressure cell. There are two procedures to test for a possible leak. One is to test the feedthrough using a He gas leak detector (Varian) in the Glass Shop, Crow 101. A good feedthrough should not leak above 10^{-9} atm-cc/sec. The other procedure is to use a helium gas handy detector (Edwards), the so-called "sniffer", to detect leakage anywhere at He-gas pressures of several hundred bars or more.

A manganin gauge at room-temperature measures the gas pressure in the pressure cell for pressures above the melting point. When He becomes solid in the pressure cell, helium isochore curves are used to determine the pressure exerted by solid He on samples, which is somewhat lower than the reading of the manganin gauge. A platinum thermometer (for temperatures above 30 K) and a germanium thermometer (for temperatures below 30 K) are placed at the top at the pressure cell while a *Cernox* thermometer (calibrated from 1.3 K to room-temperature) measures the temperature at the bottom. *Apiezon N* grease can be used in a small amount on the surface of the thermometers to ensure good thermal contacts. Phosphor-bronze wires are wrapped around the top/bottom of the pressure cell and the capillary, acting as heaters to control temperature.

3.1.2 Janis Supervaritemp Bath Cryostat

Over the course of this thesis work, the Janis Supervaritemp Cryostat, together with a Balzer's rotary pump as seen in Figure 3.3, is used to vary temperature from 1.5 K to ambient. This Janis cryostat is a typical "gas-vaporizing" cryostat. It consists of several insulation layers, a liquid

nitrogen reservoir, a liquid helium reservoir (3.5 L), and a sample space separated from the reservoirs. It usually can sustain low temperature for 15-20 hours, consuming about 10 liters of liquid helium.

Figure 3.3: Pictures of the Janis cryostat (left) and the Balzer's pump (right).

The typical operation process beginning with the cryostat at room temperature is briefly described as follows. First, pump out the cryostat's insulation vacuum layer to about 10^{-5} mbar using the diffusion pump. It's recommended to pump overnight. Then insert the pressure cell into the sample space and insert the liquid helium transfer line (the cryostat half) into the helium reservoir. Connect the capillary to the He gas system using 40 lbs-inch torque and connect all electrical plugs and gas lines. Flush the sample space and the capillary three times and then fill liquid nitrogen in the outer reservoir several times and allow the temperature to decrease to about 150 K overnight. In the morning transfer liquid helium into the reservoir. Open the cold valve which controls the helium flow from the reservoir to the sample space and turn on the Balzer's

pump to the sample space. The cold He gas goes through the cold valve and cools the pressure cell. With this method, the temperature can go to about 4.2 K. For an even lower temperature, after collecting some LHe in the sample space, the cold valve should be closed and the needle valve that controls the pumping rate to the sample space should be tuned to get a proper cooling speed. How low a temperature can be reached depends on the pressure of the He gas is in the sample space (see the Figure 3.4 for reference).

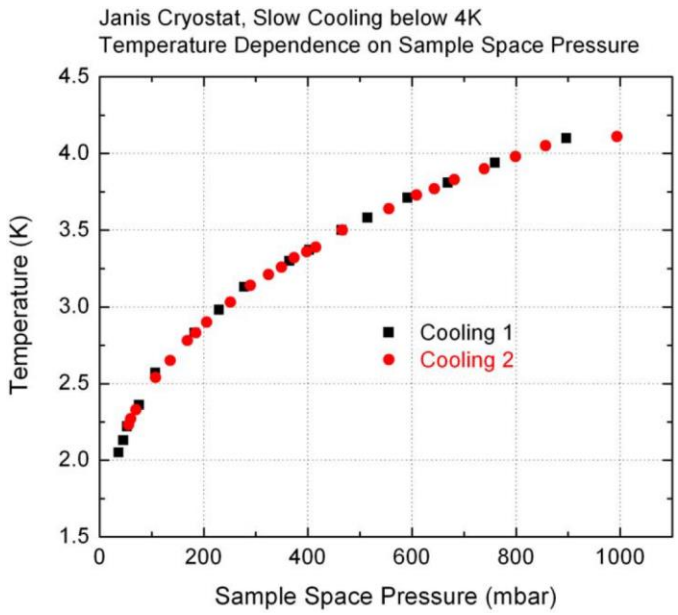

Figure 3.4: Plot of typical temperature vs. sample space pressure for slow cooling measurements below 4 K in the Janis cryostat. The figure is taken from [40].

Special attention should be paid when the temperature is close to the melting point (MP) of the high-pressure helium. For temperatures near the MP plus/minus 5 K, the cooling/warming rate must be controlled to be below 0.2 K/min, and the temperature of the capillary must be warmer than the temperature at the top of the cell that should be warmer than the bottom of the cell. If the temperature of the pressure cell passes through the MP too fast, helium solidifies quickly, grabbing anything inside it suddenly, a dangerous situation for the fragile electrical wires inside

the pressure cell. The correct temperature gradient across the pressure cell ensures the helium freezes from the bottom of the cell to the top (or melts from the top to the bottom). If not, the warm expanding helium at the bottom has nowhere to expand to because of the frozen helium at the top, and thus may blow past the bottom seal, thus jeopardizing the electrical connections in the cell. Good temperature control can be achieved by varying the cold valve, the needle valve, the heaters on the cell and the capillary, and the heater at the diffuser (under the pressure cell, which controls the temperature of the cryogenic He vapor).

3.1.3Mini-Coil for ac Susceptibility Measurements

Ac susceptibility measurements are very important in studying superconducting or magnetic materials. The basic concept is to use a magnetic field generated by an ac current to penetrate a sample and if the sample experiences a superconducting or magnetic transition, the field will be changed around it. According to Lenz's law, this change in magnetic flux can induce a current in a pick-up coil (the secondary coil), which results in a change in the voltage of the pick-up coil that can be detected by a lock-in amplifier. In the work presented in this thesis, a 0.1 mA, 1023 Hz ac current is used to excite a magnetic field of about 0.1 Oe in the coil system for the He-gas hydrostatic pressure experiment. The applied field should be low to avoid shifting or broadening the superconducting or magnetic transitions. Previously an SR830 lock-in amplifier was used to provide a constant voltage with a large external resistor in series with the primary coil (the one that generates the magnetic field) to provide a nearly constant ac current that varied slightly on cooling or warming. In 2015 a Keithley 6221 ac and dc current source was purchased capable of generating a constant ac current.

The mini-coil system used in this work is illustrated in Figure 3.5. Compared with the previous design, the distance between coils and the feedthrough is increased to minimize the possible

magnetic influence from the metal feedthrough. The holder is made of *Vespel* (Dupont), a nonmagnetic material. Two secondary coils are wound in opposite directions around the holder and the primary coil is wound on top of the secondary coils. After balancing properly, this coil system gives nearly zero voltage signal, giving a nonzero signal when the magnetic flux inside the secondary coil changes due to the sample becoming superconducting or ordering magnetically. In experiments usually a superconductor like NbTi ($T_c \approx 10$ K) or MgB_2 ($T_c \approx 39$ K) will also be placed in one secondary coil and the sample in the other. This helps to determine the correct reference phase angle of the lock-in by balancing the left/right side of the signal peak in the imaginary part versus temperature curve of the calibrant superconductor.

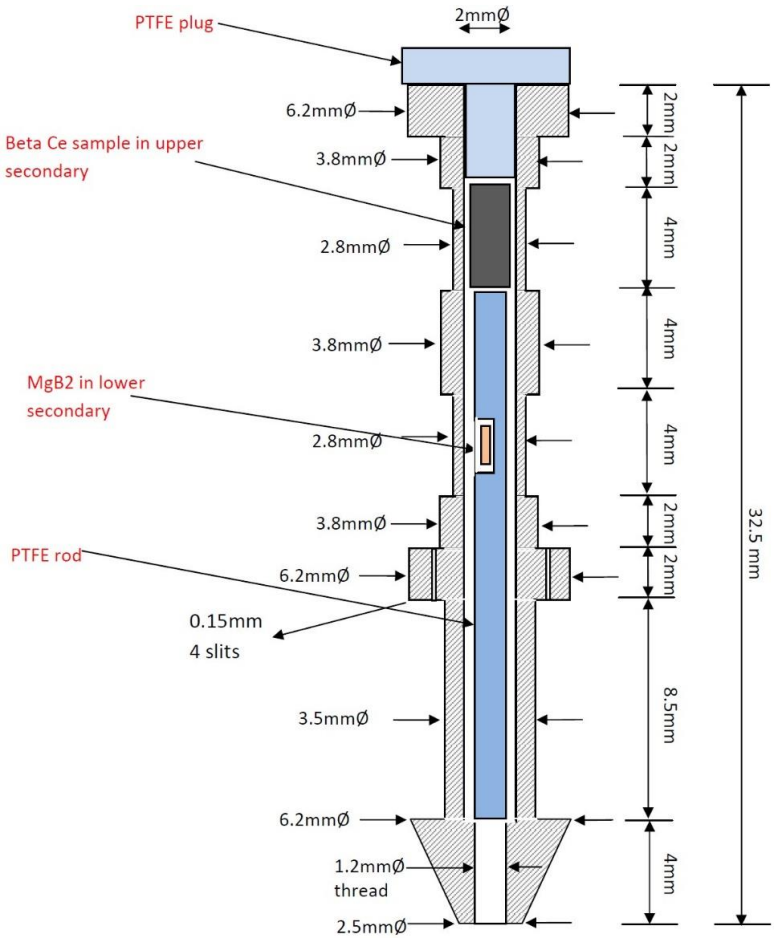

Figure 3.5: The mini-coil system for ac susceptibility measurements in He-gas hydrostatic pressure system. The figure is from Pallavi Malavi.

Due to the fact that both the primary and the secondary coils are wound using 60 μm copper wires, much patience and time (perhaps five days) are needed to finish a coil system. The ends of the coils are attached with non-superconducting cadmium solder to the four pins of the feedthrough. To avoid the destruction of the joint points by the compressed solid helium, a slow cooling/warming rate (below 0.2 K/min) near the melting curve of helium and a small temperature gradient (below 2 K) between the top and the bottom of the pressure cell are necessary.

3.2 Diamond Anvil Cell

During the first half of the 20th century, Percy Williams Bridgman developed a system of opposed anvils, known as the Bridgman anvil device, to study physics under pressures to several GPa. His work is revolutionary since the previous pressure record was only about several kbar (1 kbar = 0.1 GPa). In 1950s Charles E. Weir, Alvin Van Valkenburg, Ellis R. Lippincott, and Elmer N. Bunting at the National Bureau of Standards (NBS) created the diamond anvil cell (DAC) [41], which replaced the tungsten carbide anvils in the Bridgman anvil with diamond anvils, extending the pressure region to above 100 GPa (Mbar).

3.2.1 Diamond Anvil Cell

Diamond is the hardest known natural material due to its super strong covalent bonding between carbon atoms, which makes it highly thermally conducting and chemically stable as well. It is also optically transparent over a wide spread of wavelengths. All these properties make diamond a premium material in high-pressure science: its hardness provides the possibility to create ultra-high pressure; its chemical stability avoids reactions between it and materials under its compression; its transparency facilitates visual observation and various optical measurements at

high pressure. Actually, many advances in high-pressure science are firmly related to the invention of the diamond anvil cell (DAC), in which a pair of diamond anvils are the core, and the static pressure at the megabar level (the highest pressure obtained in a DAC is reportedly 7.7 megabars! [42]) can only be achieved by using a DAC.

Though diamonds are very tough, they still contain several kinds of impurities or defects such as boron, nitrogen and lattice defects, which can cause the diamond anvils to shatter at high pressure. Even laser radiation can induce the failure of diamonds. V. Tissen informed us of an empirical formula developed by Dunstan and Spain [43]: P_{max}(GPa)= 12.5/d^2(mm), where d is the diameter of the culet, to estimate the maximum pressure a diamond anvil can reach. Unfortunately, many diamond anvils fail before this limit due to inaccurate alignment and internal defects. It is thus important to examine the diamond anvils carefully before committing them to a high-pressure experiment. We use cross-polarizers to observe internal strain fields. Fix one of the cross-polarizers to the stereoscopic microscope (*Nikon* SMZ-U) and put the diamond anvil, which is illuminated from below, on the other cross-polarizer. Rotate the cross-polarizer on the microscope to make it 90 degrees out of phase with the other one. Any observable features indicate defects. See Figure 3.6 for an example of defects in a diamond anvil.

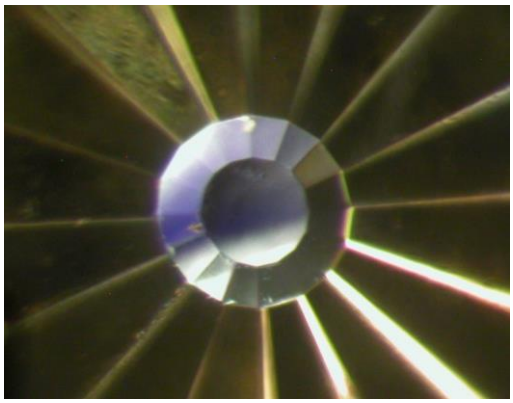

Figure 3.6: Strain in diamond anvils, making them more likely to fail. The defects can be observed through cross-polarizers. A diamond without strains inside should look clear and uniform.

High-pressure DAC experiments in the course of this thesis were carried out by using diamond anvil cells made of hardened CuBe (Schilling 1984). Figure 3.7 (upper) shows the schematic of this cell. A stainless-steel diaphragm, placed between the force plate and the piston, can be filled with ultra-high purity helium gas through a capillary connected to a gas bottle. The diaphragm expands slightly when filled with He gas, thus pushing the piston up, generating a pressure between the diamond anvils. The area of this diaphragm is approximately 19 cm^2 whereas the culet area is only about 10^{-3} cm^2 (for a 0.18 mm diameter culet), so 1 bar in the diaphragm generates 20 kbar on the culet. The pressure can be increased in the diaphragm at any temperature above the melting point of liquid helium. This is a big advantage over the mechanically loaded DAC system where the DAC must be taken out of the cryostat and loaded at room-temperature. A low-temperature gear box can also be used.

The diamond anvil (purchased from either d'Anvils or Almax, 1/6 carat, 16 facets, about 2 mm height) sits on a punctured 25 μm thick zirconium foil, to minimize local stresses on the diamond table under pressure, and then glued onto a non-magnetic tungsten carbide (WC) backing piece with epoxy (Stycast 2850 FT black and catalyst 24 LV). The WC can withstand pressures of 5 to 10 GPa and can deform somewhat under pressure to prevent the possible development of micro-cracks on its surface. Before use, the WC backing piece should be polished using 30 μm diamond sandpaper to ensure the surface, especially near the optical hole where the diamond anvil sits, is flat and crack free. Then translational, rotational, and planar alignments should be made on the diamond anvils. The precision of these alignments is crucial in order to maximize the pressure. The basic idea of planar alignment is to observe the interference stripes of two anvils under the stereoscopic microscope. When two anvils are parallel to each other by adjusting the three screws that control the tilt of the hemisphere at the top of the piston, the

colorful interference stripes disappear. After all alignments are satisfactorily completed, a gasket will be built on the diamond anvil of the piston.

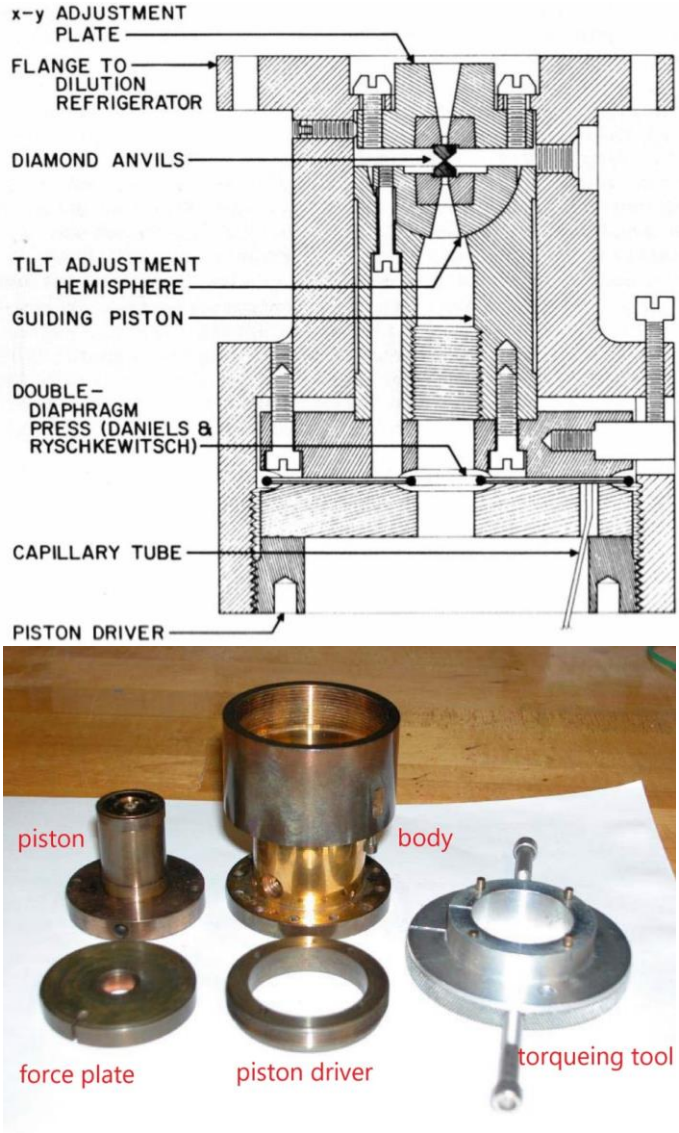

Figure 3.7: Cross-sectional schematic of the DAC designed by J. Schilling [44] (upper) and pictures of DAC set (lower). The set includes piston, body, force plate (placed between the piston driver and the diaphragm), piston driver, and torqueing tool (for the piston driver) [45].

3.2.2 Gaskets

The gasket for DAC high-pressure measurements is a thin sheet of metal between diamond anvils, with a hole where the sample, pressure transmitting medium, and ruby spheres can be

placed. Additionally, the gasket supports the diamond anvils and protects the edges of the anvils. The extremely high-pressure environment requires a gasket to be both hard and ductile. If a gasket is too soft, it would become very thin under high pressure leading to the destruction of the sample chamber. Materials that are hard but brittle such as ceramics are not suitable as a gasket either, since micro-cracks form and grow in these materials due to their poor plastic deformation ability, resulting in diamond anvil failure.

Besides the mechanical requirements, gaskets should also be neither magnetic nor superconducting if they are used in ac susceptibility measurements. The secondary coil in the coil system picks up signals from materials both inside and near the coil, which means most of the signal originates from the gasket since the sample is very small compared with the gasket. If the gasket is magnetic in the temperature range of interest, its large response to the magnetic field will overwhelm the small change in signal from the tiny sample. If the gasket is superconducting, below its critical temperature it expels the magnetic field near it, making the ac susceptibility measurements impossible. Several kinds of materials are often used in experiments: rhenium (Re), CuBe, NiCoCrMo alloy (MP35N), NiMo alloy, NiCrAl alloy (Russian alloy). 250 μm thick Re foil is the most often used gasket material for resistivity measurements over the course of this thesis because it allows pressures to at least 170 GPa and because of its high hardness (51 HRC) and low magnetic response. It becomes superconducting at 1.7 K and T_c increases to about 4 K under shear stress, limiting its use in ac susceptibility experiments below 4 K. For ac susceptibility measurements, CuBe (41 HRC after annealing) and MP35N, neither of which superconduct above 1.3 K, are used. Both of them have been used to pressures as high as 150 GPa.

Gaskets should be pre-indented before using, because the gasket material outside diamond anvils supports the squeezed part between two anvils and also protects gaskets from large deformations and instability of the hole. Usually, the final thickness after pre-indentation is about 1/6 of the diameter of the diamond anvil culet. Use a torque wrench to apply force to the gasket and rotate the tool by 10 degrees each time, then rotate it back by 5 degrees to prevent cold-welding between diamond anvils and gasket. After pre-indentation make sure there are no cracks in the pre-indentation area, otherwise pre-indent another gasket. A hole drilled at the center of the pre-indentation of the gasket by electrical discharge machining technique (Hylozoic Products micro EDM system) technique is used to hold samples. The drilled hole should be about half as big as the diameter of the diamond anvil culet, circular and centric.

To verify that the sample does not short with the gasket in resistivity measurements under high pressure, two flattened 80 μm diameter Pt wires are spark-welded onto the gasket and then covered by silver paint. A piece of Scotch tape is then used to cover the entire gasket, isolating the gasket from the four Pt strips which will be put on the Scotch tape. A hole in the tape around the pre-indentation area should be hollowed over before filling the pre-indentation area with cubic boron nitride (cBN)-epoxy powder. The powder is compressed to make an insulation layer on the surface of the pre-indentation area, to isolate it from the sample or electrical leads. Put some *krazy glue* on the edge of the insulation layer to strengthen it.

Depending on the hardness of the samples, two different types of sample chambers are suitable. For soft or fluid materials such as cesium, a bowl-style sample chamber is made whereas for relatively stiff materials such as samarium, a flat sample chamber works best (see Figure 3.8 for more details). As for the bowl-style sample chamber, a bowl is drilled at the center of the insulation layer with a diameter about 1/3 of the diamond anvil culet. A micro-drilling system

(Minitool inc.) equipped with a spade-shape carbide drill bit is used to drill the bowl. Unfortunately, this system cannot control the depth of the bowl, so a lot of attention and patience has to be paid to obtain a bowl with a sharp edge rather than a hole in the insulation layer. After this a 4 μm thick Pt strip is fixed on the gasket by a small piece of tape, with its tip pointing to the center of the bowl. Its position is adjusted so that after closing the cell, a part of its end hangs above the bowl. When the Pt strip takes the shape of two diamond anvils (this can be achieved by keeping the cell closed for about half an hour), some glue from the Scotch double-sided tape is deposited between the strip and the insulation layer and the cell is closed again for half an hour. In this way the strip can be fixed onto the insulation layer, which facilitates loading samples into the bowl. A needle is used to push the part of the strip above the bowl onto the wall of the bowl. Then repeat this process for the remaining three Pt strips. When the soft/fluid sample is loaded into the bowl, the four Pt strips on the wall act as electrical leads. For the flat style sample chamber, after making the insulation layer, some cBN-epoxy powder is put on the culet area and the cell is closed. The body is pushed against the piston by hand, to make a loose, fresh insulation layer, which is stickier than the torque-tool compressed layer. A small Pt triangular strip (~80 μm high, 30 μm wide, with ~5 μm wide point) is placed in the culet area and the cell is closed to make the strip firmly attached to the insulation layer. Make sure the triangle is pointing to the center of the culet and about 10 μm away from the center. Then the same thing is done for the remaining three small Pt strips. Four big Pt strips are rested on the gasket and their positions are adjusted so that when the cell is closed, the ends of the four big strips touch the small Pt strips. The sample will be put on the four small strips. The big strips will be soldered to the copper wires in the electrical board that is fixed on the piston. Figure 3.9 gives a photograph of a gasket ready for a high-pressure resistivity measurement.

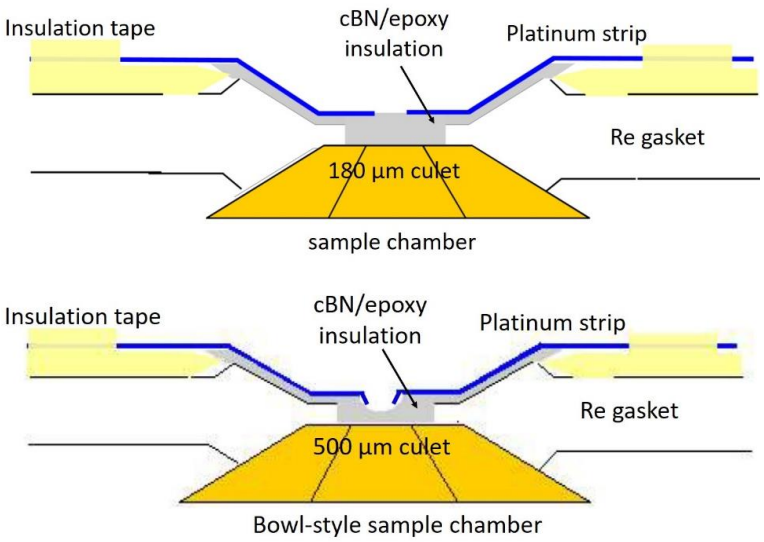

Figure 3.8: (upper) Schematic of the normal gasket for resistivity measurements on lanthanides such as Sm and (lower) the bowl-style gasket for measurements on alkali metals such as Cs and Rb. The soft alkali metals are confined in the bowl made of compressed cBN-epoxy layer. Both kinds of gaskets are based on the design by Shimizu group, Osaka University [46].

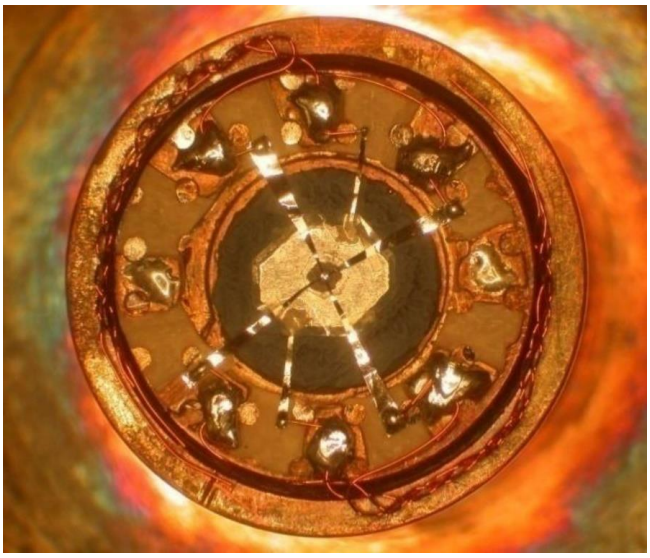

Figure 3.9: The picture of a gasket mounted by clay at the center of a circular electrical board, on the piston of the DAC. After closing the DAC, the copper braids consisting of two voltage wires, two current wires, and two wires for testing whether the gasket contacts the sample, will be carefully pulled out from two holes drilled through the body of DAC using a tweezer.

3.2.3 Resistivity Measurements

During the course of this thesis, the resistivity measurement is the main tool to determine the transition temperature of superconductors. Compared with the ac susceptibility measurements, the resistivity measurement is more sensitive to detect superconductivity. This is because it allows us to find a superconducting transition even if only a small part of the sample becomes superconducting. In addition, ideally a resistivity measurement only collects signals from the sample, whereas the ac susceptibility technique collects information near the coil system, including the sample and other materials such as backing pieces, Zr foil, and the high-pressure cell. The background signal in the ac susceptibility from these materials sometimes makes the data analysis difficult. As a very common but useful characterization method, by fitting the temperature-dependent resistivity to different polynomial functions, information about the sources of the resistance can be obtained. The overall shape of the resistance versus temperature curve is extremely informative as well: an upturn of the curve with decreasing temperature may suggest a Kondo effect whereas a sudden drop of the curve with decreasing temperature may mark a magnetic ordering transition due to a reduction of the magnetic scattering.

In order to measure resistance, a four-point probe method is applied. Four platinum strips on the sample act as voltage/current electrodes. Jing Song in our group has confirmed that platinum foil does not superconduct up to about 170 GPa, as shown in Figure 3.10. Usually, a dc current output by Keithley 220 programmable current source is polarized by a switch box, then sent to two current leads on the sample. The voltage across the sample is measured by a Keithley 182 sensitive digital voltmeter. For samples with very small resistance at low temperature (0.1 mOhm level), a 17 Hz ac current provided by a Keithley 6221 dc and ac current source is applied

to the sample, and an SR830 DSP lock-in amplifier is used to measure the ac voltage after an SR554 pre-amplifier. This ac method filters noises off to obtain better-quality data.

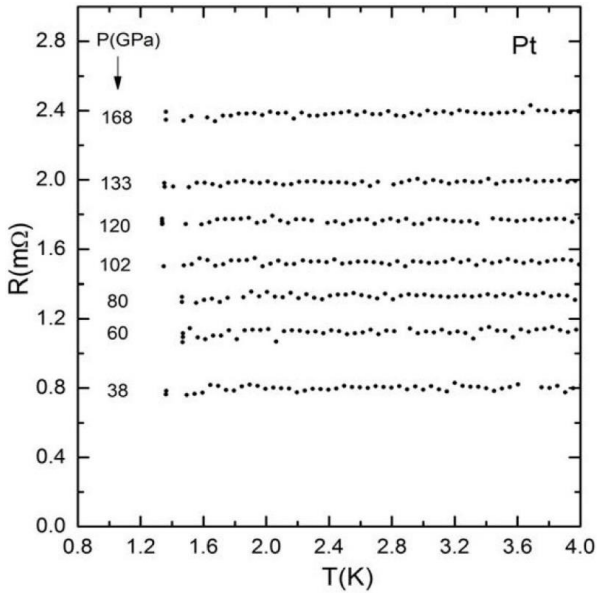

Figure 3.10: Temperature-dependent resistance of Pt foil to 1.35 K at pressures to 168 GPa. No superconductivity was observed [32].

After preparing a gasket, loading the sample and closing the pressure cell, the cell is attached to the cryostat insert, the diaphragm capillary attached to the insert, and all electrical wires connected. Then the cryostat insert with pressure cell is lowered into an Oxford “flow” cryostat whose schematic illustration is shown in Figure 3.11. A transfer line from Cryo Industries of America connects a liquid helium (LHe) dewar and the arm of the cryostat. A membrane pump is used to pump LHe from the dewar, through the transfer line to the cryostat. The outer insulation layer of the cryostat needs to be at high vacuum before starting a transfer. When inserting the transfer line, I would push the inflated balloon of the cryostat gently to avoid air to be pumped into the cryostat (it should have been flushed by He gas three times). A *Cernox* sensor near the cell measures the temperature of the sample.

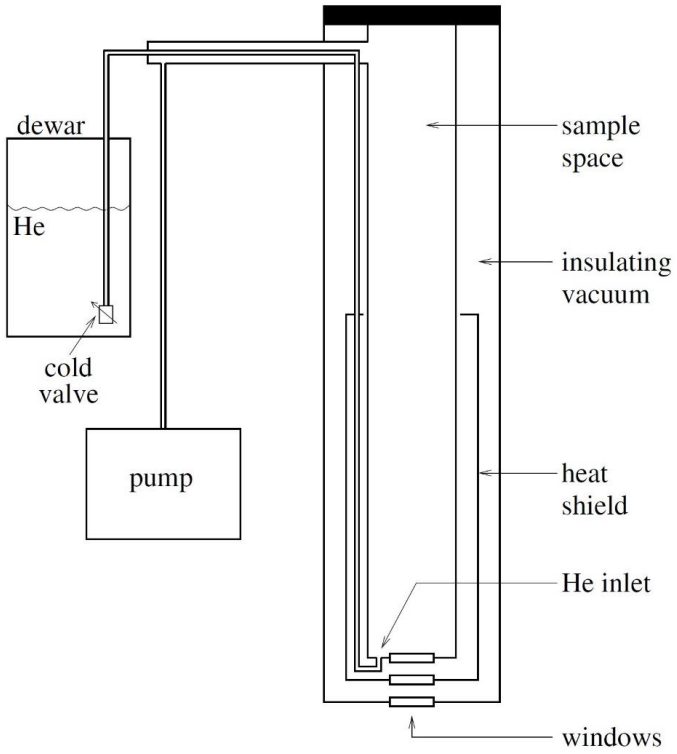

Figure 3.11: Schematic of Oxford Instruments continuous flow cryostat (not to scale). Also shown are the pump and LHe dewar. The cell is optically accessible through sapphire windows at the bottom of the cryostat. The figure is taken from [47].

By using the membrane pump, cooling from room-temperature to LHe temperature can be achieved in about two hours. The cooling rate can be controlled by the VC30 flow regulator connected to the transfer line, the cold valve on the transfer line, and the heating power of a heater inside the cryostat. When the temperature is about 4.2 K, if a lower temperature is desired, some LHe (about 2 inches above the cell or even more) is collected at the bottom of the cryostat first, then the transfer line is taken out and a plastic insert is plugged in the arm of the cryostat, and the cryostat is pumped on slowly with a mechanic pump (lowest temperature ~1.5 K) or a roots pump (lowest temperature ~1.3 K). About 1.5 hours to go to the lowest temperature is desirable since cooling too quickly may add noise to the measurement. After reaching the lowest temperature, the roots pump or the mechanic pump is closed gradually to allow a slow warm-up

(so called drift warming). When the temperature rises to about 50 K, it is often necessary to break the outer vacuum layer by about 0.2 torr to accelerate the warming process so that it returns to room-temperature after about 12 hours. Usually, the cooling data from room-temperature to 4.2 K is noisier than the drift warming data because of vibrations from the membrane pump, but the cooling data from 4.2 K to 1.3 K is preferred over the warming data because sometimes LHe runs out before the temperature comes back to 4.2 K during warming, thus destabilizing the warming process.

3.2.4 Ac Susceptibility Measurements

The ac susceptibility technique for the DAC system is in principle the same technique as for the He-gas hydrostatic pressure system. Both employ the same lock-in amplifier, pre-amplifier, and ac current source. Instead of the mini-coil system used in He-gas hydrostatic pressure system, a side-by-side coil originally designed by V. G. Tissen is used in the DAC system. The primary coil can generate a 3.0 Oe magnetic field for an excitation current of 6.8 mA (rms) and the secondary coil picks up the signal from the sample. Unfortunately, though this coil system can detect superconducting transitions, experience from Jing Song's Nd ac susceptibility measurements shows that it is not sensitive enough to detect antiferromagnetic transitions.

The side-by-side coil system is made of two identical counter-wound coils, each containing an inner secondary coil and outer primary coil. Figure 3.12 shows a photograph of a coil system wound by the author. The whole coil system is glued on a ~0.7 mm thick fiberglass board with crazy glue (between the coil and the board) and GE varnish (between the extended wires and the board). The board is designed so that through the central hole of the board one coil will be centered at the diamond anvil and the sample. The other coil has a "dummy" gasket inside it,

which is the same as the gasket for the sample and compensates the signal from the sample gasket.

Figure 3.12: Custom coil system for ac susceptibility measurements in the DAC. The central coil is for samples to be measured and the side coil is for a dummy gasket that compensates the magnetic susceptibility signal from the gasket in the central coil.

A set of tools, as seen in Figure 3.13, was developed to prepare the coil system, including a brass pin, two Teflon disks, a stainless-steel tube and a brass holder. The whole set should be attached firmly to a number counter. 60 μm copper wire with insulation coating is drawn from a spool and wound tightly around the stainless-steel tube which had been coated with Teflon spray TFL 50 *dry lube* to facilitate taking the coil off from the tube once the coil is finished. Altogether, 6 layers, each layer ~30 turns copper wire, are wound to form a secondary coil. A primary coil is wound on top of the secondary coil, also containing 6 layers with ~30 turns per layer. When one layer is finished, paint the layer with GE varnish diluted with ethanol and allow it to dry before starting the next layer. In this way the layer will become tough and self-supporting. When a coil is complete, paint it with GE varnish again and leave it for two days. Remove the coil from the stainless-steel tube carefully and put GE varnish on the inner, top and bottom side of the coil. Repeat the same procedure for the other coil. Spark weld the two side coils inversely so that the voltages generated in the two secondary coils cancel out.

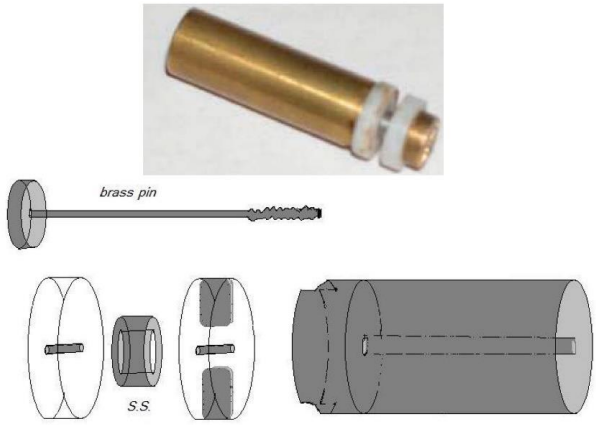

Figure 3.13: The coil winding rig used for winding the side-by-side coil system.

Before using the coil system, it is best to test the background signal of both coils together at room-temperature with no magnetic materials nearby. Fix the coil onto an electrical board, connect the primary/secondary coil to an ac current source/lock-in amplifier, and set the reference phase angle of the lock-in amplifier using a ferrite (see below). A well-balanced empty coil should give a voltage no larger than ~100 μV after 100 times pre-amplification in the X channel, given that a 675 Ohm resistor is in series with the primary coils and a 1023 Hz, 5 V ac voltage is applied to the primary coil. If the remaining voltage in the X channel is above 100 μV, some of the outer turns in the primary coil can be removed. A ferrite sample can also be used to set the phase angle of the secondary coil system. On inserting the ferrite into one coil, the reading in the X channel should show s sizable increase, with no change in the Y channel. If there is a voltage change in the Y channel, the phase angle should be adjusted until the change in the Y channel becomes zero as the ferrite is inserted or removed.

3.3 Pressure Gauges

Many methods have been developed to determine the pressure generated in a DAC apparatus. In the early days, pressure was often estimated from the applied load. This method is not very

reliable especially if a gasket is used since it absorbs much of the load. The electrical resistance of some materials can also be used to estimate the pressure, such as the superconducting transition temperature of lead under pressure [48] or the semiconductor-metal transformation of II-VI or III-V semiconductors [49]. Electrical resistance measurements require bringing electrical contacts inside the high-pressure region to the sample, a difficult task in many cases. Due to the excellent optical transparency of diamond, optical pressure gauges are ideal in DAC measurements. The pressure-dependent equation of state of some materials such as NaCl and gold [50, 51], measured by X-ray diffraction, is a powerful tool to determine pressure. The main drawbacks of this method are the expense of the X-ray diffractometer and the long data acquisition time. Nowadays, most high-pressure research groups use ruby fluorescence and the diamond vibron as the main manometers in a DAC apparatus to megabar pressure. These two techniques are those used to measure pressure in the present dissertation research.

3.3.1 Ruby Fluorescence

In the 1970s scientists at the National Bureau of Standards discovered that the sharp fluorescence peaks of ruby (Cr^{3+} doped Al_2O_3) display a large, almost linear red-shift under pressure [52] that can be used as an excellent pressure gauge in DAC high-pressure experiments. The fluorescence intensity from a small ruby chip is sufficient to easily determine pressure using only a laser and simple spectroscope. The ruby spheres used in the present experiments have been annealed to eliminate internal stress [53].

The ruby fluorescence originates from the photon emissions between energy bands of Cr^{3+} in the crystal field of Al_2O_3 (see the energy level diagram of Cr^{3+} in ruby presented in Figure 3.14). Through the absorption of a blue or green photon, ruby in its ground state $^4A_2$ can be excited to the Y or U band. Through a non-radiative decay (phonon emission) the meta-stable ^2E states will

be populated. The radiative decay (photon emission) happens when states decay from ^2E back to the ground state $^4A_2$, resulting in the ruby fluorescence peaks R_1 and R_2 centered at 694.3 nm and 692.8 nm under ambient conditions, respectively.

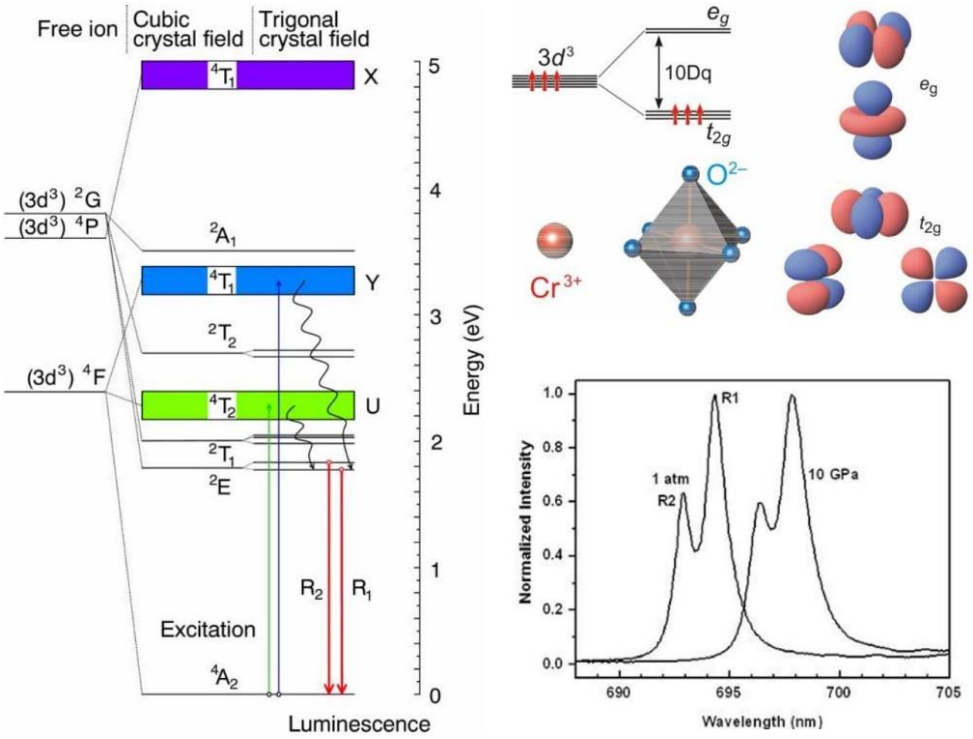

Figure 3.14: Energy level scheme of Cr^{3+} in ruby [54]. The lowest-energy free-ion multi-electron state of Cr^{3+} is a high-spin state (^4F); one of the excited states (^2G) is low-spin. The ligand field effects on the free-ion states are dominated by the octahedral crystal field component. The trigonal field in combination with spin-orbit interaction results in additional splittings. The ^2E levels are split by ΔR_{12} = 29 cm^{-1}; the rather small splitting of the $^4A_2$ ground state by 0.38 cm^{-1} is not shown here.

The shape and the location of R_1 and R_2 lines change with temperature as well. When temperature decreases, the population of the lower ^2E state is preferred, which means the intensity of the R_1 line will be enhanced while that of the R_2 line will be suppressed. Since the work in this thesis focuses on the low temperature properties of materials, the R_1 line is used as manometer. The temperature dependence of the R_1 line between 0 and 300 K was determined by Buchsbaum *et al*. [55]:

$$\upsilon_0 = 14422.0 - 36.612t^{3/2} + 169.77t^2 - 265.54t^{5/2} + 112.14t^3, \quad (3.1)$$

where υ_0 is in cm^{-1} the frequency of the R_1 line at zero pressure and $t = T/(300\ K)$, the reduced temperature. Despite the shift of the R_1 line with temperature, it was found that the pressure dependence of the R_1 line is independent of temperature, thus making it easy to determine the pressure at a given temperature [56]. A number of ruby fluorescence calibrations have been proposed, such as MXB86, a popular standard by Mao *et al*. in 1986 [57]. In this thesis a more recent calibration (CNSS05) to 150 GPa under quasi-hydrostatic conditions is applied [58]:

$$P(GPa) = \frac{1876}{10.71}\left[\left(\lambda/\lambda_0\right)^{10.71} - 1\right], \quad (3.2)$$

where λ_0 is the wavelength of the R_1 line at ambient pressure. The comparison between these two standards is given in Figure 3.15. In an actual measurement a small piece of reference ruby is placed on the backing piece and its R_1 line at a given temperature will be considered as λ_0. The wavelength of the R_1 line of a ruby sphere in the sample chamber is measured as λ so that we can calculate the sample pressure using the above formula.

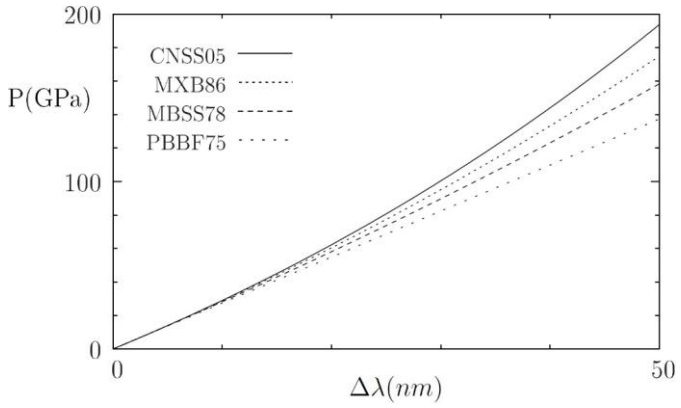

Figure 3.15: Comparison of different ruby manometer calibrations. Pressure versus wavelength shift in the R_1 ruby fluorescence peak is shown according to different calibrations. The CNSS05 standard is mainly used in the thesis. The figure is taken from [47].

Above 1 megabar the fluorescence of ruby becomes increasingly weak and broad, making it difficult to use as manometer. In order to determine the pressure well into the megabar region, where diamond anvils with small culets are selected, the amount of ruby has to be small and the fluorescence intensity is weak. If the power of the exciting laser is increased to counteract this, the heating effect may cause the diamond anvils that are already under high stress to shatter. In addition, the ruby bands Y and U shift to higher energy with pressure, requiring lasers with shorter wavelength to populate the Y and U bands. For pressures of 250 GPa and above photons with sufficient energy are strongly absorbed by the diamond anvils themselves [59] preventing the use of ruby as manometer. Additionally, above 120 GPa the fluorescence from diamond itself appears, giving a strong background to ruby fluorescence which makes it hard to resolve the R_1 peak [60]. Megabar pressures not only strongly weaken the ruby fluorescence but also broaden the peaks due to shear stresses from non-hydrostatic pressure media. A superior manometer for pressures above 1 Mbar is the frequency of the diamond vibron at the center of the culet directly adjacent to the sample.

3.3.2Diamond Vibron

Since its first observation by K. S. Krishnan and C. V. Raman in 1928, the Raman effect has become a powerful method to study the inelastic scattering of light in materials. It can detect the phonon modes, thus providing structure and chemical bonding information on materials. When a photon excites a material, this excitation puts the material into a virtual energy state for a short time before a photon is reemitted. Most molecules/atoms will decay from the virtual energy state back to the initial ground state, emitting photons with the same wavelength, the so-called Rayleigh elastic scattering. Only a small fraction of molecules/atoms ($\sim 10^{-7}$) jump from the virtual state to higher vibrational/rotational states rather than to the initial state, emitting energy

in the form of light with longer wavelength. This is the Stokes inelastic scattering. The other kind of Raman scattering, the anti-Stokes inelastic scattering, involves energy transfer from higher vibrational/rotational states to lower ground state, emitting light with short wavelength. Figure 3.16 illustrates how Raman scattering happens.

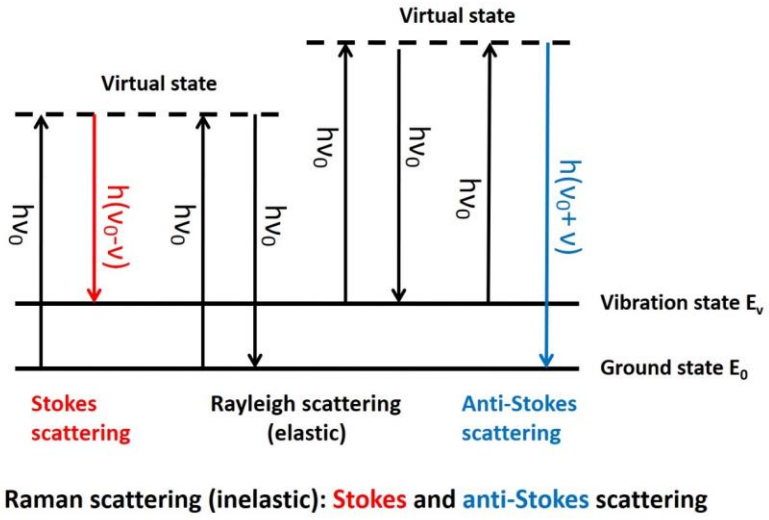

Figure 3.16: Raman scattering and Rayleigh scattering. They are both related to the energy transfer between ground states, vibration states, and virtual states of materials.

The first-order Raman spectrum of diamond consists of a single peak at 1333.1 cm^{-1} at room-temperature, shifting to 1333.3 cm^{-1} at 15 K [61]. This peak is referred to as the diamond vibron. The diamond vibron is found to shift monotonically to higher frequency under pressure. Hanfland and Syassen found that the high frequency edge of the diamond vibron blue shifts linearly with pressure to 30 GPa, which can be used as a manometer [62]. In this thesis research the following expression from Akahama and Kawamura [63] valid to 310 GPa gives the pressure as a function of the frequency shift $\Delta\upsilon$ of the Raman edge (see Figure 3.17):

$$P(GPa) \cong K_0 \frac{\Delta\upsilon}{\upsilon_0}\left[1 + \frac{1}{2}(K_0' - 1)\frac{\Delta\upsilon}{\upsilon_0}\right], \tag{3.3}$$

where υ_0 = 1334 cm^{-1}, K_0 = 547(11) GPa, and K_0' = 3.75(20).

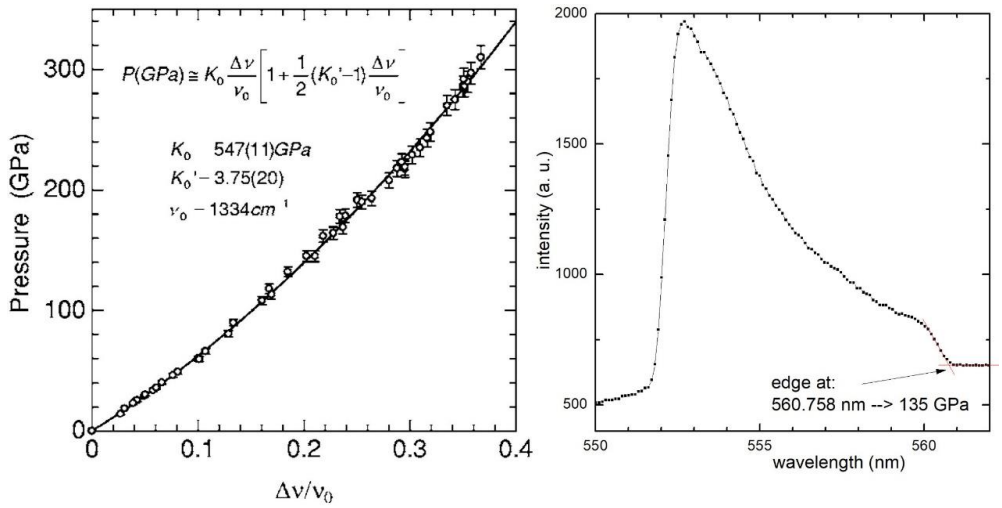

Figure 3.17: (left) Pressure versus relative shift in high-pressure edge frequency of the diamond vibron from Eq. 3.3 [63], and (right) example of pressure determination from the edge frequency.

Because of the broadening and weakening of the ruby R_1 line above one megabar, the diamond vibron gauge is preferred in this extreme pressure region.

We now outline several advantages the vibron manometer has compared with the ruby fluorescence manometer. In measurements to 100 - 200 GPa a beveled culet diameter of only 180 μm is normally used. This limits the sample size to approximately 40 - 50 μm and the ruby sphere to about 15 μm diameter. The intensity of the fluorescence from a ruby sphere of this size is near the detection limit of our in-cryostat optical system. In addition, such a ruby sphere can significantly influence the pressure distribution if it is placed on top of the sample. If the ruby sphere is placed next to the sample, the pressure on the ruby sphere can be quite different from the pressure on the sample. The diamond vibron manometer enables us to measure pressure anywhere from the center to the edge of the sample chamber, thus allowing an estimate of the pressure gradient across the sample. In optical absorption measurements the ruby fluorescence cannot be used as a pressure gauge since the incident light can also transmit through the ruby in the sample chamber, resulting in an artificial absorption spectrum.

Chapter 4

Experimental Results and Discussion

4.1 Enhanced Magnetic Ordering in Sm metal

The lanthanide (Ln) series of elements comprises the 15 metallic elements with atomic numbers 57 through 71, from lanthanum (La) through lutetium (Lu). These elements, along with the chemically similar elements scandium (Sc) and yttrium (Y), are often collectively known as the rare earth elements. Lanthanides are characterized by the gradual filling of their 4*f* orbitals, which gives rise to the magnetism in lanthanides. The poor shielding of the 5*s* and 5*p* orbitals by the 4*f* orbitals is also the cause of the famous lanthanide contraction, i.e. the reduction in size of the Ln^{3+} ion from La^{3+} (103 pm) to Lu^{3+} (86.1 pm).

A structural sequence from hcp → Sm-type → dhcp → fcc → dfcc in regular trivalent Ln metals under pressure or with decreasing atomic number is observed as seen in Figure 4.1. Note that the divalent Ln metals Eu and Yb, as well as the trivalent Ce metal, show different structural behavior. J. Duthie and D. Pettifor [65] showed that in Ln^{3+} metals either pressure or decreasing atomic number decreases the volume available to the conduction electrons outside the ion core, leading to the increasing occupancy of the *d*-band electrons that drives Ln metals through the above structural sequence. The origin of magnetism in lanthanide metals has been discussed in Subsection (2.1.2). Under sufficiently high pressures we have seen that the RKKY interaction is compromised by Kondo spin screening and will be discussed for the specific case of samarium (Sm) below.

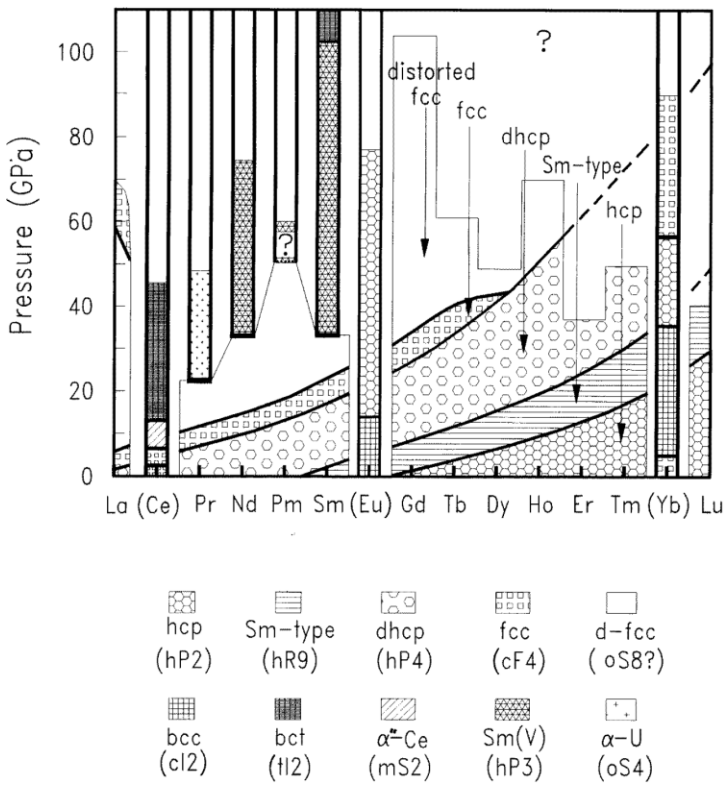

Figure 4.1: Generalized phase diagram for lanthanide metals and inter-lanthanide alloys under pressure at ambient temperature. The figure is taken from [64].

4.1.1 Previous Research

In recent studies on the trivalent lanthanide metals Nd [2], Gd [4], Tb [3], and Dy [4], the magnetic ordering temperature T_o was found, with the exception of Gd, to rise steeply to anomalously high values upon the application of sufficiently high pressures. In the same pressure range the superconducting pair breaking in dilute magnetic alloys of Nd, Tb, and Dy with superconducting Y took on extremely high values, in the case of Y(Nd) the record-high value 39 K/(at.% Nd) [2]. Such high values point to giant Kondo pair breaking, a sign that these lanthanides are approaching a magnetic instability. The anomalous rise in T_o would thus appear to be related to the unstable magnetic state. It is interesting to note that in the Kondo lattice model described by the Doniach phase diagram [14] T_o is expected to first increase with the

magnitude of the negative covalent mixing exchange coupling J_- [66] before passing through a maximum and falling rapidly to the quantum critical point at 0 K. This occurs when the RKKY interaction is totally suppressed by Kondo spin screening. Since the magnitude of J_- normally increases under pressure [67], in the Doniach picture T_o versus pressure should pass through a maximum and fall to 0 K. Such behavior was recently observed on elemental Nd metal by Song *et al*. [2]. Due to the extreme stability of Gd's magnetic state with its half-filled $4f^7$ configuration, even pressures to 1 or 2 Mbar are not sufficient to destabilize Gd, as evidenced by the absence of an anomalous rise in T_o (P) in Gd nor strong pair-breaking in Y(Gd) [68].

In view of the fact that some of the most anomalous magnetic behavior was found in trivalent Nd metal and Y(Nd) alloys at extreme pressure, an in-depth study of the second light trivalent lanthanide Sm^{3+}, both as elemental metal and in the dilute magnetic alloy Y(Sm), was attempted. Trivalent Sm assumes the electronic configuration [Xe]$4f^5$. Sm metal crystallizes in the Sm-type (α-Sm) structure at ambient pressure, transitioning to dhcp at 4 GPa, to fcc at 14 GPa, to distorted fcc (dfcc) at 19 GPa, to *hP*3 at 37 GPa, and finally to *tI*2 at 91 GPa [69, 70]. These structural transitions thus follow the regular trivalent lanthanide structure sequence under pressure: hcp → Sm-type → dhcp → fcc → dfcc, a sequence related to the increasing *d* character in the conduction band upon compression [65].

The free Sm^{3+} ion has the ground state configuration $^6H_{5/2}$, with Landé g-factor $g_J = 2/7$ and total angular momentum $J_t = 5/2$. The effective magnetic moment of free Sm^{3+} calculated from Hund's rules is $p_{eff} = 0.85\ \mu_B$. However, magnetic susceptibility measurements on paramagnetic Sm salts give $p_{eff} = 1.74\ \mu_B$ [71]. The discrepancy between the theoretical and experimental values is believed due to contributions from low-lying excited states with different J_t values.

In Sm metal the situation is even more complicated since the crystalline electric field and conduction electron polarization significantly influence the magnetic state of Sm^{3+} [72]. As a result of this complexity, Sm metal exhibits a number of interesting physical phenomena. Both the temperature-dependent heat capacity [73] and electrical resistivity [74] have anomalies near both 13 K and 106 K, as seen in Figure 4.2. The fact that the temperature-dependent magnetic susceptibility of Sm has peaks near these temperatures, as shown in Figure 4.3 (left), strongly suggests antiferromagnetic ordering [75]. This was confirmed by Koehler and Moon from neutron diffraction experiments on single-crystalline ^{154}Sm [76]. They viewed Sm-type Sm (space group R-3m) as a combination of hexagonal and cubic sites where Sm^{3+} ions at these sites magnetically order at 106 K and 14 K, respectively. Figure 4.3 (right) presents the magnetic structure of Sm metal at ambient pressure.

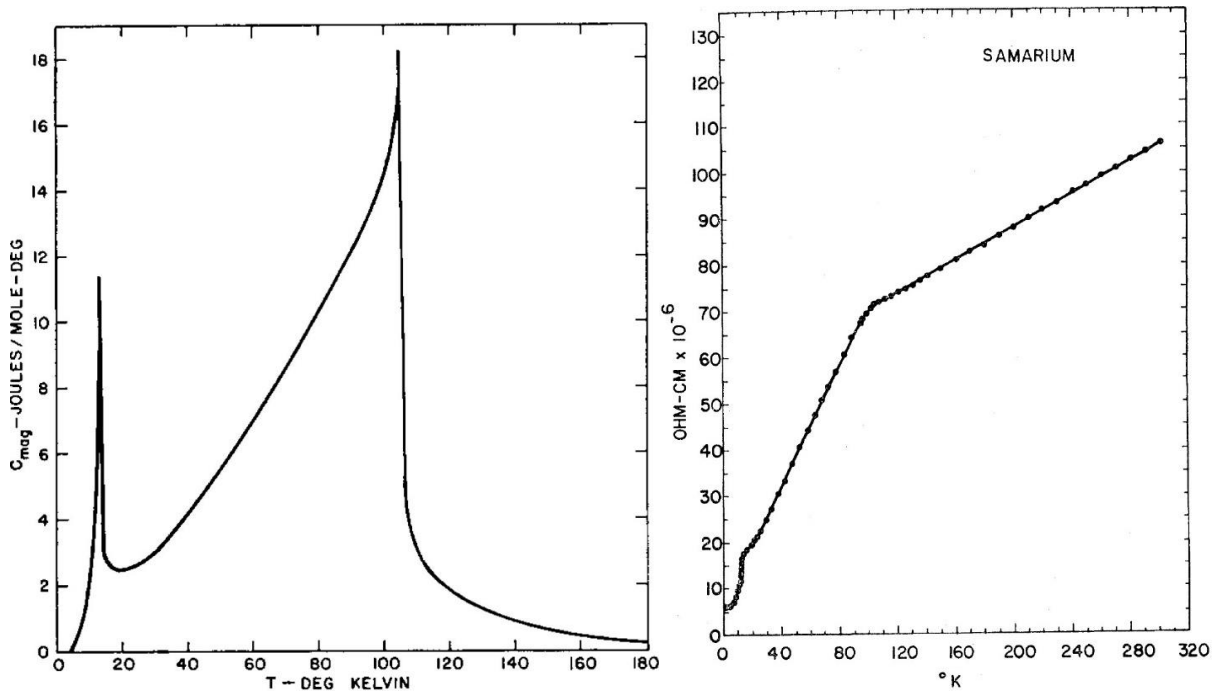

Figure 4.2: The magnetic heat capacity (left, taken from [73]) and temperature-dependent resistivity (right, taken from [74]) of Sm.

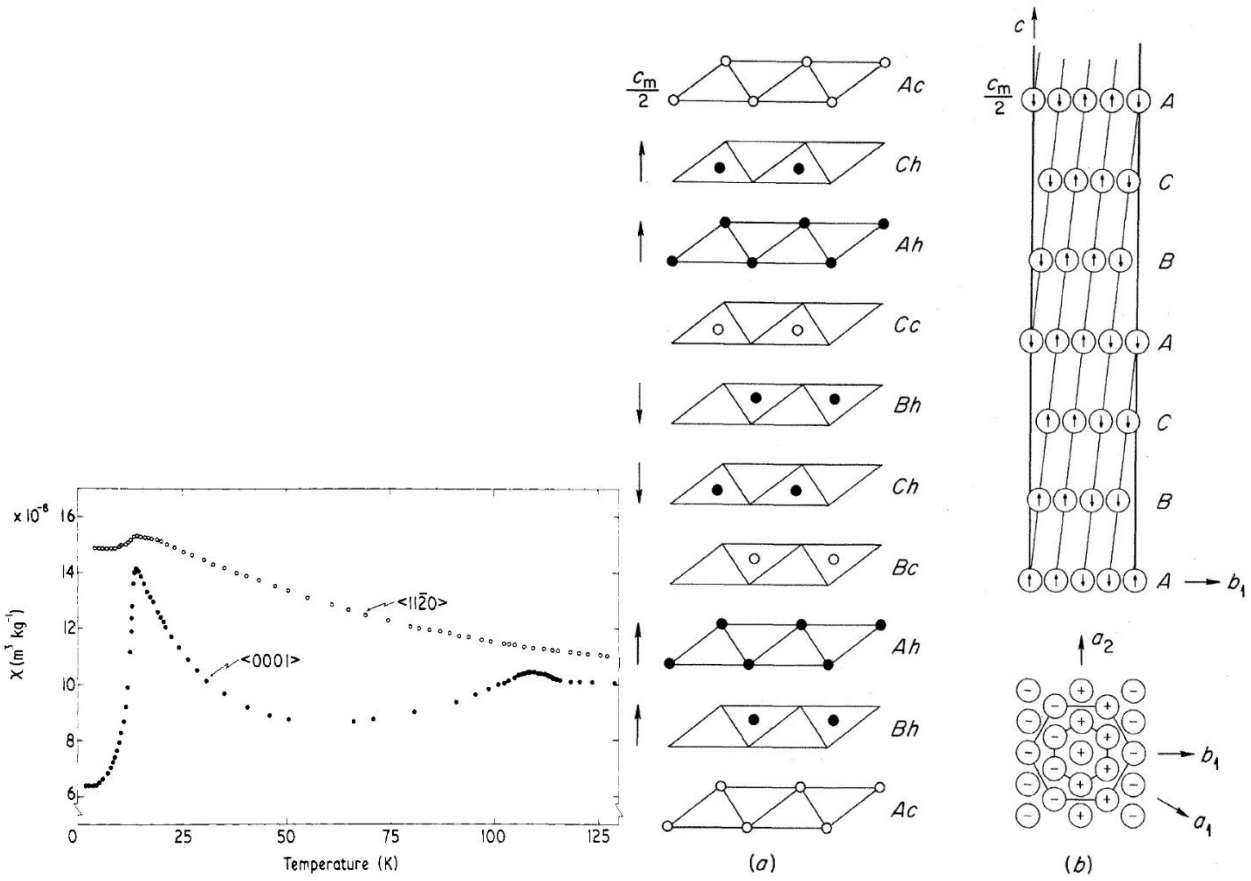

Figure 4.3: (left) The temperature-dependence of the mass susceptibility in the basal plane and *c*-axis (from Ref [75]), and (right) the magnetic structure of Sm measured by neutron diffraction (from Ref [76]). Sm can be viewed as a nine-layer stacking sequence, ACACBCBAB…, of close-packed hexagonal layers. Two thirds of atoms are at hexagonal sites (h) and one third of atoms are at cubic sites (c).

In temperature-dependent resistivity measurements $R(T)$ a knee is observed at the magnetic ordering temperature T_o due to the loss of spin-disorder scattering upon cooling. Dong *et al*. [77] measured resistivity on Sm to 43 GPa shown in Figure 4.4 (left) and found that the two ordering temperatures move toward each other with increasing pressure, finally merging together near 66 K at 8 GPa where Sm enters the dhcp phase. At higher pressures T_o increases rapidly to 135 K at 43 GPa. Johnson *et al*. [78] measured $R(T)$ on Sm to 47 GPa and made the phase diagram shown in Figure 4.4 (right). They found that the two ordering temperatures merge near 56 K at 10 GPa

and increase slowly up to the phase transition at 34 GPa (dfcc → *hP*3) where again two ordering temperatures appear.

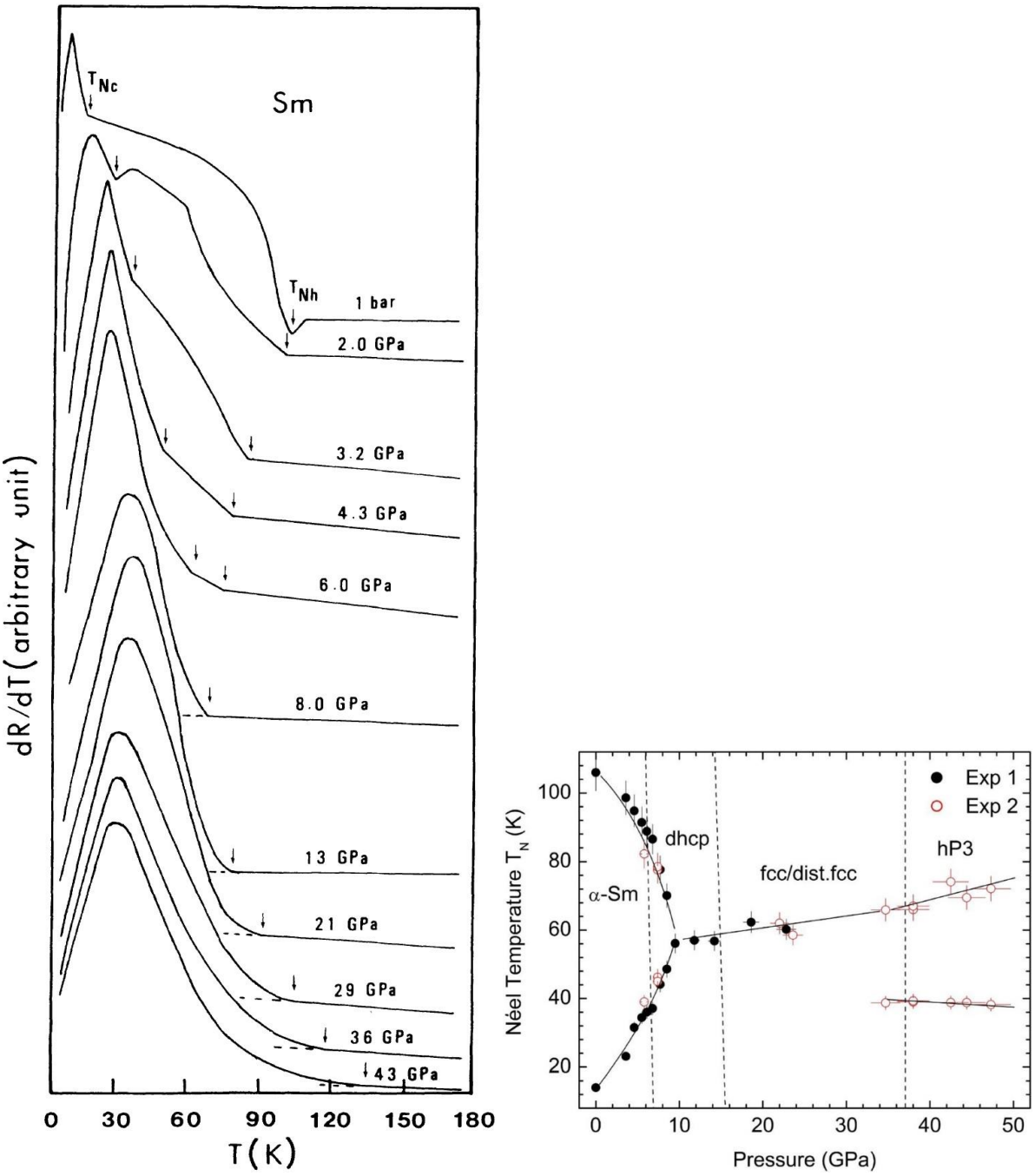

Figure 4.4: (left) The temperature dependence of d*R*/d*T* of Sm at different pressures (figure taken from Ref [77]). The arrows pointing down mark the antiferromagnetic transition temperatures T_N, and (right) the magnetic phase diagram showing the variation of T_N as a function of pressure to 47 GPa (figure taken from Ref [78]).

4.1.2 Present Experiments

The polycrystalline Sm samples for the high-pressure resistivity measurements were cut from a Sm ingot (99.9 % pure, Ames Laboratory [79]). The dilute magnetic Y(Sm) alloys were made by argon arc-melting small amounts of Sm with Y (99.9 % pure, Ames Laboratory [79]). To enhance homogeneity the alloys were sealed in glass ampules under vacuum and annealed at 600^{o}C for two weeks. The concentrations of Sm for the four alloys as determined from x-ray fluorescence analysis is: 0.15(2) at.%, 0.40(3) at.%, 0.83(4) at.%, and 1.16(6) at.%. Before arc-melting the nominal concentrations were 0.5 at.%, 1.0 at.%, 1.2 at.%, and 2 at.%, respectively. It follows that 30% to 70% Sm evaporated during arc-melting due to the relatively low boiling point of Sm.

A diamond anvil cell (DAC) made of CuBe [80] was used to reach pressures to 150 GPa between two opposed diamond anvils (1/6-carat, type Ia) with 0.18 mm diameter culets beveled at 7 degrees to 0.35 mm. The force applied to the anvils was generated by a stainless-steel diaphragm filled with He gas [81]. In one experiment on Sm culets with 0.30 mm diameter without bevel were employed. In experiments with 0.18 mm culets the Re gasket (250 μm thick) was pre-indented to 30 μm and a 90 μm diameter hole drilled through the center of the pre-indentation area. A cBN-epoxy insulation layer was compressed onto the surface of the gasket. Four Pt strips (4 μm thick) were then placed on the insulation layer, acting as the electrical leads for the 4-point resistivity measurement. The Sm or Y(Sm) sample with dimensions 40 * 40 * 4 μm^3 was then placed on the Pt strips.

The DAC was inserted in an Oxford flow cryostat capable of varying temperature from ambient to 1.3 K. Pressure was determined at room-temperature using the diamond vibron [63]. Earlier resistivity experiments by Song *et al.* [2] in an identical DAC using a ruby manometer revealed

an approximately linear pressure increase of ~ 30% on cooling from 295 to 4 K. In the present experiments, this calibration allows an estimate of the pressure at the magnetic or superconducting transition temperatures from the vibron pressure at ambient temperature. After the sample warmed back to room-temperature, a pressure about several GPa's was gained compared to the pressure before cooling.

The four-point resistance $R(T)$ was measured in three runs over the temperature and pressure ranges 1.3 to 295 K and 2 to 127 GPa, respectively. Figure 4.5 shows $R(T)$ during warming at different pressures in runs 1 and 3. In most experiments the Sm sample was cooled to ~ 4 K; however, the Sm sample was cooled down to 1.3 K at pressures 2, 9, 25, 51, 60, 86, 93, 97, and 127 GPa but no superconductivity was found. As seen in Figure 4.5, at high temperatures the resistance of the sample decreases roughly linearly when T goes down, reflecting the R-T law of resistance from electron-phonon scattering. However, at low temperature a knee or kink appears in $R(T)$, suggesting a reduction of spin-disorder scattering R_{sd} when Sm enters a magnetic ordering state. This transition is not very clear above 40 GPa since the pressure gradient in a nonhydrostatic pressure experiment gets gradually bigger with increasing pressure.

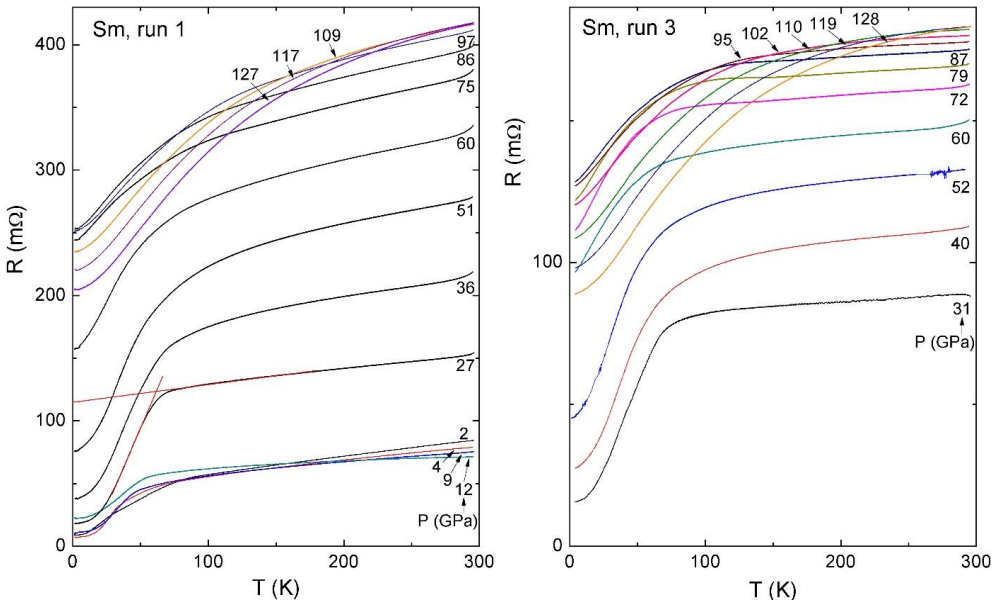

Figure 4.5: Four-point resistance data $R(T)$ from run 1 (left) and run 3 (right) for Sm metal versus temperature on warming from 1.3 to 295 K at multiple pressures to 128 GPa (measured at room-temperature). A kink or knee in $R(T)$ at T_o signals the onset of magnetic order (for example, in run 1 at 27 GPa $T_o \approx 61$ K). Straight red line fitting data above knee for 27 GPa intercepts resistance axis at 115 mΩ.

Three different methods were used to determine the pressure-dependent magnetic ordering temperature in Sm: method 1 (intersection): define T_o as the intersection point of two straight lines which go through the $R(T)$ below T_o and above T_o respectively; method 2 (dRdT #1): define T_o as the point where dR/dT increases rapidly; method 3 (dRdT #2): half way down the slope where dR/dT increases sharply. Figure 4.6 gives examples of three methods to determine T_o. Finally, the method 1 was chosen to be consistent with previous work on Nd, Gd and Dy. In Figure 4.7 the values of T_o for Sm from runs 1 and 3 are plotted versus pressure and compared to previous results from Dong *et al*. [77] to 43 GPa and Johnson *et al*. [78] to 47 GPa. In all experiments the two branches of T_o are seen to merge near 13 GPa followed by an increase in T_o. In the present experiments $T_o(P)$ passes through a maximum near 53 GPa, gradually decreasing to ~ 60 K near 85 GPa, before rising sharply to ~ 140 K at 150 GPa. The report by Johnson *et al.* [78] that a second transition appears in the pressure range 35 - 50 GPa could not be confirmed.

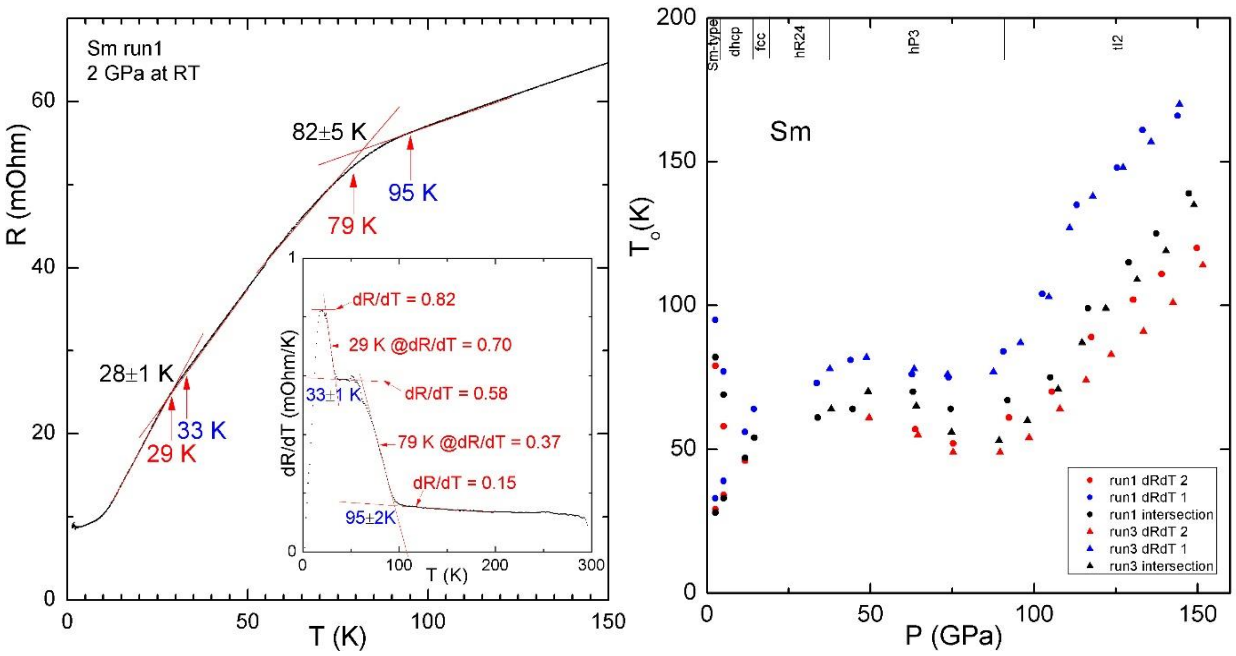

Figure 4.6: Three different ways to determine T_o for $R(T)$ at 2 GPa (left) and $T_o(P)$ based on the three methods (right). T_o determined with method 1 is in black; T_o determined with method 2 is in blue; T_o determined with method 3 is in red. Note that the fundamental trend in $T_o(P)$ is the same for all three methods.

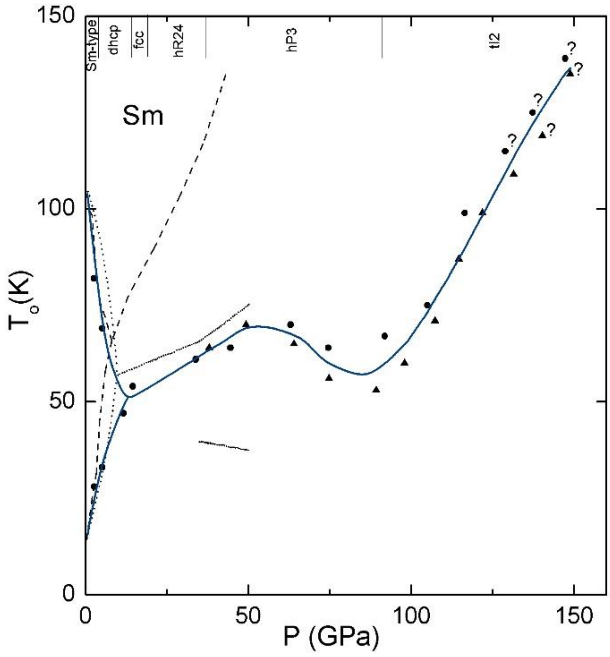

Figure 4.7: Magnetic ordering temperature T_o of Sm versus pressure. Data from run 1 (solid circle), data from run 3 (solid up triangle), dotted line from Ref [78], dashed line from Ref [77]. Value of pressure is estimated for temperature near T_o (see text). Question marks (?) accompany data points where evidence for magnetic ordering is weak. Extended solid lines through data points are guides to the eye. Crystal structures for Sm at top of graph determined to 189 GPa [70].

Independent information on the origin of the resistivity knee in Sm can be gained by comparing the pressure dependence of the spin-disorder resistance $R_{sd}(P)$ for $T > T_o$ to that of $T_o(P)$ obtained from the resistivity knee. As discussed in Ref [4], both T_o [1] and R_{sd} [82] are proportional to $J^2N(E_F)$, where J is the exchange interaction between local moment and conduction electrons and $N(E_F)$ is the density of states at the Fermi energy. A similarity between the pressure dependences $T_o(P)$ and $R_{sd}(P)$ is anticipated for the trivalent lanthanide metals since their *spd* conduction electron properties are closely related. This similarity was indeed observed for Nd [2], Gd [4], Tb [3], and Dy [4]; it would be interesting to examine whether this also holds for Sm, together with Nd the second light lanthanide studied. From Figure 4.5 it is readily seen that where the resistivity knee shifts under pressure to higher temperatures the size of the resistivity drop-off below the knee also increases. A semiquantitative estimate of R_{sd} is now attempted.

The total measured resistance is the sum of three terms, $R(T) = R_d + R_{ph}(T) + R_{sd}(T)$, where $R_d = R(0\ K)$ is the temperature-independent defect contribution. In the paramagnetic state in the temperature region above the resistance knee, $R_{sd}(T)$ is constant, taking on its maximum value R_{sd}^{max}, so that the only temperature dependence comes from the phonon resistance $R_{ph}(T)$. To estimate R_{sd}^{max} Colvin *et al*. [83] assumed that $R_{ph}(T)$ depends linearly on temperature, and extended a straight line fit to $R(T)$ for $T > T_o$ to 0 K with intercept R_{int} and then subtracted off R_d from this intercept. An example for this estimate is given in Figure 4.5 at 27 GPa where $R_{sd}^{max} = [R_{int} - R_d] = (115 - 18)\ m\Omega = 97\ m\Omega$. In Figure 4.8 R_{sd}^{max} is plotted as a function of pressure. Comparing Figures 4.7 and 4.8, a parallel behavior of the pressure dependences $T_o(P)$ and $R_{sd}^{max}(P)$ is indeed observed, thus supporting the identification of the resistance knee with the onset of magnetic ordering in Sm. Also included in Figure 4.8 is the quantity $[R(290\ K) - R(4\ K)]$ that is seen to also qualitatively track T_o versus pressure. This suggests that the resistance from

electron-phonon scattering at room-temperature does not change dramatically within the pressure range of these experiments.

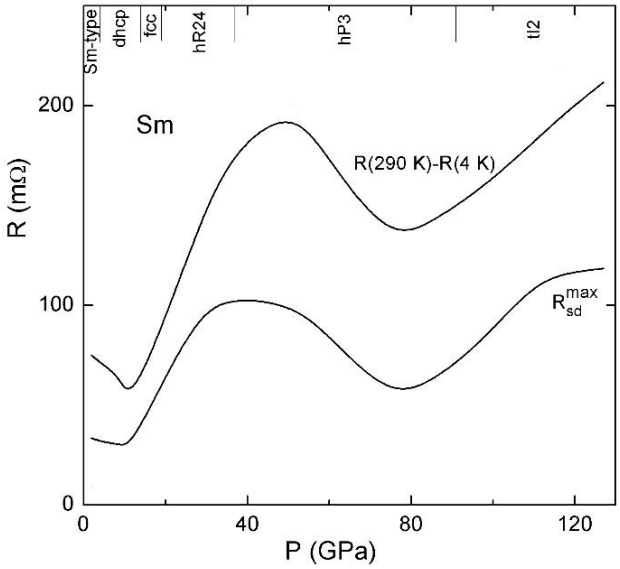

Figure 4.8: Plot of estimated maximum value of spin-disorder resistance R_{sd}^{max} (P) versus pressure. R_{sd}^{max} is estimated by subtracting defect resistance R_d from intersection point R_{int} on resistance axis of straight-line fit to $R(T)$ data for $T > T_o$ (see text). Also shown is pressure dependence of [R(290 K) - R(4 K)] using data from Figure 4.5 (left).

To examine whether the rapid rise in T_o for pressures above 85 GPa might be related to an approaching instability in Sm's magnetic state, Sm is alloyed in dilute concentration with Y, a high-pressure superconductor having, compared to the trivalent lanthanides, closely similar conduction electron properties and structural sequence under pressure [8]. Under these circumstances the ability of the Sm ion to suppress Y's superconductivity, the degree of pair breaking $\Delta T_c \equiv T_c$ [Y] - T_c [Y(Sm)], can reveal valuable information about the magnetic state of the Sm ion itself. This general observation was emphasized for lanthanide ions by Maple [84]. In the present experiment Y(Sm) alloys with differing dilute Sm concentrations were studied at pressures to 180 GPa. Figure 4.9 shows the superconducting transitions in four-point resistance measurements on Y(0.15 at.% Sm) at selected pressures. As illustrated in this figure for the $R(T)$

data at 52 GPa, T_c is defined as the temperature at which the resistance transition reaches the halfway mark, whereas the intersection point of two straight red lines defines T_c^{onset}, and T_c^{zero} gives the temperature where the resistance disappears. The fact that a typical total transition width is less than 2 K gives evidence that the distribution of Sm ions in the alloys is homogeneous. As seen from the data in Figure 4.9, T_c increases monotonically with pressure to 140 GPa, but then decreases to 180 GPa.

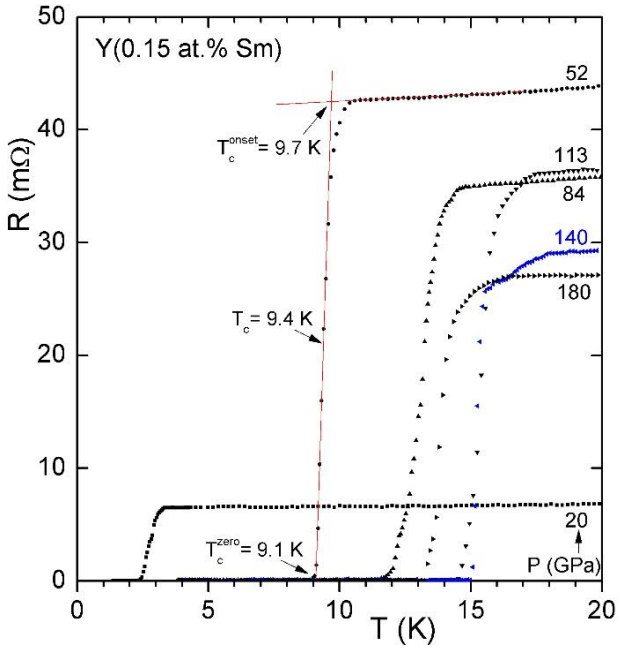

Figure 4.9: Four-point resistance of Y(0.15 at.% Sm) alloy versus temperature showing superconducting transition at various pressures to 180 GPa (estimated at low temperature). Intersection of two red straight lines defines T_c^{onset}; midpoint of transition defines T_c; temperature where $R(T) = 0$ defines T_c^{zero}.

The dependence of T_c on pressure for Y(Sm) alloys with Sm concentrations 0.15, 0.40, 0.83, and 1.16 at.% is shown in Figure 4.10. Below ~ 40 GPa the $T_c(P)$ dependence for all four alloys tracks that for pure Y. However, above ~ 40 GPa a strong suppression sets in. This suppression ΔT_c is so strong that for Y(1.16 at.% Sm) at pressures above 50 GPa T_c lies below the temperature range of this experiment (1.3 K). For the more dilute Y(0.15 at.% Sm) and Y(0.40 at.% Sm) alloys, T_c remains well above 1.3 K at all pressures.

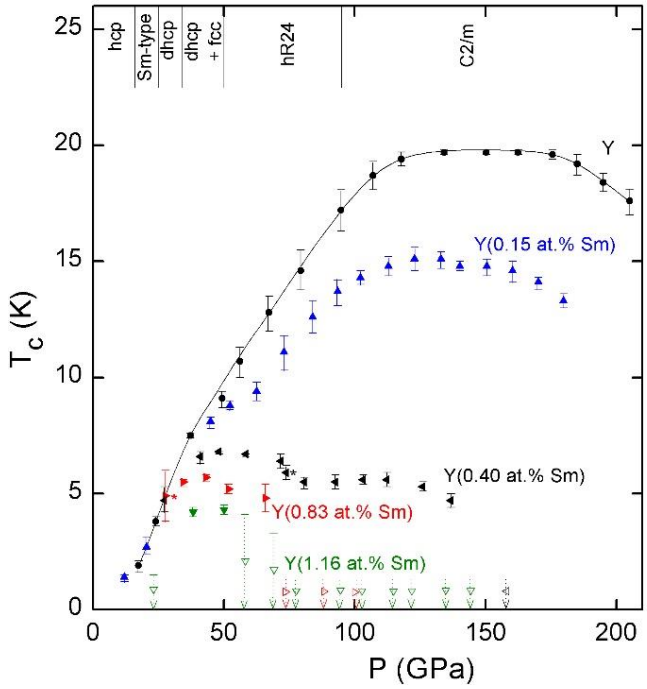

Figure 4.10: Superconducting transition temperature T_c versus pressure (estimated at low temperature) for Y and Y(Sm) alloys at four different Sm concentrations. In all cases giant superconducting pair breaking $\Delta T_c \equiv T_c$ [Y] - T_c [Y(Sm)] is observed. At top of graph are crystal structures for superconducting host Y to 177 GPa [85].

To allow a more meaningful comparison of the degree of superconducting pair breaking ΔT_c for the different alloys, in Figure 4.11 ΔT_c is divided by the Sm concentration c and then plotted versus pressure for all alloys measured. Where they can be compared, the individual $\Delta T_c/c$ curves agree reasonably well and increase monotonically with pressure, reaching the extremely high value of ~ 40 K/at.% Sm at 180 GPa, a value slightly higher than that found earlier for Y(0.4 at.% Nd) [2]. Both the giant pair breaking in Y(Sm) and the remarkable increase of T_o in Sm give evidence for unconventional physics in Sm above 85 GPa.

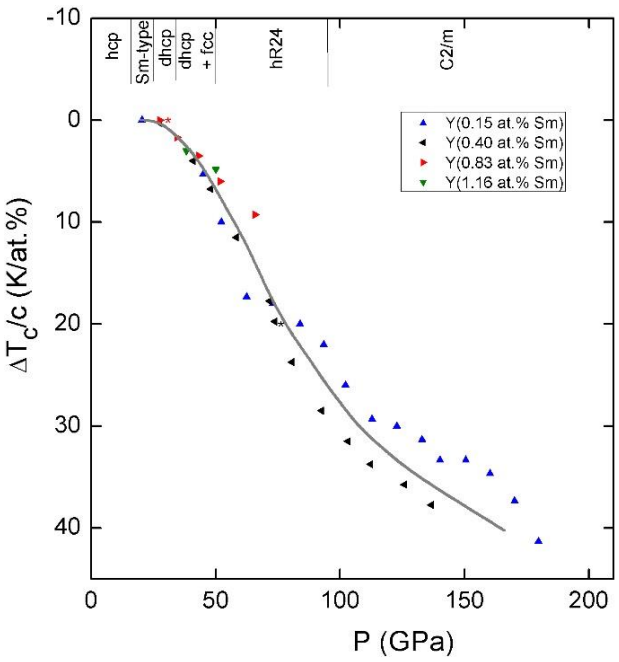

Figure 4.11: Superconducting pair breaking ΔT_c divided by concentration c of Sm in four Y(Sm) alloys plotted versus pressure. At top of graph are crystal structures for superconducting host Y to 177 GPa [85]. Line through data is guide to the eye.

4.1.3 Discussion

The present results on Sm and Y(Sm) alloys will now be compared to those from earlier studies on the lanthanides Nd [2], Gd [4], Tb [3], and Dy [4]. Going from right to left across the lanthanide series (Lu to La) or by applying pressure, one finds with few exceptions [85] the canonical rare-earth crystal structure sequence hcp → Sm-type → dhcp → fcc → *hR*24 believed to mainly arise from an increase in the number n_d of *d*-electrons in the conduction band [65].

In the elemental lanthanide metals magnetic ordering arises from the indirect RKKY exchange interaction between the magnetic ions. For a conventional lanthanide metal with a stable magnetic moment, the magnetic ordering temperature T_o is expected to scale with the de Gennes factor $(g - 1)^2 J_t(J_t + 1)$, modulated by the prefactor $J^2N(E_F)$, where J is the exchange interaction

between the 4*f* ion and the conduction electrons, $N(E_F)$ the density of states at the Fermi energy, *g* the Landé g factor, and J_t the total angular momentum quantum number [1] (see Eq. 2.19).

In Figure 4.12 (a) the dependence of the magnetic ordering temperature T_o on pressure is shown for the four lanthanide metals Nd, Sm, Tb, and Dy. Except for Nd, $T_o(P)$ is seen to initially decrease rapidly with pressure, but then pass through a minimum and rise. $T_o(P)$ for Gd [4] also shows this same initial behavior. Since the de Gennes factor, in the absence of a magnetic instability or valence transition, is constant under pressure, the initial $T_o(P)$ dependence for the above lanthanides likely originates in the pressure dependence of the prefactor $J^2N(E_F)$. Electronic structure calculations for Dy support this conclusion [86, 87].

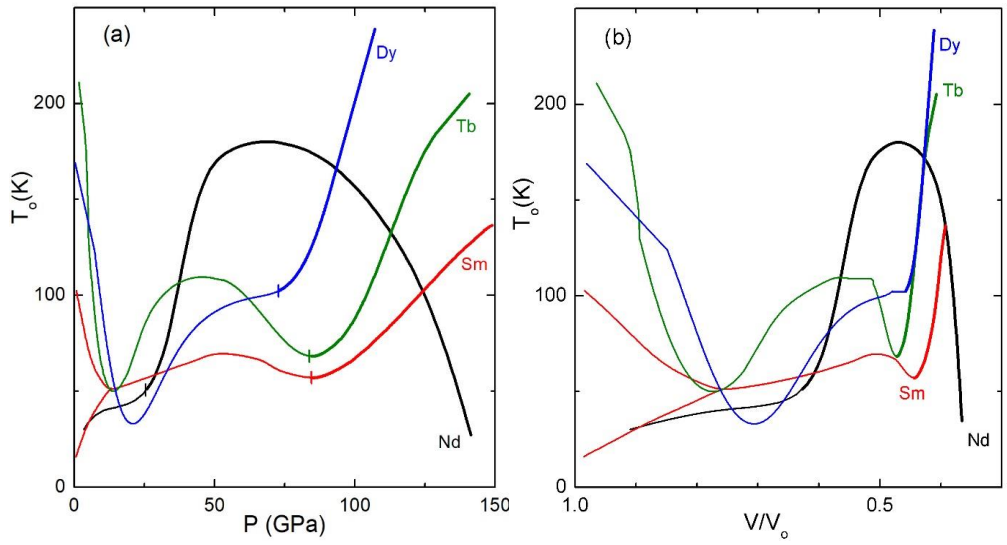

Figure 4.12: T_o under pressure for Nd, Sm, Tb, and Dy. (a) Graph comparing lines through T_o versus pressure data for Nd, Sm, Tb, and Dy. Vertical tick marks separate regions of "conventional" (to left) from "unconventional" (to right) behavior in $T_o(P)$; (b) Data in (a) is replotted versus V/V_o, where V_o is sample volume at ambient pressure, using measured equations of state of Nd [88], Sm [69], Tb [89], and Dy [90]. In both graphs, lines with double thickness mark regions where the magnetic ordering is "unconventional".

The strong initial decrease in T_o with pressure in Sm (upper transition), Gd, Tb, and Dy occurs within the hcp and Sm-type phases. The minimum in $T_o(P)$ at approximately 20 GPa for Dy

appears at somewhat lower pressures for Tb, Gd, and Sm, disappearing entirely for Nd. As discussed in some detail in Ref [2], this is consistent with an increase in the number of *d* electrons in the conduction band going from Dy to Nd; the electronic structure and the crystal structures taken on by Nd resemble those of Dy but at a pressure approximately 30 - 40 GPa higher [2]. The systematic behavior for all five lanthanides Dy, Tb, Gd, Sm, and Nd in the region of pressure where the hcp, Sm-type, dhcp, and *hR*24 structures occur, gives evidence that changes in the magnetic ordering temperature in this region are mainly determined by corresponding changes in the properties of the conduction electrons that mediate the RKKY interactions between the magnetic lanthanide ions.

It would seem helpful to propose that the $T_o(P)$ curves for each element can be separated into two principal pressure regions: a "conventional" region at lower pressure governed by the electronic properties of the conduction electrons and normal positive exchange interactions J_+ between the lanthanide ion and the conduction electrons, and an "unconventional" region at higher pressures where exotic physics dominates leading to negative covalent-mixing exchange J_- and associated anomalous magnetic properties. In the "conventional" region the observed variations in $T_o(P)$ would be principally caused by changes in the prefactor $N(E_F)J_+^2$ with pressure. In the "unconventional" pressure region highly correlated electron effects dominate leading to anomalous magnetic properties, including anomalous $T_o(P)$ dependences and giant superconducting pair breaking in dilute magnetic alloys.

Although the properties of the conduction electrons and the magnetic state of the lanthanide ions are intertwined, the "conventional" and "unconventional" regions represent different physics, the former being amenable through standard electronic structure calculations, whereas the latter is only accessible through consideration of strong highly correlated electron effects. The stability of

the ion's magnetic state is determined to a large extent by the exchange interactions within a given lanthanide ion (Hund's rules). Once the "unconventional" rapid rise in T_o with pressure sets in, it overpowers the "conventional" conduction electron behavior and determines $T_o(P)$. Since in Dy and Nd the "unconventional" region begins at a lower pressure, the rapid rise in T_o may prevent the "conventional" second minimum seen in Sm and Tb from appearing in $T_o(P)$ for Dy or Nd.

A rough estimate of the boundary pressure where the "unconventional" $T_o(P)$ behavior may begin for a given lanthanide is indicated by a vertical tick mark in Figure 4.12 (a). In the "unconventional" region itself the $T_o(P)$ data curves have been given double thickness. There is a good deal of arbitrariness for where this boundary is placed, particularly for Sm and Tb where the second $T_o(P)$ minimum may well belong to the "unconventional" region, instead of the "conventional" region, as indicated by the beginning of anomalous superconducting pair breaking in Y(Sm) or Y(Tb) near the pressure for the second minimum in $T_o(P)$.

Focusing now on the anomalous rise in T_o with pressure in the "unconventional" region in Figure 4.12 (a), we note that this rise is steepest for Nd but becomes progressively less steep for Dy, Tb, and Sm. At least part of this reduction in steepness has to do with the fact that the compressibility of the lanthanides decreases significantly as pressure is increased. To bring out the physics more clearly, T_o in Figure 4.12 (b) is replotted versus the relative volume V/V_o. Different features in the respective curves are shifted to new relative positions, but now it is seen that the sharp upturns in $T_o(P)$ have nearly the same slope and are much steeper relative to the changes in the "conventional" region at lower pressures. This points to a common mechanism for the upturn in these four lanthanides.

In Figure 4.13 the normalized pair breaking curve $\Delta T_c/c$ for Y(Sm) from Figure 4.11 is compared to those for the dilute magnetic alloys Y(Nd) [2], Y(Tb) [3], and Y(Dy) [4]. For Y(Sm) and Y(Nd) the pair breaking begins to increase rapidly at relatively low pressures compared to Y(Tb) and especially Y(Dy). At least part of the reason for this is that the Y host exerts lattice pressure on the light lanthanides Sm and Nd, but not on Tb and Dy. This can be seen by comparing the respective molar volumes in units of cm^3/mol: Y(19.88), Nd(20.58), Sm(19.98), Gd(19.90), Tb(19.30), Dy(19.01) [91]. Without exception, the region of pressure where $T_o(P)$ increases rapidly lies within the region of pressure where the superconducting pair breaking $\Delta T_c/c$ in the corresponding dilute magnetic alloy with Y is anomalously large. Note also that the maximum value of the slope of $\Delta T_c/c$ versus pressure in Figure 4.13 is noticeably reduced for Y(Dy). At least part of this effect is due to the sizable reduction in the compressibility of Y at higher pressures.

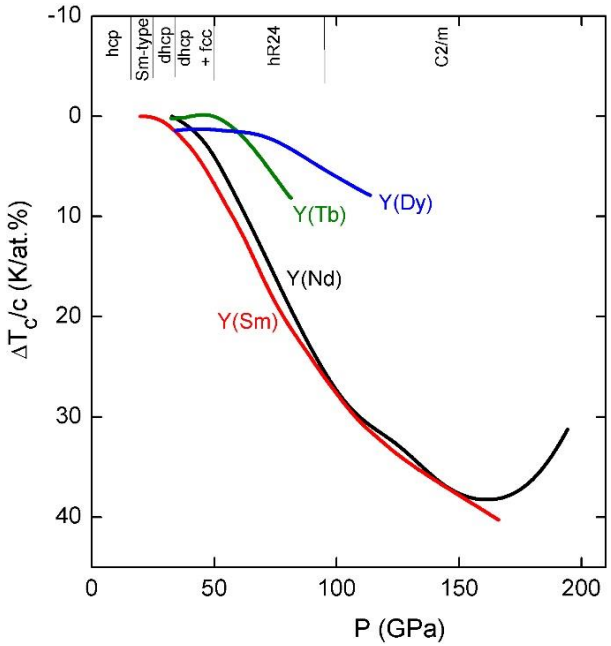

Figure 4.13: Graph comparing relative superconducting pair breaking $\Delta T_c/c$ for dilute magnetic alloys Y(Nd), Y(Sm), Y(Tb), and Y(Dy) versus pressure. The figure shows lines through data as in Figure 4.11 for Y(Sm). At top of graph are crystal structures for superconducting host Y to 177 GPa [85].

For the dilute magnetic alloy Y(Nd) the normalized pair breaking data in Figure 4.13 are seen to be reduced ($\Delta T_c/c$ turns upwards) for pressures above 160 GPa. Presumably the same effect would also be observed in Y(Sm), Y(Tb), and Y(Dy) if the experiments were extended to even higher pressures. This reduction in giant pair breaking seen in Y(Nd) at the highest pressures was observed previously in dilute magnetic alloys La(Ce) [36], La(Pr) [92], and Y(Pr) [68, 93] and can be readily accounted for in terms of Kondo pair-breaking theory [38] where the magnitude of the negative exchange interaction J_- between the magnetic ions and the conduction electrons increases with pressure. The appearance of such Kondo physics in the dilute magnetic alloy suggests that the corresponding concentrated system will likely show Kondo lattice, heavy Fermion, and fluctuating valence behavior at higher pressures, eventually culminating in a full increase in valence whereby one 4*f* electron completely leaves its orbital and joins the conduction band.

The well-known Doniach model [14] is often cited to account for the dependence of the magnetic ordering temperature T_o in a Kondo lattice as a function of the magnitude of the negative exchange parameter J_- (see Figure 2.3 in Chapter 2). Whereas the upturn in $\Delta T_c/c$ occurs above 160 GPa for Y(Nd), the downturn in $T_o(P)$ begins above 80 GPa (see Figure 4.12 (a)) for Nd in its "unconventional" pressure region (double line width). The rapid rise in $T_o(P)$ for Nd followed by its rapid downturn resembles the dependence anticipated from the Doniach model [2]. A similar $T_o(P)$ dependence would be expected for Sm, Tb and Dy if the experiments were extended to even higher pressures.

The values of the pair-breaking parameter $\Delta T_c/c$ for Nd and Sm impurities in Y are surprisingly large - in fact, to our knowledge, the largest ever reported. However, even more surprising is the sharp upturn in $T_o(P)$ where T_o reaches values that appear to be much higher than would have

been possible had “unconventional” physics, such as Kondo physics, not been operative. In the case of Dy, $T_o(P)$ extrapolates to values well above room-temperature, higher than any known value for an elemental lanthanide metal at either ambient or high pressure [4].

4.2 Search for Superconductivity in Cs and Rb

The alkali elements occupy the first column in the periodic table that consists of lithium (Li), sodium (Na), potassium (K), rubidium (Rb), cesium (Cs), and francium (Fr, very rare due to its extremely high radioactivity). Their single valence electron resides in an *s* orbital. These outermost electrons are only weakly bound, forming an *s*-band in alkali metals, and are responsible for their highly chemically active nature. At ambient pressure and temperature, all alkali metals take on the bcc structure. They are driven first into the fcc structure by the application of pressure, then into more complex, lower symmetry structures at higher pressures. Figure 4.14 shows the structural sequences of alkali metals at room-temperature. The driving force of the phase transitions in alkali metals is still under debate. The interaction between the Fermi surface and Brillouin zone boundary, based on a nearly-free-electron picture, has been proposed to explain the universal bcc to fcc transition, but it cannot account for the transition in Na since there is no electronic structural change to very high pressure (120 GPa) [94]. The following structures with lower symmetry are thought to be the result of pressure induced *s-p* electron transfer in the light alkalis Li and Na [95] or *s-d* electron transfer in the heavy alkalis K, Rb, and Cs [96, 97].

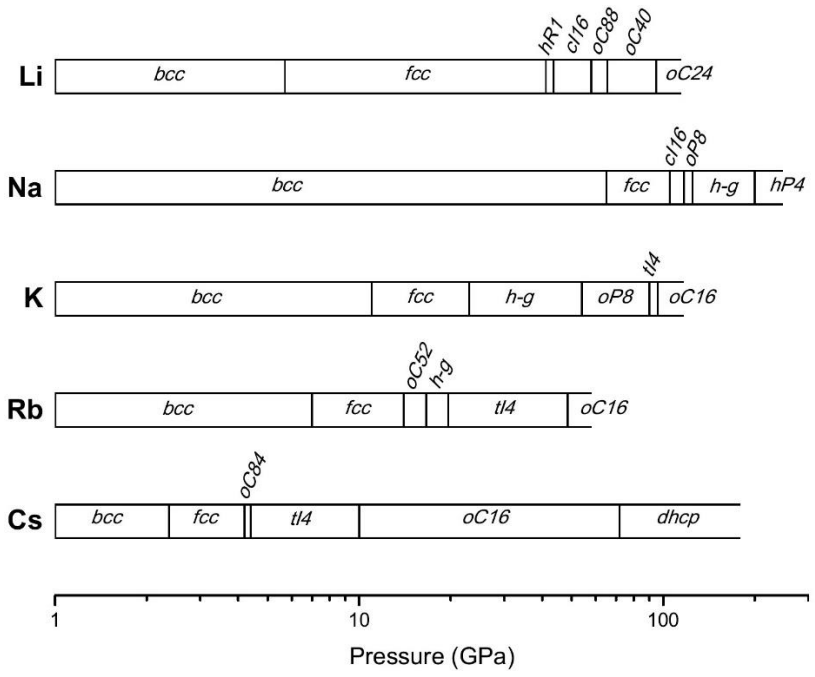

Figure 4.14: Phase diagram of alkali metals. Structures are determined at room-temperature, except for Li which is for ~ 200 K. The figure is taken from [39].

Since alkali metals are generally viewed as the metals most closely obeying the nearly-free-electron model, they are not expected to show superconductivity at ambient pressure (refer to Subsection 2.2.2). Only Li has been found to be superconducting at ambient pressure, but only at the very low temperature of 0.4 mK [6]. However, its superconducting transition temperature increases dramatically to above 5 K in the pressure range 20 to 60 GPa, peaking at 14 K at 30 GPa [7]. There are no reports of superconductivity in the other alkalis at ambient pressure. Pressure-induced superconductivity in Cs will be discussed in the following sections.

4.2.1 Previous Research

At ambient pressure the properties of the alkali metals, including Cs and Rb, can be well explained by the nearly-free-electron model. For example, MacDonald *et al*. [98] found the electrical (thermal) resistivity from lattice vibrations in Cs and Rb to be proportional to T^5 (T^2) at

low temperatures less than 1/10 of their Debye temperatures, as expected for nearly-free-electron metals. However, since Cs and Rb are among the most compressible elements (see Figure 4.15), they experience dramatic structural and electronic changes under high pressures whereby they completely lose their free-electron character.

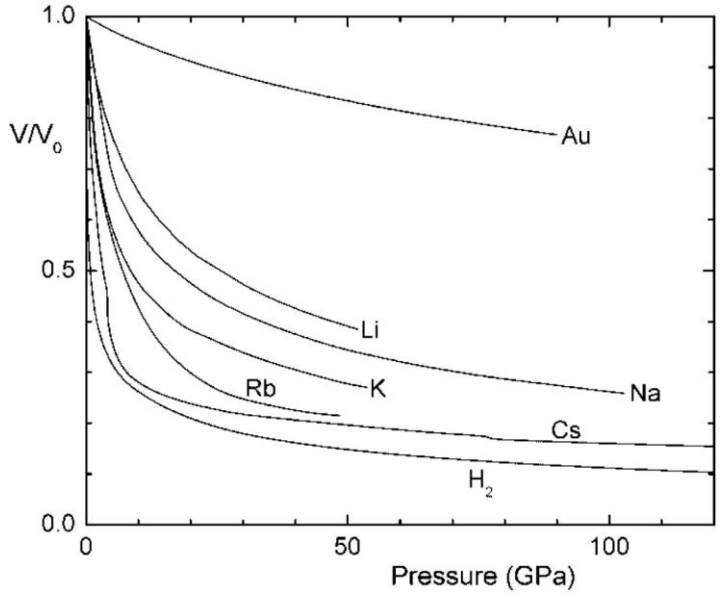

Figure 4.15: Equations of state of several elements. All data were obtained at room-temperature except for Li above 21 GPa (160-200 K) and H_2 below 10 GPa (5 K). The figure is taken from [99].

At room-temperature Cs exhibits a complex sequence of phase transitions under pressure: bcc → fcc at 2.3 GPa, → *oC*84 at 4.2 GPa [100], → *tI*4 at 4.3 GPa [101], → *oC*16 at 11 GPa [96], → dhcp at 72 GPa and persists to 92 GPa [102]. A very similar sequence is observed in Rb: bcc → fcc at 7 GPa [103], → *oC*52 at 13 GPa [104], → h-g at 17 GPa [105], → *tI*4 at 20 GPa [106], → *oC*16 at 48 GPa and persists to 101 GPa [107, 108]. With increasing pressure, the Pauli exclusion principle and wavefunction orthogonality force the conduction electrons into the interstitial regions between atomic cores. The shape of the interstitial region is not spherical but highly irregular, which promotes *p*- and *d*-band occupancy compared to *s*-band occupancy [99]. At sufficiently high density the heavy alkali metals Cs and Rb essentially become monovalent *d*-

electron transition metals. The pressure-driven *s-d* transition is believed to destabilize the highly symmetric low-pressure structures (bcc and fcc) and favor complex, lower symmetry structures [97]. The 6*s* → 5*d* transition in Cs was calculated to begin at 3 GPa and be complete at 15 GPa whereas the 5*s* → 4*d* transition in Rb was calculated to finish at 53 GPa [109].

Besides the fact that the *s-d* transition can drive structural transitions in the heavier alkali metals, the drop in near infrared resistivity at the phase boundary between Cs fcc → *oC*84 and Rb fcc → *oC*52 observed by K. Takemura and K. Syassen (see Figure 4.16) can also be explained within the *s-d* transition picture [103]. The complex melting curve of Cs, featured by two maxima and a negative dT_M/dP slope from 3 GPa to 4 GPa (see Figure 4.17), is related to the *s-d* transition as well [110]. Similar characteristics in the melting curve of Rb were also observed [111].

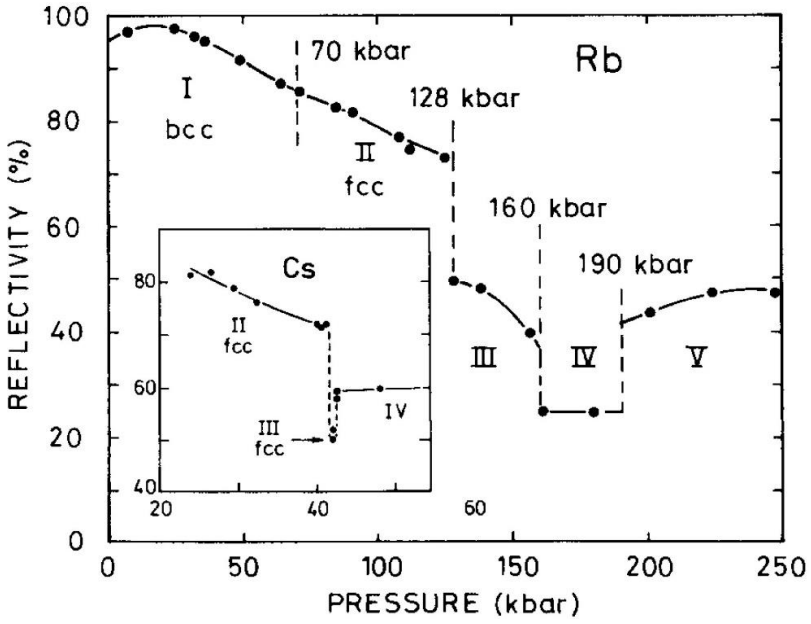

Figure 4.16: Pressure scan of the near-infrared reflectivity (~ 0.7 eV) of polycrystalline Rb metal in the pressure range 0 - 250 kbar. In the inset a similar pressure scan (~ 0.6 eV) for Cs metal is shown on a different pressure scale. The figure is taken from [103]. Note that the Cs III structure is determined as *oC*84 instead of fcc later [100] and the Rb III is determined as *oC*52.

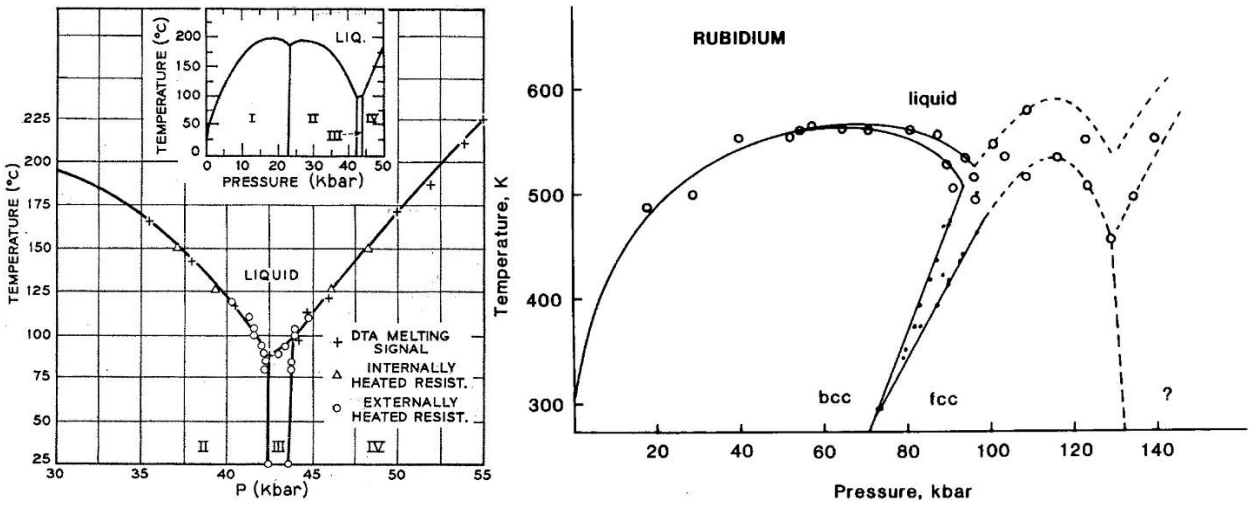

Figure 4.17: *T-P* phase diagram of Cs (left, taken from [110]) and Rb (right, taken from [111]). The phase diagram of Rb above 100 kbar is incomplete but the trend within the data scatter is shown by the dashed curves. Open circles are melting points. Solid dots represent the bcc-fcc transition.

Neither Cs nor Rb is superconducting at ambient pressure. This is not surprising since the density of states at the Fermi level is small and the electron-phonon interaction weak in these nearly-free-electron metals. However, superconductivity in Cs and Rb at high pressure, especially when pressure is high enough to drive the *s-d* transition, can be expected due to the increased importance of *d*-band states. Cs is the first alkali metal to become superconducting under high pressure. In 1970 Wittig [8] sealed a very air-sensitive Cs sample in a stainless-steel capillary and measured the resistivity of the capillary and Cs under quasi-hydrostatic pressure up to 15 GPa. He found that Cs superconducts around 1.4 K within a small pressure window from 12 to 14 GPa (see Figure 4.18 (left)). In later work [112] Wittig measured Cs directly whereby he confirmed superconductivity near 13 GPa and discovered a new superconducting region starting at 50 mK near 11 GPa. From Figure 4.18 (right) we can see that T_c first increases with pressure but then jumps to 1.3 K near the phase boundary between Cs IV *tI*4 and Cs V *oC*16. It is worthwhile to notice that the *s-d* transition in Cs is believed to end at 15 GPa. Based on the many

similarities between Cs and Rb, one could hope that superconductivity would appear in Rb, near 48 GPa where Rb V *tI*4 → Rb VI *oC*16 and the *s*-*d* transition almost ends. In fact, a search for superconductivity in Rb above 50 mK between 13 and 21 GPa in resistivity measurements was conducted by Wittig, but no superconductivity was found [113].

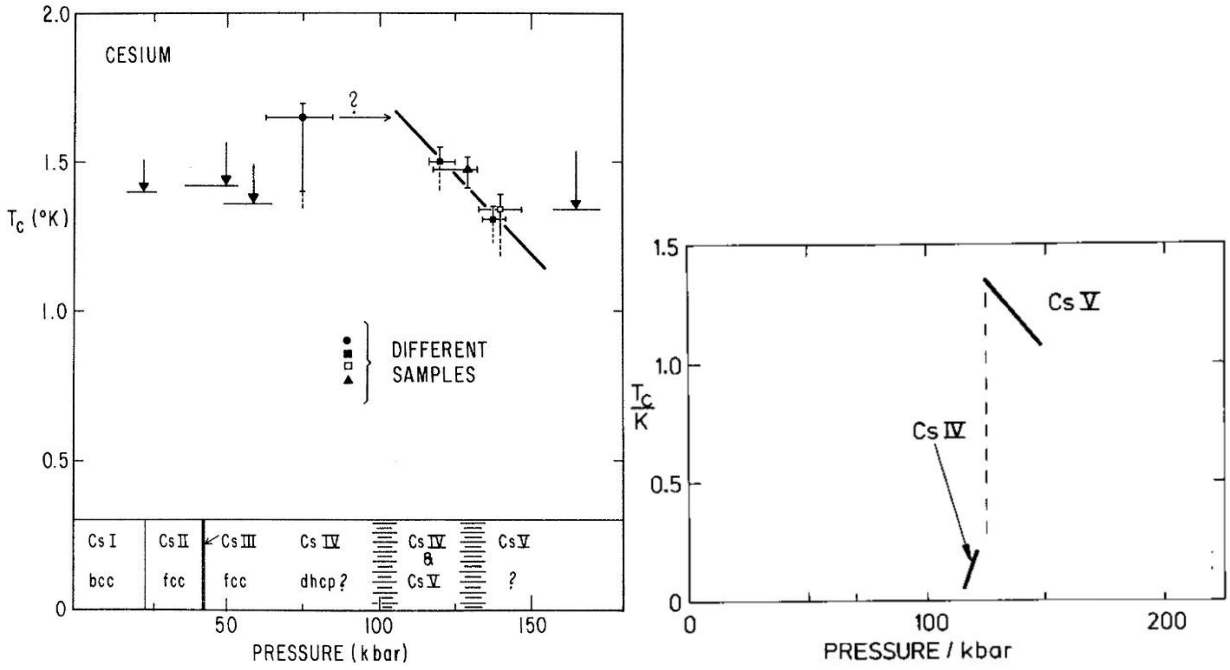

Figure 4.18: Superconducting transition temperature T_c versus pressure for Cs. Figures are taken from [8] (left) and [112] (right).

4.2.2Present Experiments

Instead of using the standard insulating gaskets as for the Sm and Y(Sm) experiments, due to the extreme softness of Cs and Rb bowl-style gaskets were prepared for the resistivity measurements (see "3.2.2 Gaskets"). After finishing a bowl-style gasket on the piston diamond, a ruby sphere can be placed either at the center of the body diamond culet or in the insulation layer just near the edge of the bowl. Unfortunately, if the ruby is placed at the body diamond culet, after closing the DAC it is usually buried inside the alkali metal, so that sometimes the ruby fluorescence is

too weak to detect. It is also somewhat problematic if the ruby is put in the insulation layer because it would be pushed away from the center under high pressures.

A small amount of Cs (99.98 % pure) or Rb (99.75 % pure) from Alfa Aesar was loaded into the bowl using the glovebox filled with ultra-high purity argon gas to minimize any reaction of Cs and Rb with oxygen and water vapor. Even with a trace oxygen content of only about 0.2 ppm, the DAC should be closed and torqued within 20 minutes for Cs and 30 minutes for Rb to seal the sample after it is loaded into the bowl. For Cs loading inside the glovebox, a special trick can be used to remove the oxides inside the metal: after placing Cs on a glass slide, use human body temperature to warm it until it melts (melting point of Cs is only 28.5^{o}C), then use a needle to remove the oxides which float on the surface of the liquid Cs. After letting the liquid Cs cool down and solidify, use the needle to take the shiny Cs inside as the sample to be measured.

Although much care has been taken, until now only five out of fourteen resistivity runs (run 7, 9, and 10 for Cs and run 3, 4 for Rb) have been completed. See Table 4.1 to get an overview of the cell specifications. The main reasons for failures include 1) oxidization of the sample because of bad sealing conditions in the DAC, and 2) shorting between the sample and the gasket, especially at high pressures. The electrical resistance measurements under high pressure from ambient to low temperatures were conducted using the four-point method with an ac current of about 1 mA at 17 or 34 Hz. The sample voltage was amplified by an SR554 preamplifier and input into an SR830 lock-in amplifier. Measurements with dc current were also attempted and the same value of resistance obtained, but the signal-to-noise ratio in the dc experiments was significantly lower than in the ac experiments, so most of the experiments were carried out using an ac current with lock-in technique. On the other hand, in the temperature region below 4 K dc measurements often gave superior results.

Table 4.1: Cell specifications used in Cs and Rb runs

	Anvil diameter (mm)	Gasket hole diameter (mm)	Bowl diameter (mm)	Pressure gauge	Highest pressure at RT (GPa)	Sample-gasket short	Why stop?
Cs Run 7	0.5	0.26	0.15	vibron	45	no	Pressure limit
Cs Run 9	0.9	0.45	0.15	ruby	14	no	Pressure limit
Cs Run 10	0.3	0.15	0.10	ruby	91	at 91 GPa	Pressure limit, short
Rb Run 3	0.5	0.26	0.15	vibron and ruby	78	no, kOhm contact	Pressure limit
Rb Run 4	0.5	0.26	0.10	vibron	75	no	Pressure limit

Unfortunately, there is only one run (Cs Run 9) in which ruby fluorescence could be measured during cooling/warming allowing us to follow how the pressure changed with temperature for a measurement using a bowl-style gasket and diamond anvils with 0.9 mm diameter culet. In Figure 4.19 the change in pressure during cooling is plotted. As can been seen, the pressure increases gradually during cooling; at 10 K $\Delta P/P_{RT}$ saturates at approximately 17%. This calibration will be useful when a bowl-style gasket is used to perform resistivity measurements on soft alkali metals like Cs and Rb where the ruby manometer is not available.

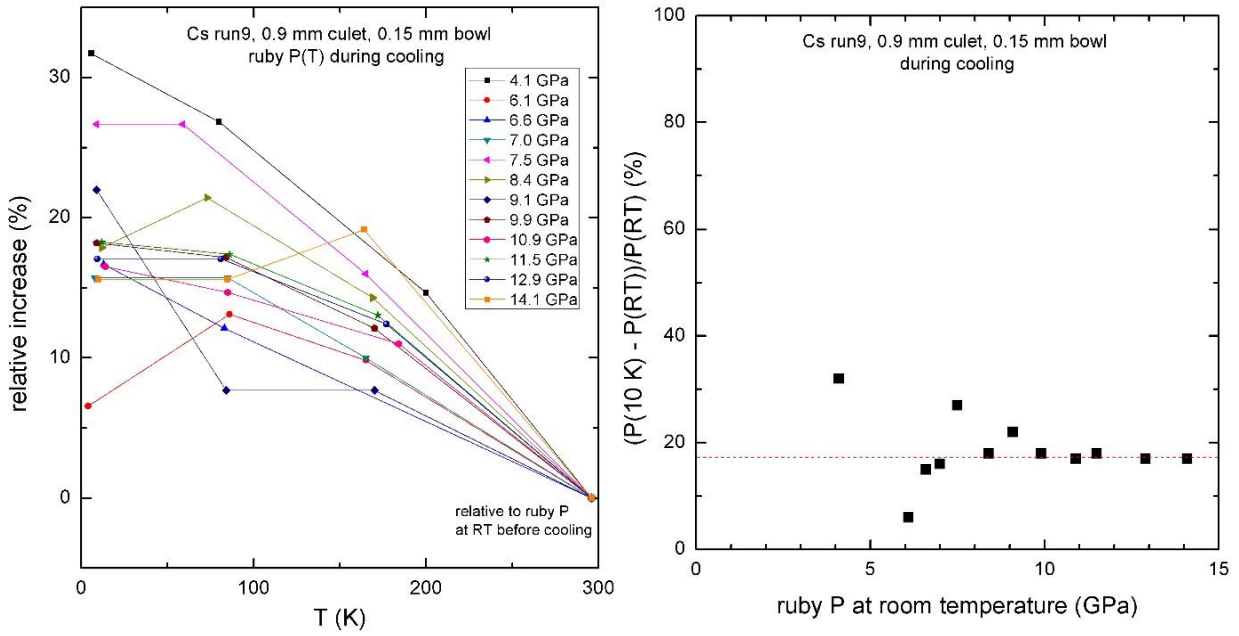

Figure 4.19: Relative pressure increase versus temperature for different pressures (left) and the relative change in pressure at 10 K versus pressure at room-temperature (right). This can be used as a pressure calibration when using a bowl-style gasket and diamond anvils with 0.9 mm diameter culet in resistivity measurements on Cs.

For the resistivity measurements on lanthanides such as Nd, Tb, and Dy, the thin square sheet of the lanthanide sample was directly placed on the surface of the flat cBN-epoxy layer. This setup has proven to be very successful: usually no electrical shorting between the samples and Re gaskets appears up to 150 GPa. Cs was the first alkali metal sample I measured under pressure. In order to confine the very soft Cs, a bowl acting as the sample chamber is drilled at the center of the cBN-epoxy layer. The thin wall of this bowl is the weak point of the resistivity pressure cell where Cs can break through to short with the gasket. Many tries failed before the final three successful runs. The results will be presented below in chronological order.

Experiments on Cs metal

In run 7 0.5 mm culet diamond anvils were used to measure the high-pressure resistance of Cs up to 45 GPa, thus tripling the pressure range of Wittig's previous work [8, 112]. Figure 4.20 shows

selected $R(T)$ curves of Cs. A sudden resistance drop was found at 10 GPa, with an onset transition temperature of about 1.4 K. For pressures below 6 GPa or above 11 GPa, no such drop was found. This sharp resistivity drop thus confirms the superconducting transition in Cs reported by Wittig. The present experiments also demonstrate that the pressure region where Cs superconducts is quite limited, probably smaller than 5 GPa.

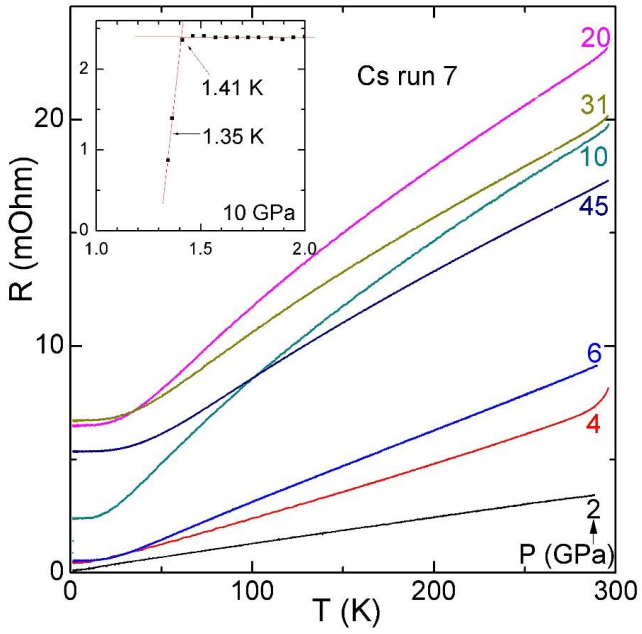

Figure 4.20: Selected $R(T)$ data for Cs showing the superconducting transition at 1.4 K and 10 GPa (room temperature pressure) in run 7. The numbers on the right side of the curves give room-temperature pressures. The inset magnifies the superconducting transition at 10 GPa.

Figure 4.21 gives the room-temperature resistance minus the residual resistance at 4 K versus pressure. It appears that the resistance of Cs rises quickly near the phase boundary between the *tI*4 and *oC*16 phases. This strong increase in the resistance at room-temperature suggests an enhanced electron-phonon interaction that would favor superconductivity. The superconducting transition was detected at the pressure where the resistance is at its maximum. When Cs fully enters the *oC*16 phase, the resistance continuously decreases with pressure. Compared to the $R(P)$ curve of Wittig [112], the resistance upturn found here is at a lower pressure; this may be

due to the fact that a relatively low pressure is difficult to measure accurately from the diamond vibron spectrum. The results from runs 9 and 10 where a ruby pressure gauge was applied will be discussed later.

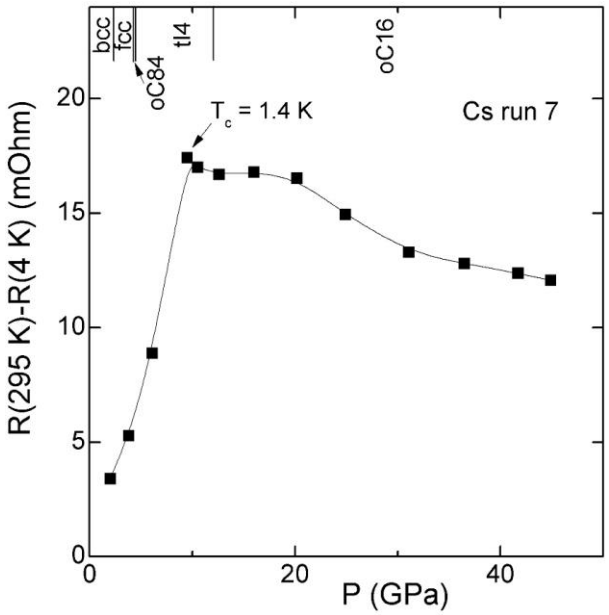

Figure 4.21: Room-temperature resistance with residual resistance subtracted off versus pressure in run 7. The phases taken on by Cs at room-temperature [100] are given at the top of the figure.

To explore the superconducting phase diagram of Cs more carefully, diamond anvils with 0.9 mm culet were used in run 9. *R*(*T*) curves up to 14.2 GPa are shown in Figure 4.22. This time the ruby pressure, rather than the vibron pressure, was measured at several points during cooling and warming. The superconducting transition appeared above 13.6 GPa (pressure at low temperature). The resistance did not decrease to zero even at the lowest temperature of 1.35 K, but the resistance drop began at about 1.5 K. That the resistance did not fall to zero may be the result of a sizeable pressure gradient across the sample since no pressure transmitting medium was used in these experiments. A similar result was obtained by Ullrich, Probst, and Wittig [114] who measured the resistance of Cs at 13 GPa down to 0.5 mK by using a ^{3}He-^{4}He cryostat and

found the superconducting transition at this pressure began at 1.4 K, dropped by half at 1.25 K, then finally fell to within only 2% of the 4K-value at 50 mK, never fully reaching 0.

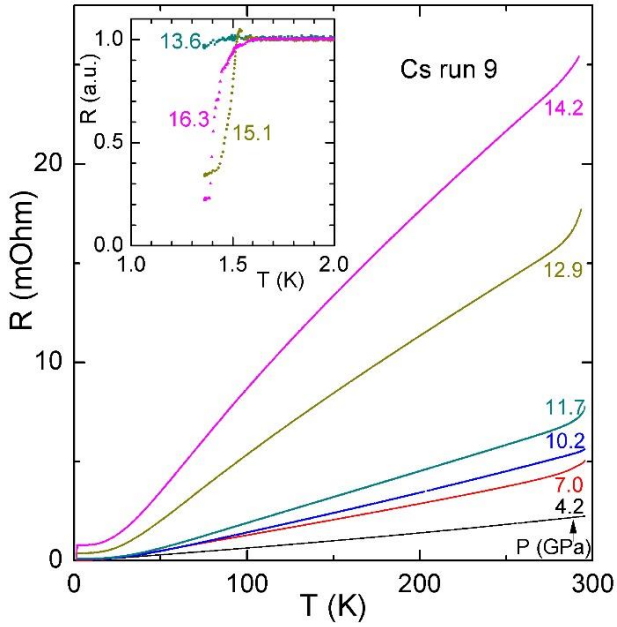

Figure 4.22: Selected $R(T)$ curves of Cs in run 9. Inset shows the normalized curves where sudden resistance drops appeared at low temperature. Note that in the inset pressure values near the transition temperatures are given. Pressures 11.7, 12.9, and 14.2 GPa at room-temperature increased to 13.6, 15.1, and 16.3 GPa at low temperature, respectively.

The $R(P)$ data at room-temperature in run 9 are shown in Figure 4.23. The pressure was increased at room-temperature and the resistance monitored. As pressure was increased from 6.8 GPa to 7.2 GPa, a peak in $R(P)$ was observed. After appearing it then disappeared after several minutes, so that the pressure where it first occurred can only be estimated to be near 7.0 GPa. This peak is so sharp that in run 7 we did not see it because of the larger pressure steps taken there. A flat-topped spike in $R(P)$ at room-temperature for Cs was also found by Hall *et al*. [115], but at a lower pressure region between 4.2 to 4.3 GPa. Hall *et al*. attributed this spike to the Cs III phase (which was later determined to be the *oC*84 structure [100]). Here, in run 9, the resistance was measured in a non-hydrostatic pressure environment whereas Hall *et al*. used the

more hydrostatic silver chloride as pressure medium. This may cause the difference in pressure where the resistance peak appeared. Similar to what was found in run 7, a rapid increase in $R(T)$ began at 12 GPa, just at the phase boundary between *tI*4 and *oC*16. This is also the region where Cs becomes superconducting.

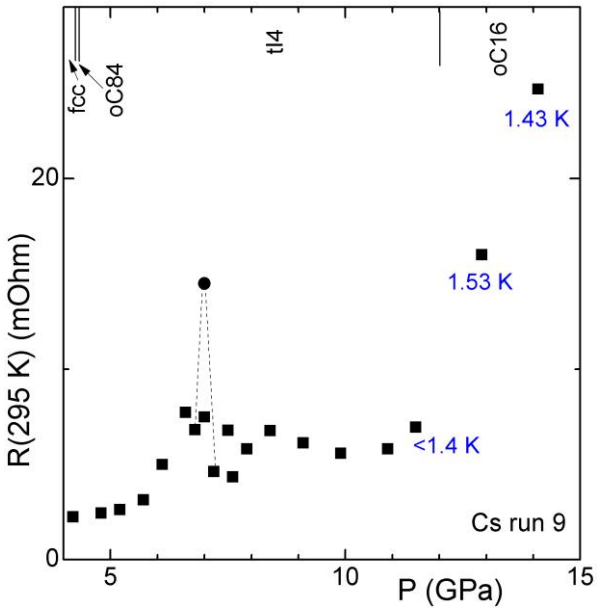

Figure 4.23: Room-temperature resistance versus pressure in run 9. Pressures where superconducting transitions of Cs were found are marked by blue transition temperature values. The solid circular dot represents a resistance peak at pressure between 6.8 and 7.2 GPa.

Magnetic fields as high as 98 G were applied to study the field-induced suppression of superconductivity as seen in Figure 4.24. Since the resistance did not go to zero, the transition temperature is defined as the intersection point of two straight lines through $R(T)$ data of normal state and superconducting state, respectively. At both pressures T_c was suppressed by a magnetic field. For the superconductivity at 15.1 GPa, the initial suppression effect is about 0.003 K/G, a smaller value indicated at 16.3 GPa.

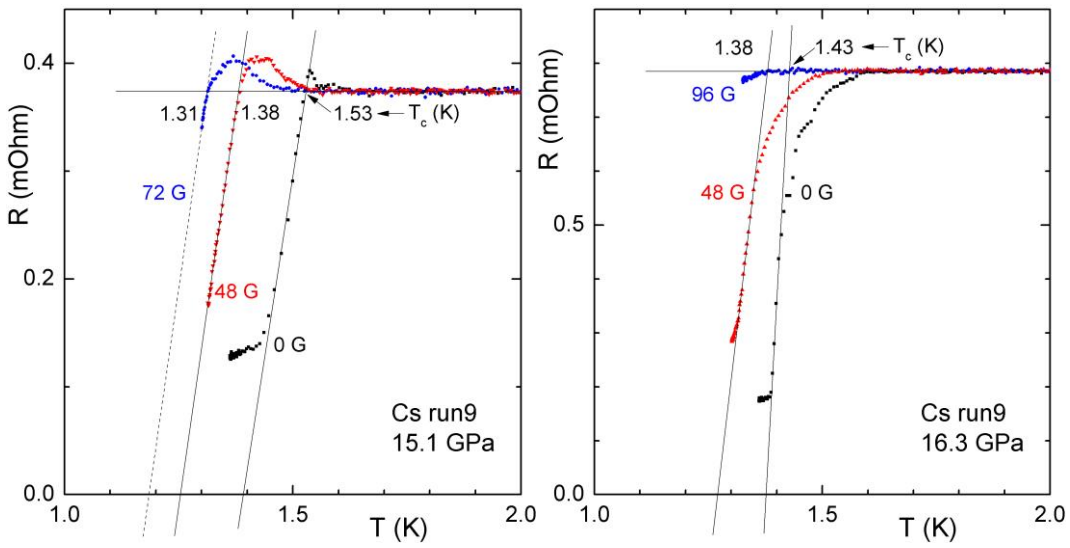

Figure 4.24: Magnetic field suppression of the superconducting transitions in Cs in run 9.

Run 10 was conducted solely at room-temperature to obtain an accurate measurement of $R(P)$ at this single temperature. Pressure was gradually increased to 91 GPa. Afterwards an electrical short between the sample and the Re gasket was noticed since the resistance became very unstable after a night of relaxation: it changed to an extent that cannot be explained by a relaxation of the sample after increasing pressure. I was not sure if the short happened before 91 GPa.

Another problem with this run is that pressure was determined at lower pressures by ruby fluorescence but at higher pressures by the diamond vibron gauge. This is because the pressure gradient became very large: at the highest pressure, the ruby pressure at the edge of the sample was 56 GPa but the vibron pressure at the center of the sample was 91 GPa. In order to determine pressure, a B-spline function was adopted to fit the sample pressure vs. membrane pressure relation based on several reliable data sets (see Figure 4.25 (left)), yielding the $R(P)$ curve in Figure 4.25 (right). A resistance peak shows up around 7.5 GPa, followed by an upturn starting

at 14 GPa. These are consistent with results in run 9. When Cs transfers into the *oC*16 phases, the resistance begins to decrease.

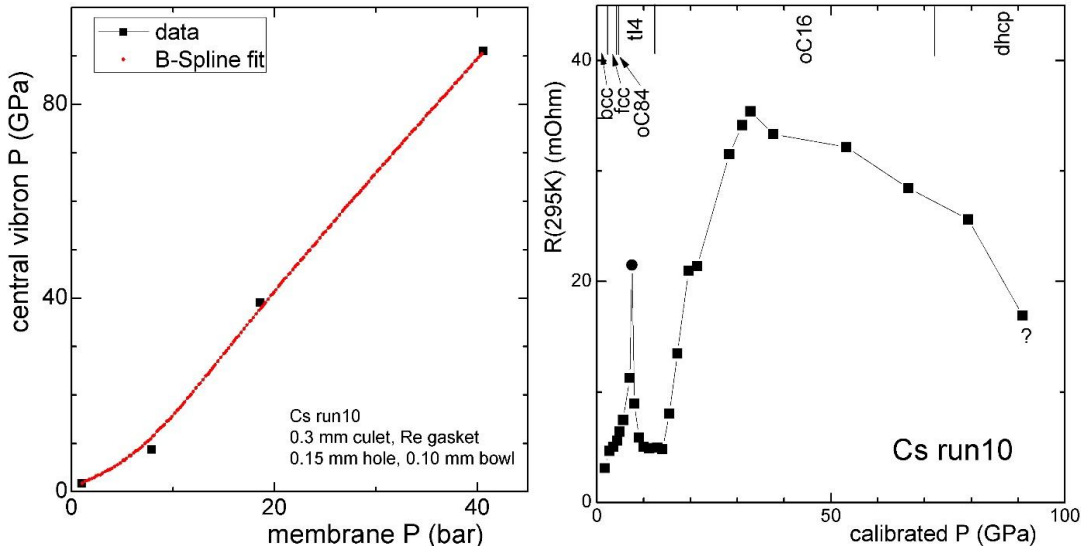

Figure 4.25: (left) Fitting of the vibron pressure versus membrane pressure and (right) room-temperature resistance of Cs versus calibrated pressure (right) in run 10. A B-spline function (red dotted line) was used to fit the sample pressure-membrane pressure relation. The question mark near a data point in the *R*(*P*) curve means the resistance at this pressure may be influenced by the electrical shorting problem.

Experiments on Rb Metal

Four experiments were conducted on Rb. Pressures were applied at room-temperature and determined by a diamond vibron gauge. After applying pressure the sample was held at room-temperature for a sufficiently long time (several hours or overnight) to yield a stable resistance reading. In runs 1 and 2 an electrical short between the Rb sample and Re gasket appeared at 14 GPa and 7 GPa, respectively. In run 3, a contact of about 1 - 100 kOhm appeared at 13 GPa; fortunately, this contact resistance did not decrease at higher pressures. Note that the transition from Rb II to Rb III occurs at 13 GPa with a volume collapse of 2.5 %. This transition could conceivably have led to the failure of the insulation between the Rb sample and Re gasket if the sudden volume collapse resulted in micro-cracks in the rigid cBN-epoxy insulation. The

measured resistance in run 3 potentially contains contributions from both the Rb sample and the Re gasket. Special care should be taken when searching for superconducting transitions, especially in the 1.7 - 4 K temperature region, where Re superconducts. In run 4 no short was observed for pressures up to 63 GPa, but a short of about 20 Ohm appeared as pressure was increased from 63 to 65 GPa. However, the strong similarity between the $R(T)$ curves at 65 GPa and 63 GPa demonstrates that the short between a sample wire and the gasket has little or no influence on the measurements. The short remained to the highest pressure (73 GPa) but then disappeared when pressure was reduced below 56 GPa.

In all runs a sudden reduction in reflectivity at ~ 7 GPa pressure was observed, as seen in Figure 4.26. Similar phenomena were reported earlier by K. Takemura and K. Syassen [103]; these authors related this anomaly to the bcc (Rb I) to fcc (Rb II) phase transition at 7 GPa. At pressures higher than 9 GPa, no obvious change in reflectivity was observed from the surface of the Rb sample.

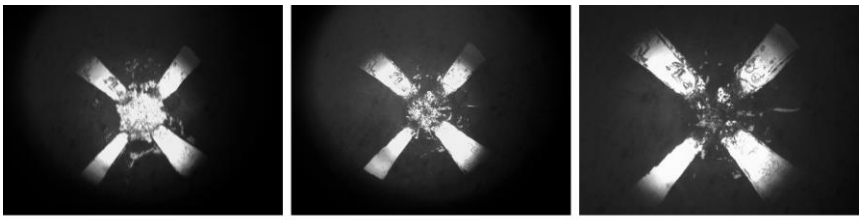

Figure 4.26: Change in reflectivity of Rb where a transition occurs at 5 - 9 GPa pressure. The reflectivity of the four shiny Pt electrical leads to the sample does not change under pressure.

Figure 4.27 presents the temperature-dependent resistance of Rb in run 3 during cooling at different pressures to 78 GPa. The resistance was measured over the temperature range 295 K to 1.3 K. Above 59 GPa a tiny resistance drop appears below 2 K. This drop is barely visible at 78 GPa. After reducing pressure to 57 GPa and then 55 GPa, the drop shifts up to approximately 2.1

K and becomes larger. Because the pressure increases with decreasing temperature down to approximately 50 K, it is not possible to give a quantitative analysis of the dependence of the resistance $R(T)$ on temperature over the entire temperature range. If the sample is at a pressure where R increases sharply with pressure, then when T decreases the increase in pressure would cause R to increase. In transition metals the *s-d* electron scattering effect gives a negative curvature to $R(T)$, as seen in the data in Figure 4.27 beginning at 20 GPa. For Rb the *s-d* transition is predicted to end at 53 GPa [109].

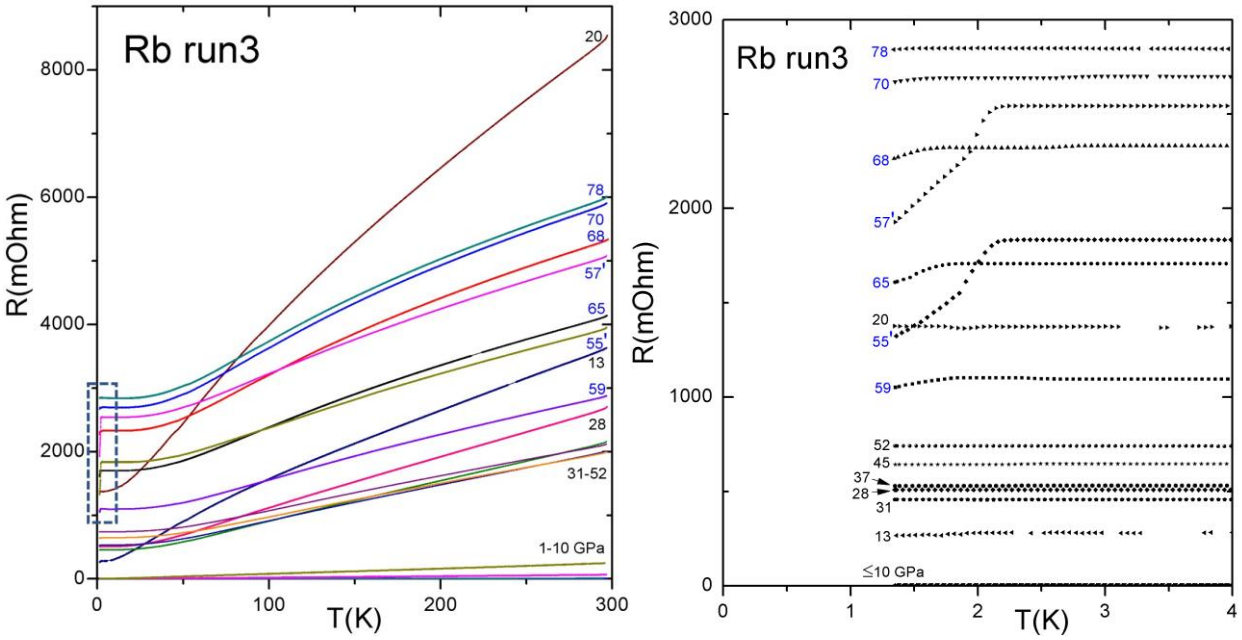

Figure 4.27: $R(T)$ of Rb at various pressures up to 78 GPa in run 3. The pressures were measured at room-temperature. The dashed blue square encloses the region where resistance drops appear below 2.2 K (except for the curve at 20 GPa), which can be seen more clearly in Figure 4.27 (right). Values of pressure in GPa at room-temperature are given to the right. The prime symbol following the number identifies data were taken upon reducing pressure.

Figure 4.28 demonstrates how the resistance of Rb at room-temperature (with the residual resistance subtracted off) changes dramatically with pressure. The residual resistance comes from the defects in the sample and should be deducted from the room-temperature resistance in order to gain information about the intrinsic electron-phonon scattering at room-temperature. A

very strong peak in [R(295 k) - R(4 K)] centered around 20 GPa is observed, followed by a plateau from 30 to 50 GPa. In the *R*(*P*) data for Cs at room-temperature, a resistance peak also appears after Cs leaves its fcc phase for the complex structures with low symmetry, similar to what happens here in Rb. Both peaks are far too large to be attributed to the respective volume collapse. The peaks in *R*(*T*) for Cs and Rb are likely related to the dramatic changes in the electronic structures of the heavy alkali metals due to structural phase transitions generated by *s*-*d* charge transfer. When the pressure is higher than 50 GPa near the Rb *tI*4 to *oC*16 structural transition, a rapid upturn in *R*(*P*) appears that ends near 70 GPa. Accompanying this upturn is the emergence of a sudden resistance drop below 2.2 K seen in Figure 4.27 (right). In Cs this correlation is also seen: Cs becomes superconducting where the room-temperature resistance soars upward, beginning at the phase boundary between its *tI*4 and *oC*16 phases. The striking similarity between Cs and Rb would seem to suggest that the small resistance drop near 2 K in Rb comes from a superconducting transition.

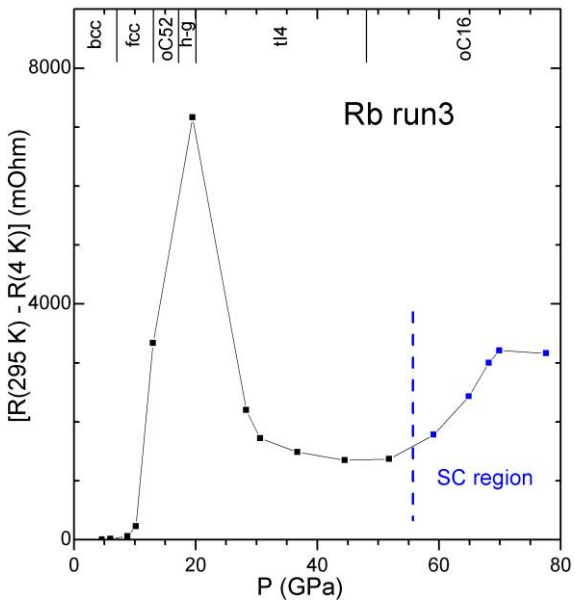

Figure 4.28: Room-temperature resistance minus 4 K resistance versus pressure in run 3. The pressure region where an indication of possible superconductivity of Rb was found is the right side to the dashed blue line. The structural phase diagram of Rb at room-temperature is at the top of the figure [104].

A magnetic field up to 500 G was applied to test whether the temperature (T_c) of the small resistance drop for Rb shifts downward. The result of a typical run is shown in Figure 4.29. At 65 GPa (room-temperature pressure), the resistance starts to decrease at 1.7 K. This resistance downturn shifts to progressively lower temperatures as a magnetic field at 240 G and 480 G is applied. After the field is turned off, T_c returns to the original value. These results give strong evidence that the resistance drop is due to a superconducting transition, either from the Rb sample or the Re gasket. Note that at ambient pressure Re superconducts at 1.7 K. However, under shear strain the T_c of Re can be as high as 3.1 K [116, 117]. More resistance measurements on Rb free of contact between Re gasket and Rb sample are necessary to establish whether the small resistance drop near 2 K seen here arises from superconductivity in the Rb sample.

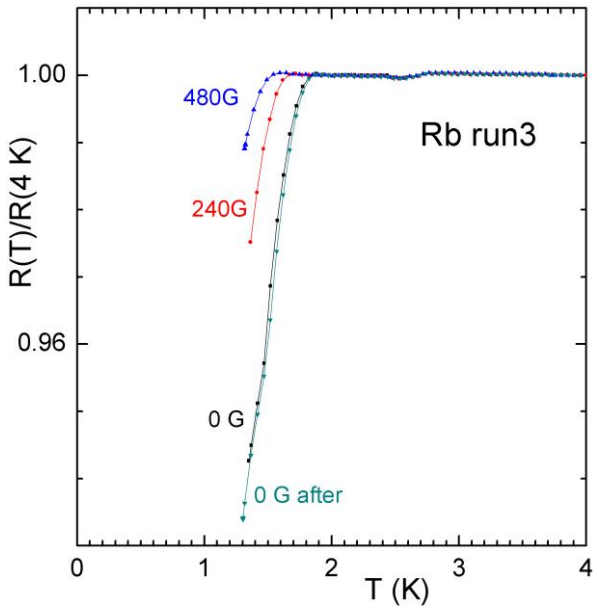

Figure 4.29: Applying a magnetic field suppresses the sudden resistance drop for Rb at 65 GPa in run 3. The four $R(T)$ curves shown have been normalized at 4 K.

Run 4 was conducted to further investigate the potential superconductivity in Rb under pressure. A smaller bowl drilled in the insulation layer helped to insulate Rb from the Re gasket at high

pressure. In addition, no ruby sphere was placed inside the sample in an attempt to obtain a more homogeneous pressure distribution in the sample. In this run sharp resistance drops greater than 30%, without any short problem, were observed at low temperatures for pressures above 48 GPa, giving convincing evidence that Rb does indeed become superconducting under high pressure. I now discuss the extensive results of run 4 in detail.

In run 4 the resistance was first measured at room-temperature while increasing pressure up to 57 GPa (see Figure 4.30), placing it in the *o*C16 phase. This reduced the possibility of a phase mixture in the sample arising from the known pressure increase upon cooling. After every change in pressure between 57 and 73 GPa, the sample was cooled to 1.3 K. The pressure was then slowly reduced at room-temperature from 73 to 34 GPa and the sample kept at 34 GPa for two weeks before beginning the second measurement of *R(T)* with increasing pressure to 75 GPa (see red lines in Figure 4.30). Finally, pressure was reduced to 48 GPa where the sample was measured for the last time (point #17 in Figure 4.30).

As seen in Figure 4.30, a small resistance peak was observed near the bcc → fcc phase boundary followed by a rapid increase in resistance up to a sizable maximum. A sudden resistance drop appears at about 20 GPa where the h-g phase transforms to the *tI*4 phase. The room-temperature resistance then remains relatively constant until 48 GPa where it starts to rise rapidly as Rb begins to enter the *oC*16 phase. This *R*(*P*) behavior is qualitatively similar to that seen in run 3. Upon reducing pressure a hysteresis in the pressure-dependent resistance *R*(*P*) appears, indicating that the *tI*4 to *oC*16 phase transition is first order in nature.

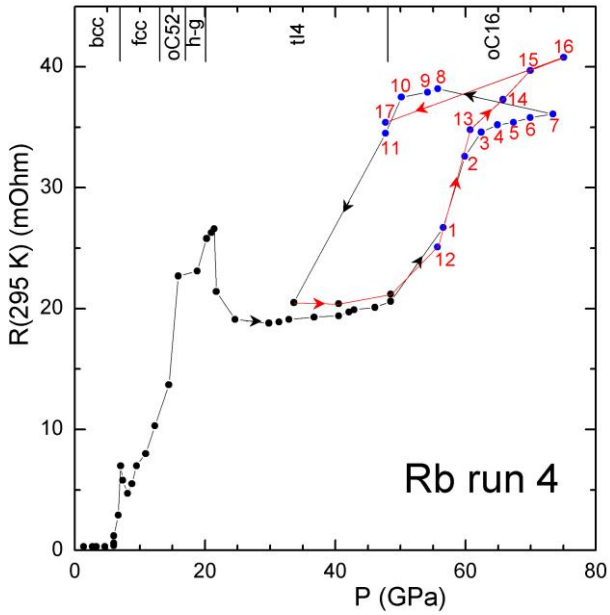

Figure 4.30: Dependence of resistance of Rb on pressure at room-temperature in run 4. The phase diagram of Rb at room-temperature is at the top of the figure [104]. Data points where superconductivity was found are blue. The order of measurement is indicated by red numbers. Several data points were taken upon reducing pressure, leading to the hysteresis loop in *R(P)* near the *o*C16 → *tI*4 transition. The four black arrows indicate the first increasing/decreasing pressure run whereas the four red arrows indicate the follow-up increasing/decreasing run.

Figure 4.31 gives several selected temperature-dependent resistance curves *R*(*T*) for Rb in run 4 over the entire measured temperature range at selected pressures. All curves show a negative curvature over a wide temperature range, a signature of transition-metal-like behavior. This is also observed in *R*(*T*) above 6 GPa for Cs (see Figure 4.20). At temperatures below 3 K, the resistance decreases abruptly by more than 30 %. For those curves obtained as the pressure is decreased, the resistance drop can be as high as 98 % (for example the reduced 48 GPa, #17).

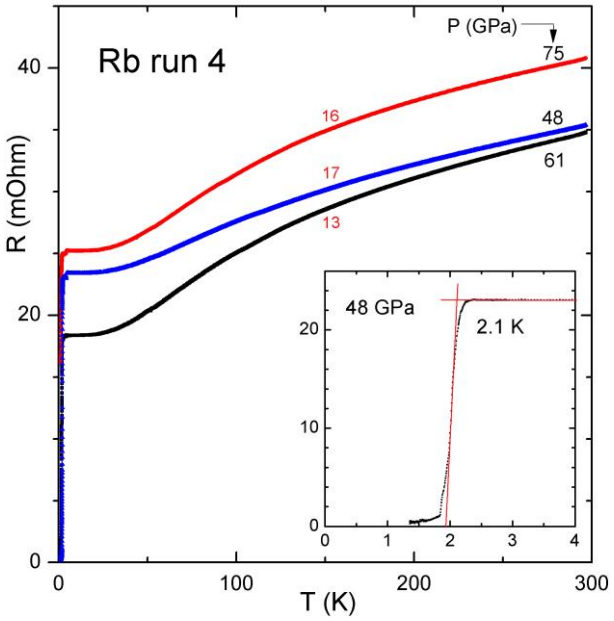

Figure 4.31: Selected $R(T)$ of Rb at different pressures in run 4. $R(T)$ of Rb down to 1.3 K was measured at 57, 60, 63, 65, 67, 70, 73, 56, 54, 50, 48, 34, 56, 61, 66, 70, 75 and 48 GPa, in that order. All curves were obtained during cooling. The pressures in GPa at room-temperature are given in black numbers to the right. Red numbers give order of measurement taken from Figure 4.30. The inset shows the data at 48 GPa below 4 K.

In Figure 4.32 the details of the resistance drops are shown for 8 different values of pressure. It is clearly seen that T_c shifts to lower temperatures with increasing pressure, beginning at 2.5 K for 50 GPa and ending below 1.4 K above 75 GPa. Referring to Figure 4.30, the apparent superconducting transition occurs in the *oC*16 phase which has a much higher resistance than the *tI*4 phase.

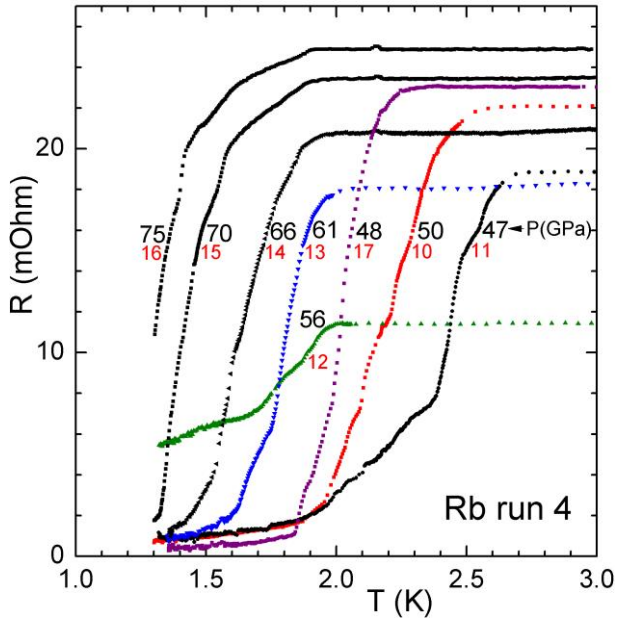

Figure 4.32: Selected $R(T)$ of Rb below 3 K at different pressures in run 4. The pressures in GPa at room-temperature are given, the red numbers indicating the order of measurement. The curves at 47, 48, and 50 GPa were obtained as pressure was reduced.

Both ac and dc currents with different amplitudes were applied to measure $R(T)$ below 4 K, as seen in Figure 4.33. At 54 GPa a 2 mA ac current is seen to lead to a heating effect in T_c of about 0.2 K compared to a measurement with 0.5 mA ac current; however, the scatter in the data is seen to be clearly reduced. Equally unusual is that the application of dc magnetic fields below 500 G reduces the scatter in the $R(T)$ data below 4 K. Another interesting observation in the $R(T)$ data at 50 GPa is that the scatter is also reduced if a dc current is used instead of ac, as seen in Fig. 4.33 (right). A 0.5 mA dc current thus appears to give superior results than an 0.5 mA ac current.

The scatter and kinks in the ac resistivity data near the superconducting transition are reversible and reproducible and thus come from the Rb sample itself and not from fluctuations in the measurement signal. It would seem likely that they are the result of inhomogeneities in the

sample where the electron current flows through regions of strong and weak superconductivity. As the primary current is increased or a magnetic field applied, the weakly superconducting regions become normal, channeling the electron current through sample regions of relatively stable superconductivity. Through many tries, 1 mA dc has been proven to be the optimal current to measure $R(T)$ below 4 K - - little scatter and negligible heating effect.

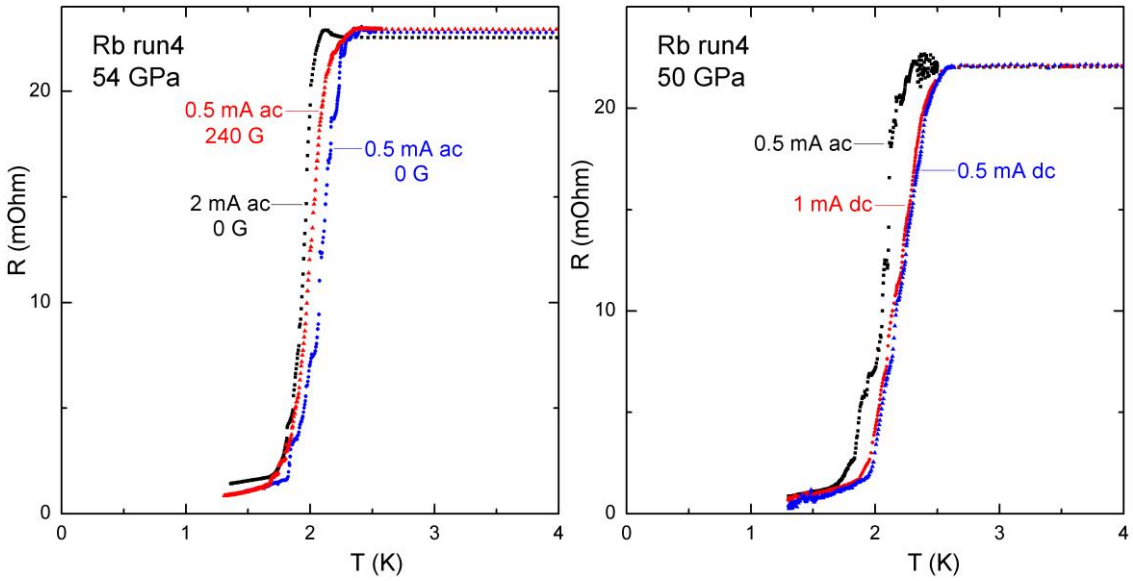

Figure 4.33: $R(T)$ in run 4 below 4 K using ac and dc currents of different magnitudes with and without magnetic field.

The effect of a dc magnetic field on the superconducting transition is shown in Figure 4.34, together with the inset where the $H_c(T)$ data at 61 and 66 GPa are fit using Eq. 2.28. The application of a magnetic field is seen to reversibly shift the superconducting transition to lower temperatures. At 61 GPa the critical field at 0 K, $H_c(0)$, is estimated to be about 1370 G; at 66 GPa $H_c(0)$ is approximately 1310 G. Considering the low value of T_c, $H_c(0)$ for Rb is somewhat higher than for the elemental metal superconductors: Pb (T_c = 7.2 K, $H_c(0)$ = 800 G); Hg (T_c = 4.2 K, $H_c(0)$ = 400 G); Al (T_c = 1.2 K, $H_c(0)$ = 100 G). The downward shift of these sharp

transitions under magnetic field gives strong evidence that the transition is indeed due to the superconducting state of Rb.

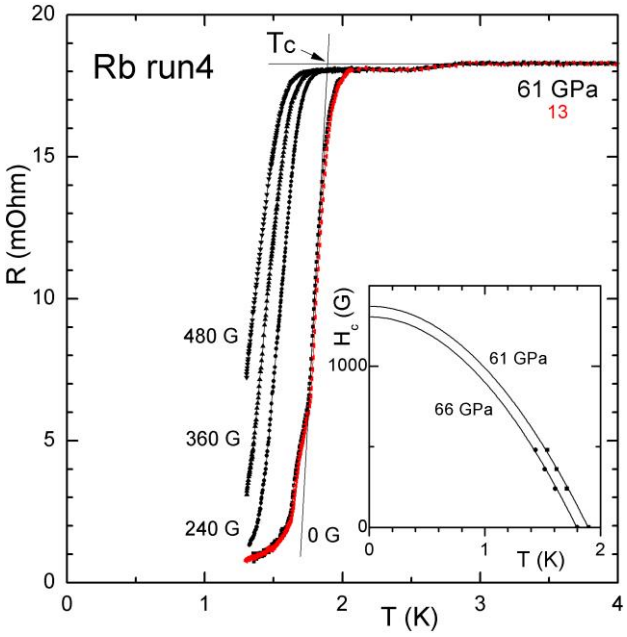

Figure 4.34: Magnetic field suppression of the superconducting transitions in Rb in run 4 at 61 GPa (room-temperature pressure), the #13 data point in Figure 4.30. Inset: $H_c(T)$ fit with the standard empirical formula Eq. 2.28 at 61 and 66 GPa. T_c is defined as the intersection point of two straight lines through $R(T)$ in both the normal state and the superconducting transition.

4.2.3 Discussion

It would be interesting to compare the occurrence of superconductivity in Cs and Rb since they share so many common properties under pressure, such as a similar crystal structure sequence, similar anomalies in the near-infrared reflectivity, and similar minima in the *T*-*P* phase diagrams. Figure 4.35 shows T_c and room-temperature R vs pressure for Cs and Rb side by side. After these two heavy alkali metals enter the *oC*16 phase, the resistance displays a significant increase with pressure, accompanied by the appearance of superconductivity where the transition temperature T_c decreases with pressure. The T_c of Cs is lower than that of Rb, perhaps due to the greater atomic mass of Cs, as would be expected from a conventional isotope effect. Cs has T_c^{max} = 1.5

K at 12 GPa whereas for Rb T_c^{max} = 2.5 K at 60 GPa. Their neighbors to the right in the periodic table, Ba has T_c^{max} = 5 K at 18 GPa [118] (Ba IV, incommensurate h-g structure) whereas Sr shows T_c^{max} = 8 K at 58 GPa [119] (Sr V, incommensurate h-g structure). It is interesting to note the similar trend in (T_c^{max}, P) between the pair of heavy alkali metals and the pair of heavy alkaline earth metals where in both cases it is generally thought that pressure induced *s-d* electron transfer leads to the superconductivity, the alkaline earth metals showing a maximum T_c in the Ba-IV type structure when the *s-d* transfer is complete [120].

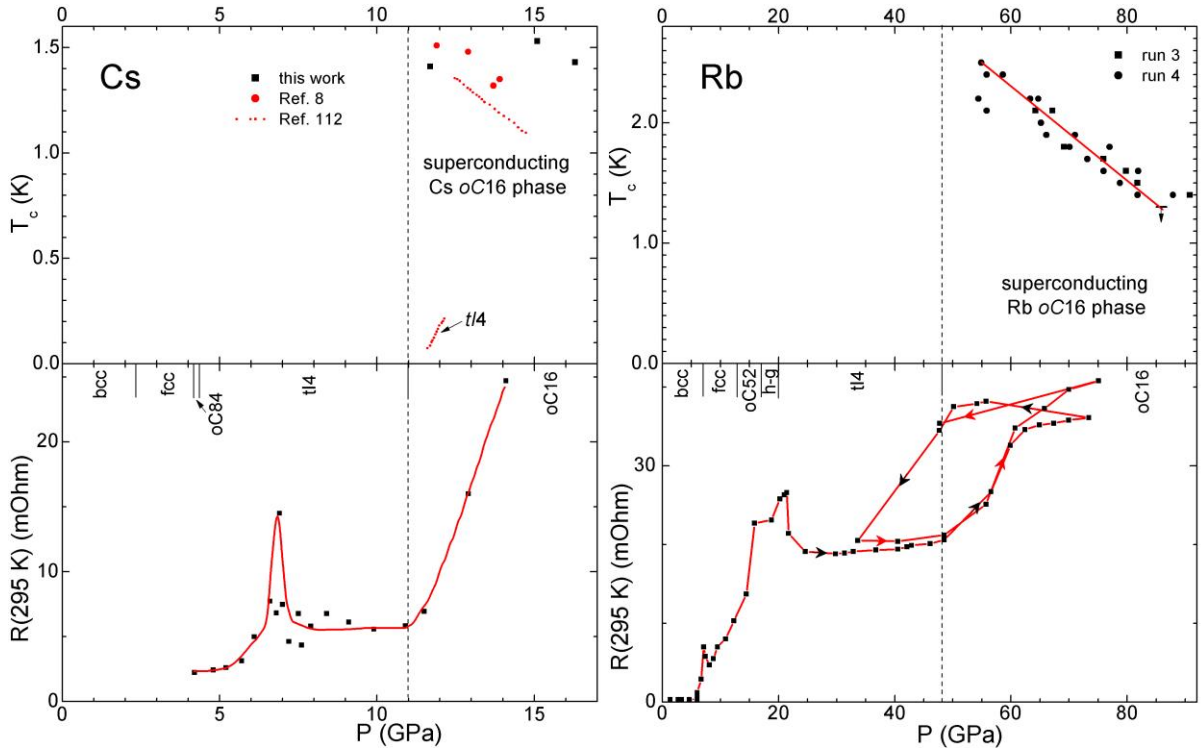

Figure 4.35: Superconducting transition temperature T_c and room-temperature resistance R of Cs (left) and Rb (right). The pressures in the lower panels were measured using the diamond vibron at room-temperature while the pressures in the upper panels are the estimated pressures at low temperature (see p.88), except for the two highest pressure points for Cs where the ruby pressure was measured at low temperature. For Rb several measurements were made upon reducing pressure, leading to the hysteresis loop in $R(P)$ near the *oC*16 → *tI*4 transition (see Figure 4.30). The four black arrows indicate the first increasing/decreasing pressure run whereas the three red arrows indicate the follow-up increasing/decreasing run. The structural phase diagrams of Cs [100] and Rb [104] at room-temperature are given at the top of the figures. Note that the transition from *tI*4 to *oC*16 of Cs or Rb is sluggish at room-temperature: it begins at 11 GPa and completes at 12 GPa for Cs [96]; it begins at 48.5 GPa and does not complete even at 50 GPa for Rb [107].

It is widely believed that *s*-*d* electron transfer plays a dominant role in the occurrence of phase transitions, temperature-dependent resistivity, and superconductivity in Cs and Rb. McMahan [109] calculated the completion pressure for the *s*-*d* transfer in Cs and Rb to be 15 GPa and 53 GPa, respectively. Near these two critical pressures Cs and Rb undergo the phase transformation *tI*4 → *oC*16, a steep increase in resistance, and the appearance of a superconducting transition at low temperature, as shown in Figure 4.35. One explanation for the correlation between the pressure induced phase transitions and the *s*-*d* transfer is that the anisotropic *d*-wavefunction favors the low-symmetry phases like *oC*52, *oC*84, h-g, and *oC*16 over the high-symmetry phases like bcc and fcc [97]. As for the *s*-*d* transfer related resistance increase, it can be due to (1) additional scattering channels between *s* electrons and *d* electrons near the Fermi level and (2) the larger effective mass of electrons in the *d*-band. When the *s*-*d* transition is complete, no additional scattering channels are added, resulting in a saturated resistance. As a result the room-temperature resistance of Cs (Rb) first generally increases slowly before beginning a strong increase near the *tI*4 → *oC*16 phase transition at 11 (50) GPa, $R(P)$ finally bending over at higher pressures. For Rb the resistance above 50 GPa is two orders of magnitude higher than that at ambient pressure!

An *s*-*d* transition is also predicted to occur in K, with a completion pressure near 60 GPa [109]. Based on the fact that the T_c of Cs and Rb reaches its maximum at the pressure where the *s*-*d* transition is about to end, we may naively expect the appearance of superconductivity in K near 60 GPa, with a T_c higher than 2.5 K since K is the lightest of the three heavy alkali metals. However, the *tI*4 → *oC*16 transition in K occurs at 96 GPa (see Figure 4.14), a good deal higher than the 60 GPa predicted for the completion of the *s*-*d* transition in K. This contrasts with Cs and Rb where the calculated completion pressure agrees quite well with the phase boundary.

Superconductivity, therefore, may be expected to occur at a pressure closer to 96 GPa than 60 GPa. T. Tomita and S. Deemyad [121, 122] found no superconductivity in K above 1.5 K (4 K) to 35 GPa (43.5 GPa) hydrostatic pressure. M. Debessai [123] was unable to find any superconductivity above 1.35 K between 8 and 94 GPa non-hydrostatic pressure. N. Hillier [39] reported no superconductivity in K between 1.35 and 30 K up to 23.8 GPa non-hydrostatic P. All the above results on K were obtained by ac susceptibility measurements. High-pressure resistance measurements are a more sensitive probe for superconductivity and should be attempted on K to pressures near 100 GPa. When searching for superconductivity in K, particular attention should be paid to the pressure region where a sharp resistance rise occurs. Interestingly, for Li Lin and Dunn [124] found a resistance rise at room-temperature beginning at 16 GPa, very close to the pressure where superconductivity appears in fcc Li. In fcc Li the superconductivity is thought to be related to *s-p* rather than *s-d* electron transfer.

Both Cs and Rb in Group I become superconducting immediately after the phase transition from *tI*4 to *oC*16 occurs. Interestingly, the T_c of Si in Group IV peaks at 4.9 K near 39 GPa [125], exactly in the small pressure region from 38 to 43 GPa where Si takes on the *oC*16 structure between the neighboring primitive hexagonal (ph) and hexagonal close-packed (hcp) phases [126]. The T_c value for Si prior to the *oC*16 transition is 3.3 K, but 3.5 K in the *o*C16 phase. Schwarz *et al*. [107] pointed out the remarkable crystallographic similarities between these three *oC*16 phases (Cs V, Rb VI, and Si VI), and boldly predicted that Rb VI would be a candidate to look for superconductivity given that *oC*16 favors superconductivity for Cs and Si. The prediction has been confirmed in the present thesis.

Table 4.1 summarizes crystal structure information and several physical properties of Si, K, Rb, and Cs at those pressures where they are in their *oC*16 phase. The *oC*16 phase (SG *Cmca*, Z = 16)

can be described as a four-layer sequence of alternating buckled nearly square layers formed by the 8*d* atoms (Wyckoff notation) and flat layers of diatomic units formed by the 8*f* atoms [107]. The coordination number is 11 (10) for 8*f* (8*d*) atoms. Note that the four elements have almost the same axial ratios (*a*/*c* and *b*/*c*) and positional parameters (x, y, and z). Another interesting point are the similar values for Rb and Cs of the ratio r_a/r_c just after they transform into the *oC*16 phase, where r_a is the Wigner-Seitz radius and r_c the ionic radius. The ratio r_a/r_c is a measure for the free space available for the conduction electrons in metals. For Rb and Cs at ambient pressure $r_a/r_c \approx 1.83$, but decreases to about 1.11 where superconductivity first appears. Rb and Cs can no longer be treated with the nearly-free-electron model under sufficiently high pressure because the free space under pressure ($r_a/r_c \approx 1.1$ means that the ion cores begin to touch) would be too small that *s*-*d* transfer dominates, as discussed in Section 4.2.1. For K the ratio at 112 GPa is only 1.007, suggesting the possibility of superconductivity in K if the superconductivity for K is also associated with the degree of *s*-*d* transfer.

Table 4.2: Properties of Si, K, Rb, and Cs in *oC*16 phase.

	Si at 43 GPa	K at 112 GPa	Rb at 48 GPa	Cs at 12 GPa
a (Å)	7.969	8.032	9.372	11.205
b (Å)	4.776	4.753	5.550	6.626
c (Å)	4.755	4.716	5.528	6.595
a/*c*	1.676	1.703	1.695	1.699
b/*c*	1.004	1.008	1.004	1.005
y (8*f*)	0.172	--	0.170	0.173
z (8*f*)	0.328	--	0.318	0.327
x (8*d*)	0.219	--	0.211	0.216
d_1 (Å)	2.321	--	2.764	3.237
V_{atom} (Å^3)	11.309	11.252	17.970	30.603
V_{atom}/V_o	0.565	0.149	0.193	0.260
atomic mass	28	39	85	133
ionic radius at 1 bar r_c (Å)	--	1.38	1.52	1.67

Wigner-Seitz radius r_a (Å)	1.392	1.390	1.625	1.941
r_a/r_c	--	1.007	1.069	1.162
T_c (K)	4.9	--	2.5	1.5

The crystallographic data of Si, Rb, Cs and K are from [107] and [127], based on which the Wigner-Seitz radius r_a data are calculated. The ionic radius r_c data are from [99]. (0, y, z) and (x, 0, 0), referring to the orthorhombic axes (*a*-, *b*-, *c*-) in the *Cmca* space group, are the coordinates for 8*f* and 8*d* atoms, respectively. d_1 is shortest distance between two 8*f* atoms. The Wigner-Seitz radius $r_a \equiv [(3/4\pi)V_{atm}]^{1/3}$.

The diatomic units formed by 8*f* atoms in the flat layers of the *oC*16 phase (*oC*16 is a structure with SG *Cmca* and 16 atoms in the orthorhombic unit cell) of Rb, Cs, and probably K, may remind us the famous "ion pairing in the dense lithium" proposed by Neaton and Ashcroft [128]. They predicted the ground state of lithium above 100 GPa to be the *Cmca* phase. In this phase the Li ions are paired and valence electrons are confined to the interstitial regions in the lattice: the nearly-free-electron picture fails at this extreme pressure, giving way to a metal-to-semiconductor transition. The band structure of the *Cmca* phase was calculated to have a zero-bandgap at the Fermi level, leading to conditions favoring the onset of the superconducting state [128]. The metal-to-semiconductor transition in Li was not found until in 2009 Matsuoka and Shimizu reported a significant increase in electrical resistivity (ρ) and a negative $d\rho/dT$ slope when the pressure lies between 78 and 105 GPa [129], where Li is in the *oC*40 phase (SG *C2cb*). Five years later Matsuoka *et al*. [130] found that above 120 GPa Li re-entered a metallic *oC*24 (SG *Cmca*) phase where the resistivity is particularly large, thus calling it a "poor metal". Interestingly, they also found clear resistivity drops at 10.2 and 12.7 K at pressures of 120 and 137 GPa, respectively, implying possible superconductivity in the *oC*24 phase.

At 12 GPa in *oC*16 Cs, Schwarz *et al*. [132] found by calculation significant valence electron density maxima at the centers of the squares formed by the Cs 8*f* and Cs 8*d* atoms, respectively.

These maxima are not so isolated as the interstitial electrons in *Cmca* Li, but they could be strong enough to induce strong electron-phonon interactions in *oC*16 Cs and Rb that result in the appearance of superconductivity and the increase in the electrical resistivity reported herein.

Chapter 5

Summary

- Four-point dc resistivity measurements are carried out on pure Sm metal to ~ 150 GPa using a diamond anvil cell. The two magnetic ordering temperatures merge at 13 GPa after which $T_o(P)$ increases gradually to a maximum at 53 GPa, but then decreases and passes through a minimum at 85 GPa followed by a sharp increase to ~ 140 K at 150 GPa. Giant superconducting pair breaking is also observed in dilute Y(Sm) alloys. The magnetic properties of Sm are found to parallel those of another light lanthanide, Nd, as well as those of the heavier lanthanides Gd, Tb, and Dy. It appears that the magnetic phase diagram can be separated into two regions: a low-pressure region where conventional changes in the electronic structure determine $T_o(P)$, and a high-pressure region where highly correlated electron effects dominate, leading to such anomalous phenomena as unexpectedly high magnetic ordering temperatures and giant superconducting pair-breaking.

- Four-point dc and ac resistivity measurements are carried out on Cs to 45 GPa and Rb to 78 GPa. The superconductivity discovered by Wittig in Cs near 12 GPa is confirmed, with a critical temperature T_c near 1.5 K that decreases with pressure. Rb is found to become superconducting between 55 and 85 GPa, also with T_c decreasing with pressure from 2.5 to 1.3 K. In both cases superconductivity appears when Cs or Rb transforms from *tI*4 to the *oC*16 phase, accompanied by a sharp increase in the room-temperature resistivity with pressure. This feature and the similar negative dependence of T_c on P may

indicate a common driving force for the superconductivity of these two heavy alkali metals: the pressure induced *s*-*d* electron transfer. Extreme pressure brings the alkali ions into contact, forcing the conduction electrons into the interstitial regions, thus enhancing their *d*-band character. Under these conditions the electronic density of states $N(E_F)$ and the electron-phonon interaction are enhanced, facilitating the appearance of superconductivity in these two heavy alkali metals. It would be promising to extend previous searches for superconductivity in K to higher pressure (60 - 100 GPa) since it shares a similar sequence of structures under pressure.

Appendix A

β-Ce

Cerium is perhaps the most interesting elemental metal among the lanthanide series in terms of its rich structural and physical properties. It exists in three allotropes at ambient and low temperature: γ phase (fcc, a = 5.1610 Å), β phase (dhcp, a = 3.6810 Å, c = 11.857 Å) and α phase (fcc, a = 4.85 Å). β-Ce is an antiferromagnet with Néel temperature $T_N \approx 12.7$ K, which lies well above that (3.3 K) anticipated from simple de Gennes factor scaling compared to the Curie temperature (293 K) of Gd [(0.18/15.75)(293 K) = 3.3 K]. In addition, dilute concentrations of Ce impurity in superconducting La have been found to cause large superconducting pair breaking [36]. These effects show that even at ambient pressure the magnetic state of Ce is near an instability. In view of the results mentioned in Section 4.1 on other lanthanides under pressure, it may be possible to push T_N of β-Ce to even higher values than 12.7 K by applying pressure.

The β-Ce sample used in this investigation was prepared at the Ames Laboratory using a thermal cycling and annealing process [133]. High purity (99.9%) γ-Ce metal was sealed in tantalum crucibles and annealed for a week at 700°C to relieve any possible strains. The sample was then rapidly quenched back and forth between room-temperature and liquid helium temperature 12 times and then sealed under He gas in quartz tubes and placed in a furnace at 70 °C for one week. This process of thermal cycling and annealing was repeated four times. DC magnetization and specific heat measurements indicated that the samples were predominantly β-Ce. Measurements of the ac susceptibility were carried out in the He-gas system at 0.1 Oe rms and 1023 Hz by surrounding the sample ($1.3 \times 1.3 \times 5$ mm^3) with a calibrated primary/secondary coil

system connected to a Stanford Research SR830 digital lock-in amplifier via an SR554 transformer preamplifier. Pre-cooling with liquid N_2 brought the sample temperature down to 150 K. Then, using liquid He, the sample was cooled down rapidly from 150 K to 4 K within 5 min to avoid the β - α transition near 50 K. The ac susceptibility measurements were then performed while warming.

A pressure of 535 bar was then applied at 25 K that resulted in an increase in T_N, as seen in Figure A.1, the rate of increase being +0.32 ± 0.05 K/kbar. At 535 bar the accurate determination of $\chi'(T)$ for temperatures below 11 K was not possible due to the proximity of the He melting curve. Following the experiment at 535 bar, 1.7 kbar was applied at 25 K; unfortunately, a significant leak of He gas out of the pressure cell prevented a measurement. The leak went away after the pressure was reduced to 62 bar. Surprisingly, at 62 bar T_N increased further and the size of the transition was reduced.

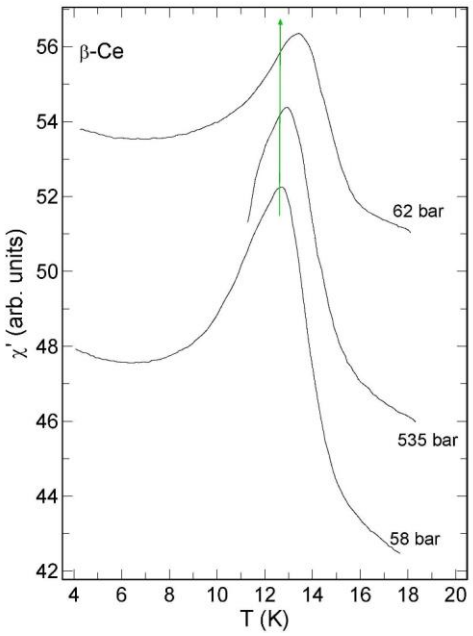

Figure A.1: Real part of ac susceptibility $\chi'(T)$ of β-Ce versus temperature at 58 bar, 535 bar, and 62 bar pressure, in that order. The increase in pressure from 58 bar to 535 bar gives the dT_N/dP = +0.32 ± 0.05 K/kbar. Vertical straight line marks T_N at 58 bar. The figure is taken from [134].

The size of the peak in the magnetic susceptibility data of β-Ce can be taken as a rough measure of the relative amount of β-Ce present in the sample [135]. A significant reduction in the transition size indicates that a large fraction of β-Ce has transformed to α-Ce as the susceptibility of α-Ce is much smaller than that of β-Ce. Since the atomic volume of β-Ce (34.784 $Å^3$/atom) is much greater than that of α-Ce (28.5 $Å^3$/atom), the α-Ce host would exert lattice pressure on minority regions of pure or nearly pure β-Ce minority phase, thus causing T_N at 62 bar upon release seen in Figure A.1 to increase. Another possible explanation for the shift in T_N follows from the fact that the β - α transformation is accompanied by a ~ 19% volume collapse and involves the movement of Ce atoms from the ABAC stacking arrangement in the dhcp crystalline lattice to ABC layering arrangement in the fcc lattice. Hence the remaining small fraction of β-Ce must be highly strained due to deformation during the β - α transformation. As discussed in Ref [135], the presence of a large amount of α phase possibly creates a large number of stacking faults in the highly strained β-Ce. This may increase the number of hexagonal sites relative to cubic sites in β-Ce. T_N would then shift upward upon release of pressure since the hexagonal sites are believed to lead to higher magnetic ordering temperatures than the cubic sites [136].

These results have been recently published in Ref. [134].

Appendix B

$PbTaSe_2$

$PbTaSe_2$ was identified as a topological, nodal semimetal with strong spin-orbit coupling [137]. To study the $T_c(P)$ behavior of $PbTaSe_2$, U. Kaluarachchi *et al*. [138] in Ames lab synthesized high-quality single crystals of $PbTaSe_2$ and measured its electrical transport and magnetic properties under pressure. They found the existence of two superconducting phases with phase boundary at ~ 0.25 GPa near 3 K. Transmission electron microscopy (TEM) and x-ray diffraction confirmed this phase transition is structural and occurs ~ 425 K at ambient pressure. In their temperature dependent resistivity and dc magnetization measurements under pressure, piston-cylinder pressure cells were used, with some liquids as pressure media. Due to the different thermal contractions of materials of cells and pressure media upon cooling, it is difficult to tell pressure at intermediate temperature range even though the room-temperature/low temperature pressure can be determined by manganin/Pb gauge.

By the He-gas hydrostatic pressure system, precise temperature and pressure control (1 bar) can be achieved from room-temperature to 1.5 K, from ambient pressure to near 1 GPa. Considering the very sharp phase transition estimated as $\Delta T_s/\Delta P$ ~ -1700 K/GPa near 4 K [130], the system is perfect to measure the resistance of $PbTaSe_2$ at different temperatures and pressures, so that its phase diagram can be obtained. A series of four-point ac electrical resistivity measurements were performed by the He-gas hydrostatic pressure system, on two $PbTaSe_2$ crystals with approximate dimensions 0.5 × 0.1 × 0.05 mm3 to hydrostatic pressures as high as 0.37 GPa. An excitation current of 1 mA (rms) at 17 Hz was applied using a Keithley 6221 constant ac/dc current source and the small voltage detected by a Stanford Research SR830 digital lock-in amplifier.

First, experiments were carried out at constant temperatures (295, 200, 150, 82, and 50 K) with varying pressures. Two $PbTaSe_2$ crystals showed quite similar behaviors and results of sample 2 are presented in Figure B.1 (left). The hysteretic nature of the transition is seen in pressure sweeps, suggesting it might be a first-order transition. These signatures are sharp and well defined. At lower temperatures the transition shifts to higher pressures and the size of the resistance jump becomes smaller, finally disappeared in the pressure sweep at ~ 50 K.

Then, temperature dependent resistance of $PbTaSe_2$ at some constant pressures were measured shown in Figure B.1 (right). Pressure was applied at room-temperature and monitored during cooling and warming. The hysteresis in the transition is seen as well as for the pressure sweeps. At higher pressures the transition shifts to lower temperatures and the size of the resistance jump also becomes smaller. Both $R(P)$ at constant temperatures and $R(T)$ at constant pressures give the evidence of a phase transition in $PbTaSe_2$ happening at low temperature and low pressure.

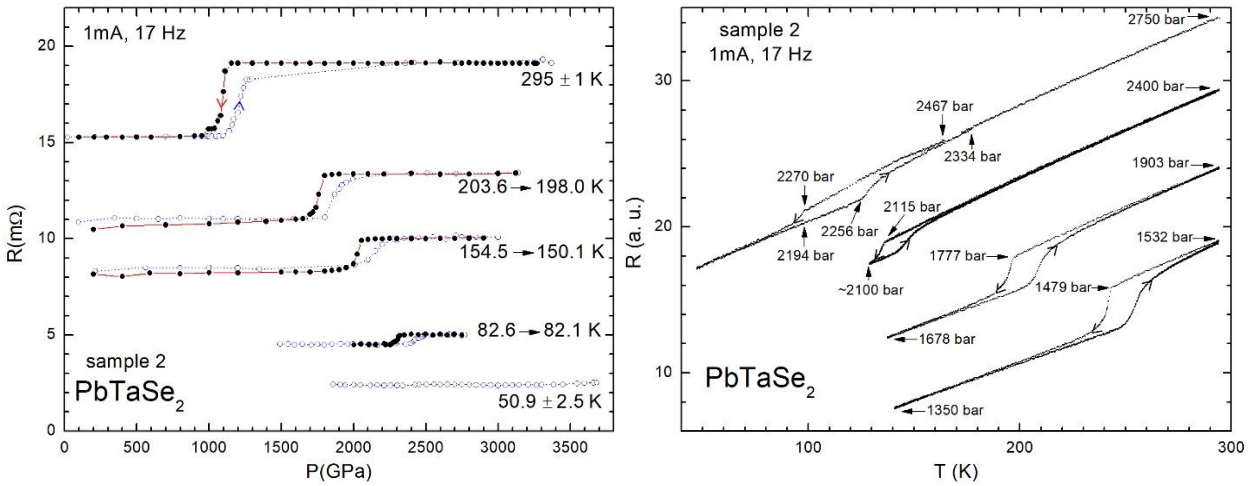

Figure B.1: Examples (left) of pressure sweeps at constant temperatures and (right) of temperature sweeps at almost constant, continuously monitored, gas pressures. Numbers indicate in (left) change of temperature during the run and in (right) measured pressures in bar. Arrows on the curves indicate the direction of the temperature/pressure changes.

Combining the data from resistivity measurements by He-gas hydrostatic pressure system or a piston-cylinder cell, high temperature TEM, and dc magnetization, the pressure-temperature phase diagram of $PbTaSe_2$ single crystals was plotted as in Figure B.2 on a semi-log scale [138].

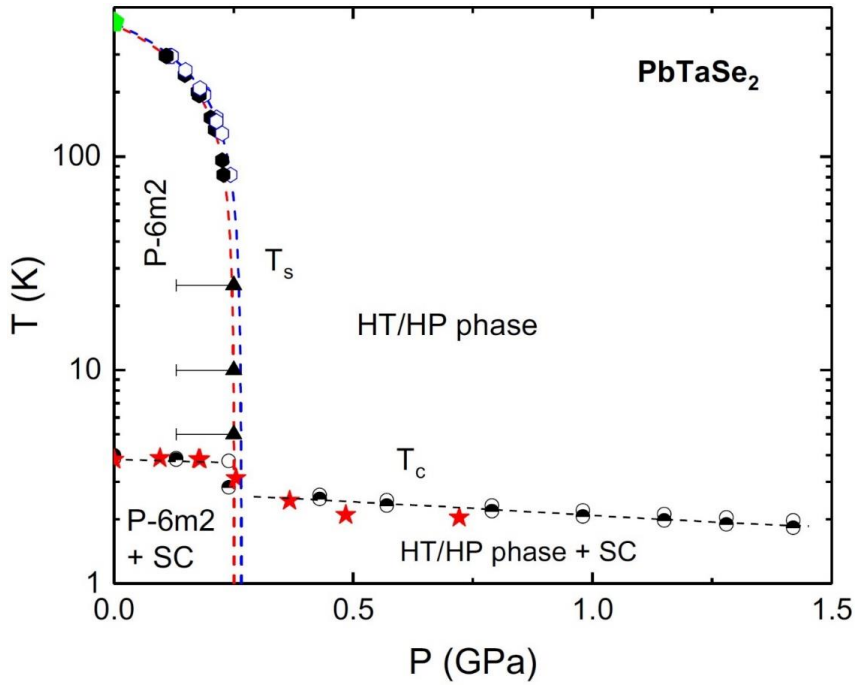

Figure B.2: Four regions in the phase diagram of $PbTaSe_2$ are labeled. Lines are guides to the eye. HT/HP denotes high temperature/high pressure. Green pentagon is ambient pressure data point from high temperature TEM. Open and filled hexagons are resistively detected structural transitions in the He-gas pressure data. Triangles are resistively detected structural transitions in the piston-cylinder cell data. Open and half-filled circles are resistively measured superconducting transition temperature. Stars are T_c values determined from the magnetization. The figure is taken from [138].

These results have been published in Ref. [138].

Appendix C

$Bi_2Te_3/Fe_{1+y}Te$

A $Bi_2Te_3/Fe_{1+y}Te$ heterostructure has been reported recently [139] that exhibits interfacial superconductivity at an atomically-flat van der Waals-bonded boundary between the non-superconducting parent compound $Fe_{1+y}Te$ of the "11" iron-based superconductor family and the non-superconducting topological insulator (TI) Bi_2Te_3. The superconductivity starts from one quintuple layer (QL) of the TI, with a T_c onset increasing with more QLs of Bi_2Te_3 until it saturates at about 12 K for thicknesses exceeding 5 QLs. The superconducting mechanism remains unknown and it is unclear whether the highest T_c for more than 5 QLs of Bi_2Te_3 can be further increased, perhaps by application of hydrostatic pressure. Also, pressure has been proven an effective tool to tune the superconductivity in iron-based superconductors. It would be interesting to measure the temperature dependent resistivity of the heterostructure under pressure.

A $Bi_2Te_3/Fe_{1+y}Te$ ($y = 0.15 \pm 0.02$) heterostructure with 9 QLs of Bi_2Te_3 was synthesized in a VG-V80H MBE system by He *et al*. in the department of physics, the Hong Kong University of Science and Technology [139]. The electrical resistance measurements under high pressure were conducted in the He-gas hydrostatic pressure system, using the four-probe method with an ac current of 0.1 μA at 77 Hz. The sample voltage was amplified by an SR554 preamplifier and fed into an SR830 lock-in amplifier. The sample was cut into the form of a long strip and silver paint was used to fabricate electrodes on the top surface of Bi_2Te_3. The silver paint can quickly diffuse into Bi_2Te_3, so the electrodes contact with the entire TI layer, the interface, and a part of the $Fe_{1+y}Te$ layer below.

The $R(T)$ curves at different pressures were shown in Figure C.1 [140]. The resistance comes from three parts in parallel: the 9QLs of Bi_2Te_3, the interface layer, and the bulk $Fe_{1+y}Te$ layer. The $R(T)$ curves at all pressures show an insulator-to-metal transition at 76 K (T_{SDW}), characteristic for $Fe_{1+y}Te$ layer, which originates from the antiferromagnetic double-stripe spin density wave (SDW) ordering in bulk $Fe_{1+y}Te$ layer. For the $R(T)$ at ambient pressure, resistance goes through a minimum at 24 K, followed by a sudden increase with a maximum (T_c onset) at ~ 12 K, then drops to zero at T_o ~ 4 K. The peak also appears at 2.1 and 3.9 kbar, which is typical for $Fe_{1+y}Te$ with high excess iron, and likely originates from scattering on the interstitial iron magnetic moments in bulk $Fe_{1+y}Te$ layer. The zero resistance is due to the superconducting interface layer, which shunts the bulk $Fe_{1+y}Te$ layer and the Bi_2Te_3 layer. As seen in Figure C.1, pressure decreases the resistance of $Fe_{1+y}Te$ metallic state, suppresses the peak at T_c onset, and increases T_c onset and T_o (see the inset of Figure C.1).

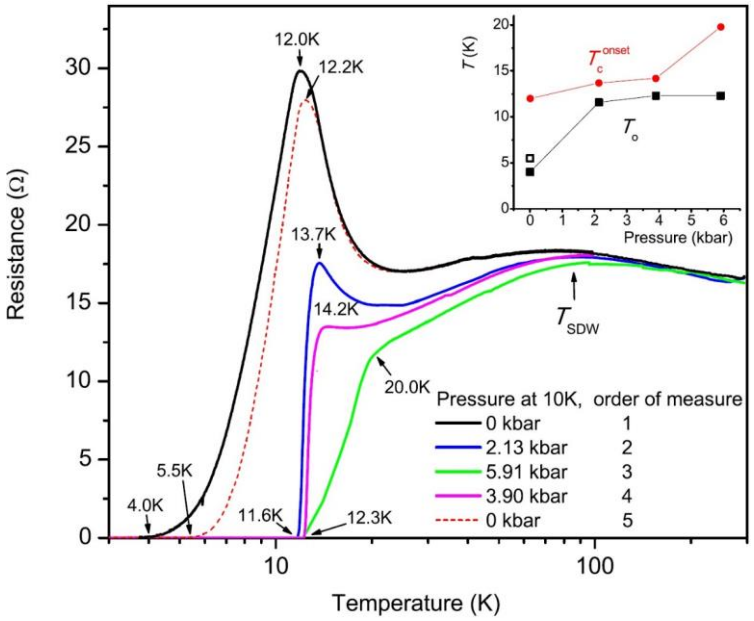

Figure C.1: The temperature dependent resistance measurement on the $Bi_2Te_3/Fe_{1+y}Te$ heterostructure under pressures up to 5.91 kbar. The temperature T_o where the resistance reaches zero is enhanced from 4.0 K to 12.3 K by applying pressure, while the peak located at T_c onset is suppressed thus shifting the onset of the critical temperature up to 20 K at the highest pressure. T_{SDW} marks approximately the

transition below which the antiferromagnetic spin density wave is formed. The inset shows the pressure evolution of the critical temperatures T_o. The open square is T_o after the pressure was released at the end of the experiment. The figure is taken from [140].

At the interface, the antiferromagnetic order of FeTe may be changed in a manner favorable for superconductivity, by the presence of the topological surface state of Bi_2Te_3. The hydrostatic pressure could push the different layers in the heterostructure closer together, thereby reducing the anisotropy and increasing the electronic coupling between the interfacial FeTe and Bi_2Te_3 layers, so that the influence of the surface state on the interface region can become more important. Although the mechanism of how this interaction with the surface state causes superconductivity remains unclear, a strengthening of the interaction may explain the T_c increase [140].

The peak at T_c onset is suppressed by pressure, suggesting the scattering of charge carriers on interstitial iron is suppressed. This indicates that the magnetic moments of the interstitial irons become more ordered, probably as a result of a stronger coupling to the antiferromagnetically ordered iron moments within the FeTe layers. Another possibility is that pressure induces a spatial ordering, or a kind of clustering of interstitial irons. This is illustrated by the dramatic sharpening of the superconducting transition under pressure. Apart from this, a pressure-induced ordering can suppress the finite-size effect, which causes the broadening of the 2D Berezinski–Kosterlitz–Thouless transition. The pressure-induced ordering or clustering of interstitial irons could reduce the finite-size effect, resulting in the sharper transition. This is further supported by the fact that both the T_c onset and T_o remain higher than their initial values after releasing pressure [140].

These results have been published in Ref. [140].

Appendix D

β-Li_2IrO_3

The novel electronic ground states of 5*d*-based compounds driven by spin-orbit (SO) interactions continue provides a playground for the realization of quantum spin liquids (QSLs), for example the nontrivial QSL ground state of the Kitaev model [141], a solvable interacting quantum model with Majorana fermions as its elementary excitations. β-Li_2IrO_3 is a candidate for the possible realization of the Kitaev model. However, it is experimentally established that it orders magnetically at low temperatures, spoiling numerous attempts to realize the Kitaev QSL. Hence, tuning structure and related intricate interactions present in β-Li_2IrO_3 through pressure provides a potential route to introduce magnetic frustration and realize novel phases of matter.

L. S. I. Veiga *et al*. [142] conducted x-ray absorption spectroscopy, x-ray magnetic circular dichroism (XMCD), x-ray diffraction under high pressure, and theoretical calculations to study the electronic, magnetic, and structural properties of β-Li_2IrO_3 under pressure. To provide electrical transport information of this material, resistivity measurements were made up to 7 GPa by DAC, with 0.9 mm diameter culet anvils. A β-Li_2IrO_3 crystal (approximate dimensions 300 * 150 * 10 μm^3) was loaded at the center of a cBN-epoxy insulted Re gasket. Due to nonhydrostaticity and sample brittleness, the crystal was crushed as the cell was assembled, thus the presented data were powder averaged. Several small ruby spheres were placed next to the sample as the pressure gauge. Four-point dc electrical resistivity measurements with 1 μA excitation current (Keithley 220 current source) were carried out on the sample. Sample voltages were measured by a Keithley 182 nanovoltmeter. Temperature was determined by a *Cernox* resistor positioned just above one of the diamond anvils.

Figure D.1 [142] shows the resistance versus temperature for several pressures together with the pressure-dependent insulating gap estimated from Arrhenius fits to the data in two different temperature ranges. While no signature of an insulator-metal transition is observed, the electronic gap estimated from fits to the resistivity data decreases linearly with pressure, likely a result of a reduction in on-site Coulomb interactions upon a pressure-induced increase in bandwidth. That the system remains insulating to 7 GPa lends further support to the presence of interacting local moments above 2 GPa, revealed also in XMCD results [142].

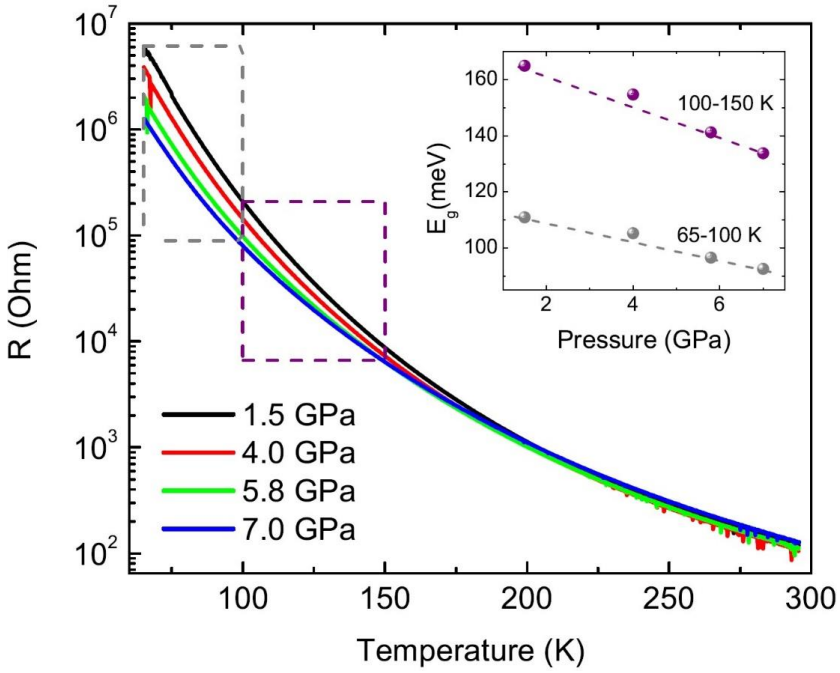

Figure D.1: Resistance of β-Li_2IrO_3 versus temperature as a function of pressure from four-probe measurements in the DAC. The insulating gap E_g as a function of pressure (inset) was estimated using $\ln R \sim E_g/k_B T$ and its value depends on the temperature range chosen. Two different temperature ranges were selected for the fittings: 65 - 100 K (grey box and grey spheres) and 100 - 150 K (purple box and purple spheres). The figure is taken from [142].

These results have been published in Ref. [142].

Bibliography

[1] K. N. R. Taylor and M. I. Darby, *Physics of Rare Earth Solids* (Chapman and Hall Ltd, London, 1972).

[2] J. Song, W. Bi, D. Haskel, and J. S. Schilling, Phys. Rev. B **95**, 205138 (2017).

[3] J. Lim, G. Fabbris, D. Haskel, and J. S. Schilling, Phys. Rev. B **91**, 174428 (2015).

[4] J. Lim, G. Fabbris, D. Haskel, and J. S. Schilling, Phys. Rev. B **91**, 045116 (2015).

[5] J. Bardeen, L. N. Cooper, J. R. Schrieffer, Phys. Rev. **108**, 1175 (1957).

[6] J. Tuoriniemi, K. Juntunen-Nurmilaukas, J. Uusvuori, E. Pentti, A. Salmela, and A. Sebedash, Nature **447**, 187 (2007).

[7] S. Deemyad, J. S. Schilling, Phys. Rev. Lett. **91**, 167001 (2003).

[8] J. Wittig, Phys. Rev. Lett. **24**, 812 (1970); J. J. Hamlin, V. G. Tissen, and J. S. Schilling, Physica C **451**, 82 (2007).

[9] J. Lim, *Enhanced Magnetism in Dy and Tb at Extreme Pressure*, Ph.D. Thesis, Washington University, St. Louis, Missouri, 2015.

[10] J. Jensen and A. R. Mackintosh, *Rare Earth Magnetism: Structures and Excitations* (CLARENDON PRESS · OXFORD) edited by J. Birman, S. F. Edwards, C. H. Llewellyn, S. M. Rees, p. 13-57, 1991

[11] B. Coqblin and J. R. Schrieffer, Phys. Rev. **185**, 847 (1969).

[12] J. Stankiewicz, M. Evangelisti, Z. Fisk, P. Schlottmann, and L.P. Gor'kov, Phys. Rev. Lett. **108**, 257201 (2012).

[13] J. Kondo, Prog. Theor. Phys. **32**, 37 (1964).

[14] S. Doniach, Physica B+C **91**, 231 (1977); S. Doniach, in *Valence Instabilities and Related Narrow-Band Phenomena*, edited by R. D. Parks (Plenum, New York, 1977), p. 169.

[15] M. Somayazulu, M. Ahart, A. K. Mishra, Z. M. Geballe, M. Baldini, Y. Meng, V. V. Struzhkin, and R. J. Hemley, Phys. Rev. Lett. **122**, 027001 (2019).

[16] A. P. Drozdov, P. P. Kong, V. S. Minkov, S. P. Besedin, M. A. Kuzovnikov, S. Mozaffari, L. Balicas, F. Balakirev, D. Graf, V. B. Prakapenka, E. Greenberg, D. A. Knyazev, M. Tkacz, and M. I. Eremets, arXiv:1812.01561 Cond-Mat (2018).

[17] R. P. Dias and I. F. Silvera, Science **355**, 715 (2017).

[18] N. W. Ashcroft, Phys. Rev. Lett. **21**, 1748 (1968).

[19] U. Gottlieb, J. C. Lasjaunias, J. L. Tholence, O. Laborde, O. Thomas, and R. Madar, Phys. Rev. B. **45**, 4803 (1992).

[20] Y. Cao, V. Fatemi, S. Fang, K. Watanabe, T. Taniguchi, E. Kaxiras, and P. Jarillo-Herrero, Nature **556**, 43 (2018).

[21] E. Maxwell, Phys. Rev. **78**, 477 (1950).

[22] C. A. Reynolds, B. Serin, W. H. Wright, and L. B. Nesbitt, Phys. Rev. **78**, 487 (1950).

[23] N. W. Ashcroft and N. D. Mermin, in *Solid State Physics* (Saunders College Publishing, Inc., United States, 1976), p. 745-747.

[24] G. M. Eliashburg, Sov. Phys. JETP **11**, 696 (1960).

[25] V. Z. Kresin, S. A.Wolf, *Fundamentals of Superconductivity* (Plenum Press, New York, 1990).

[26] W. L. McMillan, Phys. Rev. **167**, 331 (1968).

[27] T. F. Smith and C. W. Chu, Phys. Rev. **159**, 353 (1967).

[28] C. W. Chu, T. F. Smith, and W. E. Gardner, Phys. Rev. B **1**, 214 (1970).

[29] J. P. Carbotte, Rev. Mod. Phys. **62**, 1027 (1990).

[30] B. Lorenz and C. W. Chu. High pressure effects on superconductivity. In *Frontiers in Superconducting Materials*, pp. 459-497. Springer, Berlin, Heidelberg, 2005.

[31] J. S. Schilling. *Handbook of High Temperature Superconductivity: Theory and Experiment*, chapter 11. Springer, Hamburg, 2007.

[32] J. Song, *Highly Correlated Electron Effects in Selected Lanthanides under Extreme Pressure*, Ph.D. Thesis, Washington University, St. Louis, Missouri, 2018.

[33] J. Wittig, Phys. Rev. Lett. **21**, 1250 (1968).

[34] M. Debessai, T. Matsuoka, J. J. Hamlin, J. S. Schilling, and K. Shimizu, Phys. Rev. Lett. **102**, 197002 (2009).

[35] B. T. Matthias, H. Suhl, and E. Corenzwit, Phys. Rev. Lett. **1**, 92 (1958).

[36] M. B. Maple, J. Wittig, and K. S. Kim, Phys. Rev. Lett. **23**, 1375 (1969).

[37] A. A. Abrikosov, L. P. Gorkov, Zh. Eksperim. i. Teor. Fiz. **39**, 1781 (1960).

[38] E. Müller-Hartmann and J. Zittartz, Z. Physik **234**, 58 (1970).

[39] N. J. Hillier, *High Pressure Studies of Superconductivity*, Ph.D. Thesis, Washington University, St. Louis, Missouri, 2013.

[40] Schilling Lab Manual (unpublished), Washington University. *Resistivity and Susceptibility Measurements in a Helium-Gas System*.

[41] C. E. Weir, E. R. Lippincott, A. V. Valkenburg, E. N. Bunting, J. Res. Natl. Bur. Stand. **63A**, 55 (1959).

[42] L. Dubrovinsky, N. Dubrovinskaia, E. Bykova, M. Bykov, V. Prakapenka, C. Prescher, K. Glazyrin, H. -P. Liermann, M. Hanfland, M. Ekholm, Q. Feng, L. V. Pourovskii, M. I. Katsnelson, J. M. Wills, and I. A. Abrikosov, Nature **525**, 226 (2015).

[43] D. J. Dunstan and I. L. Spain, Journal of Physics E: Scientific Instruments **22**, 913 (1989).

[44] J. S. Schilling, *High Pressure in Science and Technology: Part I, Collective Phenomena and Transport Properties* (North Holland, New York, 1984).

[45] *Diamond Anvil Cell Manual: Cell Preparation, AC Susceptibility and Electrical Resistivity Measurements, Accessory Equipment* (Schilling High Pressure Laboratory Manual, Washington Univesity, St. Louis, unpublished, 2014).

[46] K. Shimizu, K. Amaya, and N. Suzuki, J. Phys. Soc. Japan **74**, 1345 (2005).

[47] J. J. H. Hamlin, *Superconductivity Studies at Extreme Pressure*, Ph.D. thesis, Washington University, St. Louis, Missouri, 2007.

[48] J. Thomasson, C. Ayache, I. L. Spain, and M. Villedieu, J. Appl. Phys. **68**, 5934 (1990).

[49] A. Onodera and A. Ohtani, J. Appl. Phys. **51**, 2581 (1980).

[50] D. L. Decker, J. Appl. Phys. **42**, 3239 (1971).

[51] D. L. Heinz and R. Jeanloz, J. Appl. Phys. **55**, 885 (1984).

[52] R. A. Forman, G. J. Piermarini, J. D. Barnett, and S. Block, Science **176**, 284 (1972).

[53] J. C. Chervin, B. Canny, and M. Mancinelli, High Pressure Res. **21**, 305 (2001).

[54] K. Syassen, High Pressure Res. **28**, 75 (2008).

[55] S. Buchsbaum, R. L. Mills, and D. Schiferl, J. Phys. Chem. **88**, 2522 (1984).

[56] J. Yen, and M. Nicol, J. of Appl. Phys. **72**, 5535 (1992).

[57] H. K. Mao, J. Xu, and P. M. Bell, J. Geophys. Res. **91**, 4673 (1986).

[58] A. D. Chijioke, W. J. Nellis, A. Soldatov, and I. F. Silvera, J. of Appl. Phys. **98**, 114905 (2005).

[59] A. L. Ruoff, *Recent Trends in High Pressure Research* (IBH, Oxford, New Delhi, 1992) p. 798.

[60] Y. K. Vohra, S. J. Duclos, K. E. Brister, and A. L. Ruoff, Phys. Rev. Lett. **61**, 574 (1988).

[61] S. A. Solin and A. K. Ramdas, Phys. Rev. B **1**, 1687 (1970).

[62] M. Hanfland and K. Syassen, J. Appl. Phys. **57**, 2752 (1985).

[63] Y. Akahama and H. Kawamura, J. Appl. Phys. **100**, 043516 (2006).

[64] W. B. Holzapfel, J. Alloys Compounds **223** 170 (1995).

[65] J. C. Duthie and D. G. Pettifor, Phys. Rev. Lett. **38**, 564 (1977).

[66] J. R. Schrieffer, J. Appl. Phys. **38**, 1143 (1967).

[67] J. S. Schilling, Adv. Phys. **28**, 657 (1979).

[68] G. Fabbris, T. Matsuoka, J. Lim, J. R. L. Mardegan, K. Shimizu, D. Haskel, and J. S. Schilling, Phys. Rev. B **88**, 245103 (2013).

[69] Y. C. Zhao, F. Porsch, and W. B. Holzapfel, Phys. Rev. B **50**, 6603 (1994).

[70] Y. Vohra, L. Akella, S. Weir, and G. A. Smith, Phys. Lett. A **158**, 89 (1991).

[71] S. Blundell, in *Magnetism in Condensed Matter* (Oxford University Press, New York 2001) p. 34.

[72] H. Adachi, H. Ino, and H. Miwa, Phys. Rev. B **56**, 349 (1997).

[73] L. D. Jennings, E. D. Hill, and F.H. Spedding, J. Chem. Phys. **31**, 1240 (1959).

[74] J. K. Alstad, R. V. Colvin, S. Legvold, and F. H. Spedding, Phys. Rev. **121**, 1637 (1961).

[75] K. A. McEwen, P. F. Touborg, G. J. Cock and L. W. Roeland, J. Phys. F: Metal Phys. **4**, 2264 (1974).

[76] W. C. Koehler and R. M. Moon, Phys. Rev. Lett. **29**, 1468 (1972).

[77] W. Y. Dong, T. H. Lin, K. J. Dunn and C. N. J. Wagner, Phys. Rev. B **35**, 966 (1987).

[78] C. R. Johnson, G. M. Tsoi, and Y. K. Vohra, J. Phys.: Condens. Matter **29**, 065801 (2017).

[79] Material Preparation Center, Ames Laboratory, U.S. Department of Energy, Ames, Iowa, http://www.mpc.ameslab.gov.

[80] James S. Schilling, in *Proceedings of the 9th AIRAPT International High Pressure Conf.*, Albany, New York, July 24-29, 1983, editors C. Homan, R.K. MacCrone and E. Whalley (North-Holland, N.Y., 1984); Mat. Res. Soc. Symp. Proc. **22**, 79 (1984).

[81] W. B. Daniels and W. Ryschkewitsch, Rev. Sci. Instr. **54**, 115 (1983).

[82] H. J. van Daal and K. H. J. Buschow, Solid State Commun. **7**, 217 (1969).

[83] R. V. Colvin, S. Legvold, and F. H. Spedding, Phys. Rev. **120**, 741 (1960).

[84] M. B. Maple, Appl. Phys. **9**, 179 (1976).

[85] G. K. Samudrala, G. M. Tsoi, and Y. K. Vohra, J. Phys. Condens. Matter **24**, 362201 (2012).

[86] D. D. Jackson, V. Malba, S. T. Weir, P. A. Baker, and Y. K. Vohra, Phys. Rev. B **71**, 184416 (2005).

[87] G. S. Fleming and S. H. Liu, Phys. Rev. B **2**, 164 (1970); S. H. Liu, Phys. Rev. **127**, 1889 (1962).

[88] G. N. Chesnut and Y. K. Vohra, Phys. Rev B **61**, R3768 (2000).

[89] N. C. Cunningham, W. Qiu, K. M. Hope, H.-P. Liermann, and Y. K. Vohra, Phys. Rev B **76**, 212101 (2007).

[90] R. Patterson, C. K. Saw, and J. Akella, J. Appl. Phys. **95**, 5443 (2004).

[91] C. N. Singman, J. Chem. Ed. **61**, 137 (1984).

[92] J. Wittig, Phys. Rev. Lett. **46**, 1431 (1981).

[93] J. Wittig, *Valence Instabilities*, edited by P. Wachter and H. Boppart (North-Holland, Amsterdam, 1982), p. 427.

[94] Y. Xie, Y. M. Ma, T. Cui, Y. Li, J. Qiu, and G. T. Zou, New J. Phys. **10**, 063022 (2008).

[95] N. E. Christensen and D. L. Novikov, Solid State Commun. **119**, 477 (2001).

[96] U. Schwarz, K. Takemura, M. Hanfland, and K. Syassen, Phys. Rev. Lett. **81**, 2711 (1998).

[97] D. A. Young, *Phase Diagrams of the Elements* (University of California Press, Berkeley, CA, 1991).

[98] D. K. C. MacDonald, G. K. White, and S. B. Woods, Proc. Roy. Soc. (London) A **235**, 358 (1956).

[99] J. S. Schilling, High Pressure Res. **26**, 145 (2006).

[100] M. I. McMahon, R. J. Nelmes, and S. Rekhi, Phys. Rev. Lett. **87**, 255502 (2001).

[101] K. Takemura, S. Minomura, and O. Shimomura, Phys. Rev. Lett. **49**, 1772 (1983).

[102] K. Takemura, O. Shimomura, and H. Fujihisa, Phys. Rev. Lett. **66**, 2014 (1991).

[103] K. Takemura and K. Syassen, Solid State Commun. **44**, 1161 (1982).

[104] R. J. Nelmes, M. I. McMahon, J. S. Loveday, and S. Rekhi, Phys. Rev. Lett. **88**, 155503 (2002).

[105] M. I. McMahon, S. Rekhi, and R. J. Nelmes, Phys. Rev. Lett. **87**, 055501 (2001).

[106] H. Olijnyk and W. B. Holzapfel, Phys. Lett. **99A**, 381, (1983).

[107] U. Schwarz, K. Syassen, A. Grzechnik, and M. Hanfland, Solid State Commun. **112**, 319 (1999).

[108] S. De Panfilis, F. Gorelli, M. Santoro, L. Ulivi, E. Gregoryanz, T. Irifune, T. Shinmei, I. Kantor, O. Mathon, and S. Pascarelli, J. Chem. Phys. **142**, 214503 (2015).

[109] A. K. McMahan, Phys. Rev. B **29**, 5982 (1984).

[110] A. Jayaraman, R. C. Newton, and J. M. McDonough, Phys. Rev. **159**, 527 (1967).

[111] R. Boehler and C. Zha, Physica B+C, **139** & **140**, 233 (1986).

[112] J. Wittig, in *Superconductivity in d- and f-Band Metals*, edited by W. Buckel and W. Weber (Kernforschungszentrum, Karlsruhe, 1982), p. 321–29.

[113] K. Ullrich, C. Probst and J. Wittig, J. de Physique, Colloque **6**, 463 (1978).

[114] K. Ullrich, C. Probst, and J. Wittig, *Electrical resistance, superconductivity and phase transformations of rubidium and casium under high pressure*, Bericht Kernforschungsanlage Jülich, Jül-1634 (1980).

[115] H. T. Hall, L. Merrill, and J. D. Barrett, Science **146**, 1297 (1964).

[116] C. W. Chu, T. F. Smith, and W. E. Gardner, Phys. Rev. B **1**, 214 (1970).

[117] M. Mito, H. Matsui, K. Tsuruta, T. Yamaguchi, K. Nakamura, H. Deguchi, N. Shirakawa, H. Adachi, T. Yamasaki, H. Iwaoka, Y. Ikoma and Z. Horita, Sci. Rep. **6**, 36337 (2016).

[118] K. J. Dunn and F. P. Bundy, Phys. Rev. B **25**, 194 (1982).

[119] S. Mizobata, T. Matsuoka, and K. Shimizu, J. Phys.Soc. Jpn. **76** Suppl. A, 23 (2007).

[120] H. Olijnyk and W. B. Holzapfel: Phys. Lett. **100A**, 191 (1984).

[121] S. Deemyad, *Superconductivity under Extreme Hydrostatic Pressures in Lithium, MgB_2 and LaNdSrCuO*, PhD thesis, Washington University in St. Louis (2004).

[122] T. Tomita, S. Deemyad, J.J. Hamlin, J.S. Schilling, V.G. Tissen, B.W. Veal, L. Chen and H. Claus, J. Phys.: Condens. Matter **17**, S921 (2005).

[123] M. T. Debessai, *Superconductivity in Selected Elements and Compounds under Extreme Pressure*, PhD thesis, Washington University in St. Louis (2009).

[124] T. H. Lin and K. J. Dunn, Phys. Rev. B **33**, 807 (1986).

[125] D. Erskine, P. Y. Yu, K. J. Chang, and M. L. Cohen, Phys. Rev. Lett. **57**, 2741 (1986).

[126] M. Hanfland, U. Schwarz, K. Syassen, and K. Takemura, Phys. Rev. Lett. **82**, 1197 (1999).

[127] L. F. Lundegaard, M. Marqués, G. Stinton, G. J. Ackland, R. J. Nelmes, and M. I. McMahon, Phys. Rev. B **80**, 020101(R) (2009).

[128] J. B. Neaton and N. W. Ashcroft, Nature **400**, 141 (1999).

[129] T. Matsuoka and K. Shimizu, Nature **458**, 186 (2009).

[130] T. Matsuoka, M. Sakata, Y. Nakamoto, K. Takahama, K. Ichimaru, K. Mukai, K. Ohta, N. Hirao, Y. Ohishi, and K. Shimizu, Phys. Rev. B **89**, 144103 (2014).

[131] Roger Rousseau, Kentaro Uehara, Dennis D. Klug, and John S. Tse, ChemPhysChem **6**, 1703 (2005).

[132] U. Schwarz, O. Jepsen, K. Syassen, Solid State Commun. **113**, 643 (2000).

[133] D. C. Koskimaki, K. A. Gschneidner, Jr, and N. T. Panousis, J. Crystal Growth **22**, 225 (1974).

[134] P. Malavi, Y. Deng, F. Guillou, Y. Mudryk, V. Pecharsky, and J. S. Schilling, Solid State Commun. **294**, 36 (2019).

[135] D. C. Koskimaki, *Some Low-Temperature Properties of Cerium* (1973). Retrospective Theses and Dissertations. Paper 5024.

[136] D. C. Koskimaki, K. A. Gschneidner, Jr, Phys. Rev. B **10**, 5 (1974).

[137] G. Bian, T.-R. Chang, R. Sankar, S.-Y. Xu, H. Zheng, T. Neupert, C.-K. Chiu, S.-M. Huang, G. Chang, I. Belopolski, D. S. Sanchez, M. Neupane, N. Alidoust, C. Liu, B. Wang, C.-C. Lee, H.-T. Jeng, C. Zhang, Z. Yuan, S. Jia, A. Bansil, F. Chou, H. Lin, and M. Zahid Hasan, Nat. Commun. **7**, 10556 (2016).

[138] U. S. Kaluarachchi, Y. Deng, M. F. Besser, K. Sun, L. Zhou, M. C. Nguyen, Z. Yuan, C. Zhang, J. S. Schilling, M. J. Kramer, S. Jia, C. Wang, K. Ho, P. C. Canfield, and S. L. Bud'ko, Phys. Rev. B **95**, 224508 (2017).

[139] Q. L. He, H. Liu, M. He, Y. H. Lai, H. He, G. Wang, K. T. Law, R. Lortz, J. Wang, and I. K. Sou, Nat. Commun. **5**, 4247 (2014).

[140] J. Shen, C. Heuckeroth, Y. Deng, Q. He, H. C. Liu, J. Liang, J. Wang, I. K. Sou, J. S. Schilling, and R. Lortz, Physica C **543**, 18 (2017).

[141] A. Kitaev, Ann. Phys. **321**, 2 (2006).

[142] L. S. I. Veiga, M. Etter, K. Glazyrin, F. Sun, C. A. Escanhoela, Jr., G. Fabbris, J. R. L. Mardegan, P. S. Malavi, Y. Deng, P. P. Stavropoulos, H.-Y. Kee, W. G. Yang, M. van Veenendaal, J. S. Schilling, T. Takayama, H. Takagi, and D. Haskel, Phys. Rev. B **96**, 140402(R) (2017).